Dissertation Thesis

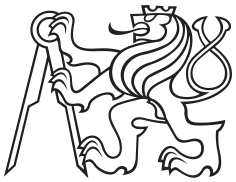

Czech Technical University in Prague

F3

Faculty of Electrical Engineering
Department of Physics

Acoustics of interaction of unsteady flows with periodic structures

Viktor Hruška

Supervisor: doc. Dr. Ing. Michal Bednařík
Supervisor–specialist: Ing. Milan Červenka, Ph.D.
Field of study: Electrical Engineering anf Information Technology
Subfield: Acoustics
February 2021

Acknowledgements

I would like to sincerely thank my supervisor Michal Bednařík and supervisor-specialist Milan Červenka for the guidance, opportunities and patience.

Above all, I am grateful to my wife and sons for all the support and kind tolerance.

Work on this thesis was supported by the Grant Agency of the Czech Technical University in Prague, grants

- SGS19/107/OHK3/2T/13
- SGS17/130/OHK3/2T/13

Declaration

I hereby declare I have written this doctoral thesis independently and I quoted all the sources of information used in accordance with methodological instructions on ethical principles for writing an academic thesis. Moreover, I state that this thesis has neither been submitted nor accepted for any other degree.

In Prague, February 2021

Viktor Hruška

Abstract

This thesis deals with chosen topics from the aeroacoustics of periodic structures. A critical analysis of the application of the frequency-domain linearized Navier-Stokes equations on the case of sound transmission above a corrugated plate with non-zero airflow was conducted. It was found out that the correspondence with the experiment is very limited in this case due to problems with the linearization of the hydrodynamical perturbations. An extension and clarification of the previously proposed phenomenological model for sound generation in corrugated pipes were given and the model was tested against the experimental data. In order to assess the influence of finite-amplitude sound propagation on the source-resonance coupling, a weakly-nonlinear model was proposed as an extension to the linear one. Next, it was investigated how the periodic arrangement of heat exchanger coolant tubes affects the sound propagation and whether it can be described as a sonic crystal. It was shown that even for finite structures consisting of four rows of coolant tubes the theory of wave propagation through periodic media is applicable and proves to be in accordance with the experiment. The noise generated by the unsteady flow through the tube array was investigated by numerical simulations. It was demonstrated that the radiated sound intensity is proportional to the previously derived dependence valid for a single cylinder and the Strouhal law governs the fundamental frequency.

Keywords: aeroacoustics, unsteady flows, periodic structures, sonic crystals, numerical simulations, corrugated pipe

Supervisor: doc. Dr. Ing. Michal Bednařík

Abstrakt

Tématem této dizertace je studium vybraných případů z oblasti aeroakustiky periodických struktur. Kritická analýza použitelnosti linearizovaných Navierových-Stokesových rovnic ve frekvenční oblasti na problém přenosu zvuku nad vroubkovanou deskou s prouděním ukázala, že aplikace tohoto výpočetního schématu odpovídá experimentu jen v hrubých rysech kvůli problémům s linearizací hydrodynamických poruch. Dříve navržený fenomenologický model generování zvuku ve vroubkovaných trubicích byl rozšířen a některé jeho aspekty byly blíže fyzikálně objasněny. Fenomenologický model byl srovnán s experimentálními daty a bylo navrženo jeho další rozšíření s ohledem na šíření slabě nelineárních vln konečných amplitud. V další části práce byly studovány vlivy periodicity uspořádání trubic tepelného výměníku na šíření akustických vln a možnost jejich popisu pomocí teorie sonických krystalů. Ta se podle srovnání s experimentem ukázala být relevantní už pro struktury o čtyřech řadách trubic. Generování šumu kvůli obtékání trubic bylo zkoumáno pomocí numerických simulací. Ukázalo se, že intenzita vyzářeného zvuku odpovídá tendencím odvozeným pro generování zvuku nestacionárním prouděním kolem válce a základní frekvence vyzařovaného zvuku se řídí Strouhalovým zákonem.

Klíčová slova: aeroakustika, nestacionární proudění, periodické struktury, sonické krystaly, numerické simulace, vroubkované trubice

Contents

Figures

Tables

Chapter 1

Introduction

In this thesis, two major branches of acoustic research meet: interaction of sound waves with periodic structures and the flow-acoustic interactions, commonly known as aeroacoustics. Their interweaving and distinct specifics form a thread running through the following, paragraphs, chapters and sections.

Although both aforementioned fields of study undertake different development and walked diverse paths through their evolution, the origins of both can be traced back to the last decades of the 19th century. In 1878, a Czech physicists Čeněk Strouhal, residing in Würzburg by that time, published a landmarking article *Über eine besondere Art der Tonerregung* (On an unusual way of sound excitation, [1]), in which he described specifics of the sound generated by unsteady flow past a cylinder. Despite the fact that the article consists predominantly of a description of the underlying experiments and their results, its clear and precise argumentation made it a cornerstone in the research of the sound generated by vortical flows. Soon after, in 1887, Lord Rayleigh published a work dealing with sound propagation through a medium exhibiting a periodic structure [2], in which the existence of band gaps were revealed.

The physics of waves propagating through periodic structures were mainly and widely studied in the field of solid-state physics and optics (see e.g., [3]). In analogy, the central concept of the acoustic waves scattering by specifically designed periodic structure is called sonic crystal (although it is disputable, sometimes this term is used even for one-dimensional structures, see e.g., [4]). The founding articles due to Kushwaha [5] and Sigalas and Economou [6] considered elastic waves in solid medium with solid inclusions. Its employment in acoustics considering a gas as the host medium gradually took place approximately from the mid-1990s (see e.g., [7, 8, 9]).

Conversely, the historical development of aeroacoustics was less interdisciplinary. If we disregard the omnipresent issue of drawing the borderlines dividing aeroacoustics, general fluid dynamics and applied mathematics, which is merely terminological, any overlaps with distinctly different fields of physics were rather rare – at least until recent developments in analogue gravity (see

e.g., [10]).

One of the main sources of motivation for the research in aeroacoustics was the rapid development of flight engines and applied turbomachinery in general, which took place in the second half of the 20th century. A symbolic cornerstone of modern aeroacoustics was laid in the 1950s in Lighthill's articles dealing with the aerodynamically generated sound [11, 12]. Since then, the theory was repeatedly generalized and reformulated (e.g. for the presence of moving bodies within the flow by Ffowcs Williams and Hawkings [13] to give just one notable example). It is not so straightforward to name the indubitable "epoch-making" texts in the field of duct acoustics with nonzero mean flow. However, one can point at the first edition of the first summarizing and subject-defining monography: the Munjal's *Acoustics of Ducts and Mufflers With Application to Exhaust and Ventilation System Design* issued in 1987 [14].

Both branches of research – the acoustics of periodic media and the aeroacoustics – are bound by several practical applications. Employment of corrugated pipes in various systems dealing with gas transport, benefiting from their local flexibility and global rigidity, presents a suitable example of a locally periodic structure with the nonzero mean flow (see e.g., [15]). The corrugated tube is often successfully described only as a (quasi-)one-dimensional system. To introduce another example with a more complex flow field, consider the periodic structure of heat exchanger tubes. In order to improve the exchange of heat, the thermoviscous boundary layer on the surface of the tubes is washed away with a flow set into motion by some type of fan. Hence, an exquisite example of the aeroacoustics of periodic structures is obtained: a mutual interaction of a sonic crystal with turbomachinery. Both given applications are studied in the sections below.

1.1 Current state of the art

As it has been pointed out, both "parental branches" relevant for this thesis are by no means new. Hence, there are numerous excellent textbooks or compendia on the aeroacoustics [16, 17, 18, 19, 20] as well as on the acoustics of periodic structures [21, 22, 23] covering the fundamental theory, most common workflows and specific computational frameworks.

Exact analytical solutions of the aeroacoustical problems without linearization often rely on the knowledge of the tailored Green's function belonging to the studied scenario (see e.g., [18]). Naturally, the amount of problems accessible by this approach is rather limited. As a consequence, computational aeroacoustics (CAA) became one of the most sublime disciplines of computational fluid dynamics. Lighthill himself claimed, that the numerical approaches shall form "the second golden age of aeroacoustics" [24]. Nevertheless, the development and validation of large-scale computational techniques (see e.g., the review [25]) are not within the scope of this work.

A long-standing problem – that is addressed in this thesis as well – is the disparity of length, velocity and time scales between hydrodynamical and acoustical phenomena (see e.g., [26] for a recent review or Sec. 2.4.3 here for some examples). In general, the framework of Reynolds averaging (RANS) gradually withers and the Large Eddy Simulation (LES) grows in importance (see e.g., [27]).

Currently, the acoustics of periodic structures, especially the design of the sonic crystals, had mastered the basic set of properties of bandgap formation along with other interesting effects such as effective negative refraction, self-collimation or beam formation (see e.g., [22] or the reviews [28, 29, 30, 31, 32]). Therefore, the focus can be turned to advanced and applied topics such as finite-amplitude nonlinear waves propagation (see e.g., [33]) or optimization of the structure properties by evolutionary algorithms (see e.g., [34]). The approach of significant importance for attenuation in the low-frequency range involves the combination of the periodic structure with local resonance (see e.g., [35] for an example of a specific design).

The aeroacoustics of the periodic structures is a topical theme. A recent review [36] describes the discipline as "still in its infancy". However, some industrial applications are already at hand (see e.g., [37]). When the flow through, past or along the periodic structure is present, some of the problems can be converted to the stagnant ones by means of Prandtl-Glauert or Taylor transform (see e.g., [38]). However, the number of specific applications regarding periodic structures that can be treated this way is very limited. As it is customary, many terms and techniques are transferred from solid-state physics and quantum mechanics. The Floquet-Bloch technique has been employed to study the wave propagation in waveguides with flow and periodic wall treatment (see e.g., [39, 40]). Generally, the presence of flow results in different transmission properties in the upstream and downstream directions. One of the possible approaches consists of introducing the so-called effective medium by means of homogenization (see e.g., [41] for the waveguide linings with flow or [42, 43, 44] for slow sound and acoustic black hole effects when the flow is present).

1.2 Aims of this thesis

Generally, this thesis is concerned with the acoustics of periodic media with nonzero mean flow. As it follows from the preceding paragraphs, the aeroacoustics of periodic structures can employ a wide variety of theoretical and numerical approaches. The goal is to choose appropriate ones while maintaining possibly elegant ways without unsuitable computational effort (such as direct numerical simulations of the compressible Navier-Stokes equations).

From the very broad topic, three specific scenarios with high application relevance were chosen to be closely studied. First, the sound transmission above a corrugated plate is treated (Sec. 3.1). The main question here is the

applicability of the linearized equations in the numerical simulations of sound propagation.

Subsequently, the possibility to formulate the problem of the corrugated pipes' whistling utilizing a phenomenological model is discussed and compared with experimental data (Sec. 3.2). A proposition of finite-amplitude propagation model is given as well (Sec. 3.2.5).

The third studied case is concerned with the opportunity to block some of the noise generated by axial fan by specifically designing the periodic arrangement of the heat exchanger tubes. The main aim of this section is to check that the calculation procedures derived for the infinite periodic structures (such as sonic crystals) apply here as well. The results are verified by comparison with experimental data (Sec. 4).

1.3 Note on terminology

Although the terminology is either well-known or defined as it goes along the course of the work, two general concepts should be mentioned before any further treatment. Terms such as "nonlinear" and "nonlinearity" are used in their broad mathematical sense. Any relation among the dynamic quantities that are not based on linear operations is labeled as nonlinear. Effects connected to the finite-amplitude nonlinearities are strictly introduced as such. Second, the word "acoustic" denotes the quantities and processes directly involving the compressibility of the fluid. Specifically, it denotes the compressibility phenomena connected to the wave motion (and it is commented below that no other are within the scope of this work). Somehow complementary to the acoustical effects are the "hydrodynamical" ones. It might seem odd, but this terminus is not necessarily associated with a medium but rather with its capability to be compressed (water is almost incompressible and hence the prefix "hydro-").

It is often tacitly assumed that the fluctuations are not driven by the unsteady heat fluxes, because no scenario of that nature is studied below. Therefore statements like "acoustic or hydrodynamic perturbations" cover all the possibilities (although they would not be universal enough in a very general case).

Chapter 2

Governing equations

Re-deriving the basic aeroacoustic equations does not belong among the goals of this thesis. However, it is convenient to briefly review some aeroacoustics and vortex sound theory elements to be referred to in the chapters below. Keeping in mind brevity and clear arrangement, only the most straightforward way is followed that leads from the very general equations governing the motion of compressible fluid to their specific approximations employed in the course of the thesis. A wide variety of other forms, different approaches and further comments might be found in fine textbooks on the subject, such as [45, 16, 18, 20]. Among the officially unpublished materials, the valuable textbooks by Avraham Hirschberg and Sjoerd Rienstra [46] and especially Jan Delfs [47] are worth mentioning.

Vector and tensor notation is preferred throughout the text. Its relation to the component-based form summarizes the Appendix A (see p. 97).

2.1 Medium and its constitutive relations

In the spirit of the just delimited aim, the first substantial reduction of generality is in place: the only medium considered is the air. Moreover, all introduced applications allow for the assumption of a perfect gas in local thermodynamic equilibrium. Therefore the following relations are conveniently at hand.

Pressure p, density ρ and (thermodynamic) temperature T are related by the ideal gas law

$$p = \frac{\rho R T}{M_m} \,, \tag{2.1}$$

with M_m and R denoting the molar mass and ideal gas constant, respectively. Changes of the specific internal energy e are directly related to the temperature changes by $\mathrm{d}e = c_V \mathrm{d}T$, where c_V is the specific heat capacity for the constant volume of the fluid. The validity of $\delta e = T\delta s - (p/\rho^2)\delta\rho$ is assumed, where

s is the specific entropy and δ denotes a change of thermodynamic variable when following a fluid particle. The equation of state can be expressed as

$$\delta\rho = \left(\frac{\partial\rho}{\partial p}\right)_s \delta p + \left(\frac{\partial\rho}{\partial s}\right)_p \delta s \,, \tag{2.2}$$

where the subscript after the brackets denotes the derivative at constant entropy and pressure, respectively. The derivatives could be evaluated making use of the ideal gas properties:

$$\delta\rho = \frac{1}{c^2}\delta p + \frac{1}{c_p}\delta s \,, \quad c^2 = \frac{\gamma p}{\rho} \,, \tag{2.3}$$

where c_p is the specific heat capacity at constant pressure and $\gamma = c_p/c_V$. Strictly speaking, at this point, c is just a convenient shorthand with physical dimensions of velocity.

Three important assumptions about the fluid's thermoviscous behavior consist of the validity of Fourier's heat law, the fluid being Newtonian, and the application of the Stokes hypothesis on the vanishing bulk viscosity. Apart from the special case of turbulent viscosity introduced below, all material parameters are assumed constant in time and space, independent of pressure and temperature. See e.g., [48, 49, 50] for more detailed discussion.

In the equations introduced below, the validity of the laws and relations introduced here are assumed without mentioning them explicitly.

2.2 Equations of motion of a compressible fluid

There is no need to re-derive and extensively comment on the Navier-Stokes equations for a compressible fluid. For the purposes of further manipulations, only two forms out of the many are introduced. Namely, it is the conservative form of the equations (that presents a convenient starting point to aeroacoustic analogies – see p. 18) and the form showing the time-evolution experienced by a fluid particle in motion (which comes in handy when dealing with linearization and transmission problems).

Although this point is not entirely free of controversy as some authors plead for a predominance of Newton's laws of motion (see e.g., [50]), here the conservation laws imposed on a control volume serve as the fundamental assumptions for further manipulations. Notably, but not exclusively, this approach is known from the books of Batchelor [48] in general fluid dynamics and Blackstock [49] in acoustics. Only the differential (local) form of the conservation laws is employed below.

2.2.1 Continuity equation

The fact that the change of the amount of mass inside the control volume must be balanced by the mass flux through the surface of the control volume (provided that there are no mass sources) is transformed to the local expression by the Gauss theorem yielding

$$\frac{\partial \rho}{\partial t} + \boldsymbol{\nabla} \cdot (\rho \boldsymbol{u}) = 0 \,, \tag{2.4}$$

where $\boldsymbol{u}$ denotes the fluid velocity. It is useful to note that the mass flux $\rho\boldsymbol{u}$ is in fact the momentum density as well. By expanding the second term and introducing the material derivative an expression for the density of a fluid particle is obtained:

$$\frac{\mathrm{D}\rho}{\mathrm{D}t} = -\rho \boldsymbol{\nabla} \cdot \boldsymbol{u} \tag{2.5}$$

2.2.2 Momentum equation

In the same manner as in previous section, the momentum conservation might be expressed in terms of momentum density $\rho\boldsymbol{u}$. For the following chapters it is convenient to show the effect of non-zero net volume force $\boldsymbol{f}$. The equation characterizing the balance reads:

$$\frac{\partial}{\partial t}(\rho \boldsymbol{u}) + \boldsymbol{\nabla} \cdot (\rho \boldsymbol{u}\boldsymbol{u} + p\mathbb{I} - \boldsymbol{\tau}) = \boldsymbol{f} \,, \tag{2.6}$$

where p and $\mathbb{I}$ denote pressure and identity matrix, respectively. The viscous stresses tensor $\boldsymbol{\tau}$ is defined employing Stokes' hypothesis as

$$\boldsymbol{\tau} = \mu \left[\boldsymbol{\nabla}\boldsymbol{u} + (\boldsymbol{\nabla}\boldsymbol{u})^{\mathrm{T}} + \frac{2}{3}\mathbb{I}\boldsymbol{\nabla} \cdot \boldsymbol{u} \right] \,, \tag{2.7}$$

with μ denoting the shear (dynamic) viscosity and $(\cdot)^{\mathrm{T}}$ the matrix transpose.

By expanding the second term in Eq. (2.6) and utilizing the continuity equation (2.4) the governing equation for the fluid particle velocity is obtained:

$$\rho \frac{\mathrm{D}\boldsymbol{u}}{\mathrm{D}t} = -\boldsymbol{\nabla} p + \boldsymbol{\nabla} \cdot \boldsymbol{\tau} + \boldsymbol{f} \,. \tag{2.8}$$

2.2.3 Energy equation

Equation describing the energy conservation in compressible fluid dynamics exists in a rich variety of forms. For the sake of brevity, the only form that is employed in the course of this work is introduced here. A domain without

heat and mass sources is considered. Making use of the constitutive relations given in Section 2.1 (p. 5) the specific internal energy and the heat flux are replaced by the already introduced dynamic variables and the temperature T. Finally, a governing equation for a pressure acting on a fluid particle is obtained:

$$\frac{\mathrm{D}p}{\mathrm{D}t} + c^2\rho\boldsymbol{\nabla}\cdot\boldsymbol{u} = \frac{c^2}{c_pT}\left(\tau : \boldsymbol{\nabla}\boldsymbol{u} - \kappa\nabla^2T\right) , \tag{2.9}$$

where c_p and κ denote the specific heat capacity at constant pressure and thermal conductivity, respectively. Note that for inviscid, thermally non-conducting fluid the right-hand-side of the equation vanishes. Then utilizing the continuity equation an useful relation between time-evolution of pressure and density is found (see e.g., [47]):

$$\frac{\mathrm{D}p}{\mathrm{D}t} = c^2\frac{\mathrm{D}\rho}{\mathrm{D}t} . \tag{2.10}$$

Another useful statement of the energy equation might be derived in the form containing the material derivative of the temperature [50]:

$$\rho c_p\frac{\mathrm{D}T}{\mathrm{D}t} - \frac{\mathrm{D}p}{\mathrm{D}t} = \kappa\nabla^2T + \tau : \boldsymbol{\nabla}\boldsymbol{u} , \tag{2.11}$$

which reflects the time-evolution of temperature and pressure acting on a fluid particle more conveniently for some applications, such as discussing the boudary conditions. The relation (2.10) is again obtained for inviscid and thermally non-conducting fluid upon substitution from the ideal gas law to the material derivative of temperature.

2.3 Nondimensional form of the equations

One of the most significant issues that is inherently present in virtually every aeroacoustic scenario is getting a proper scaling of variables involved in order to assess their physical interpretation and overall influence. In fact, it is the only thing that separates aeroacoustics from the general study of compressible flow dynamics.

2.3.1 Conditions of the flow incompressibility

It follows from Eq. (2.10) that for the isentropic (inviscid and thermally nonconductive) flow the density and pressure changes are proportional. Let the characteristic flow velocity be U and the characteristic length scale L, further assuming that L is small compared to the characteristic sound wavelength. The time scale is then set by U/L. If the reference value of the density is P, then the Bernoulli's theorem suggests that the pressure

variations caused by accelerating a fluid particle to the velocity U are of order PU^2. Formally:

$$\boldsymbol{u} = U\boldsymbol{u}^* , \qquad t = \frac{U}{L}t^* , \qquad p = PU^2 p^* , \tag{2.12}$$

$$\boldsymbol{x} = L\boldsymbol{x}^* , \qquad \rho = P\rho^* , \tag{2.13}$$

where the star $(\cdot)^*$ denotes a nondimensional quantity. Substituting these relations into Eq. (2.10) the following expression is obtained after some manipulations (see e.g., [48]):

$$\frac{\mathrm{D}\rho^*}{\mathrm{D}t^*} = \mathrm{Ma}^2 \frac{\mathrm{D}p^*}{\mathrm{D}t^*} , \quad \mathrm{Ma} = \frac{U}{c} , \tag{2.14}$$

where the so called Mach number is introduced in the second expression. Therefore, when $\mathrm{Ma}^2 \ll 1$, the density changes of the fluid particle are negligible:

$$\frac{\mathrm{D}\rho}{\mathrm{D}t} = 0 , \tag{2.15}$$

which according to Eq. (2.5) puts a constraint to the velocity field to be purely solenoidal (divergence-free):

$$\boldsymbol{\nabla} \cdot \boldsymbol{u} = 0 \tag{2.16}$$

Although this derivation was not without a loss of generality due to the assumption of isentropic flow, it could be shown by the perturbation techniques introduced below that for the domain without external heat sources, the thermoviscous contributions to the balance expressed by Eq. (2.10) are small.

2.3.2 Strouhal and Reynolds number

Suppose that the flow is incompressible. The divergence of the viscous stress tensor defined in Eq. (2.7) then simplifies just to $\mu\nabla^2\boldsymbol{u}$ and the fluid density is a constant denoted by ρ_0. Similar to the previous case, the scaling is introduced in order to investigate the effects of flow unsteadiness and viscosity. Assume that the characteristic length scale of flow variations is L, the characteristic velocity U and the characteristic angular frequency of flow instabilities ω. Then the scaling of the dynamic variables is as follows

$$\boldsymbol{u} = U\boldsymbol{u}^* , \qquad t = \frac{2\pi}{\omega}t^* , \tag{2.17}$$

$$\boldsymbol{x} = L\boldsymbol{x}^* , \qquad p = \rho_0 U^2 p^* . \tag{2.18}$$

Substituting these into Eq. (2.8) the scaled momentum equation is obtained after some manipulations:

$$\frac{1}{\mathrm{Sr}}\frac{\partial \boldsymbol{u}^x}{\partial t^*} + (\boldsymbol{u}\cdot\boldsymbol{\nabla}^*)\,\boldsymbol{u}^* = -\frac{1}{\rho_0}\boldsymbol{\nabla}^* p^* + \frac{1}{\mathrm{Re}}\nabla^{*2}\boldsymbol{u}^* \,, \tag{2.19}$$

$$\mathrm{Sr} = \frac{\omega L}{2\pi U} \,, \qquad\qquad \mathrm{Re} = \frac{\rho_0 U L}{\mu} \,, \tag{2.20}$$

where Sr and Re denote the Strouhal and the Reynolds number, respectively.

The Strouhal number reflects the influence of flow instabilities on the overall flow dynamics. Clearly, fast but slowly varying flows have a low Strouhal number and vice versa. As it is apparent from Eq. (2.19) the Strouhal number is directly related to the ratio of the local and the convective acceleration (the first and the second term in Eq. (2.19), respectively).

In the Reynolds number, the effect of momentum transport due to viscosity (as compared to convection and temporal instabilities) is reflected. Flows of low Reynolds number are governed by viscosity (the so-called Stokes' approximation), while, on the other hand, the viscous effects are relatively unimportant in the high Reynolds number limit.

There is no general law relating a specific value of Reynolds number to the outburst of turbulence within a fluid volume. On the other hand, as a rule of thumb (that has to be detailed for a specific scenario), the chance that a small flow perturbation will be attenuated by the viscosity decreases with increasing Reynolds number. In some cases, the so-called critical Reynolds number is known. For the flow speeds above the critical Reynolds number, any infinitesimal flow perturbation grows (see e.g., [51]). Therefore, although it is theoretically possible to have an unperturbed flow above the critical Reynolds number, it is highly unlikely to achieve such a state in experimental practice as well as in the time-domain simulations of the fluid dynamics.

Let this section be concluded with a specific example. Unsteady fluid flow through a corrugated pipe may result in its "singing" or "whistling". Typical wavelengths are related to the length of the whole pipe and therefore are much longer than the dimensions of one corrugation. Since the flow speeds in the piping are usually of low Mach number, it is reasonable to treat the fluid as effectively incompressible when investigating the flow details within a single corrugation or even a group of them.

To be even more specific, a corrugation pitch of 10 mm and the mean free-stream flow speed of 25 $\mathrm{m}\cdot\mathrm{s}^{-1}$ is considered. Then the Reynolds number connected to the flow instabilities evolving over the corrugation pitch is ca. 15 000, making the corresponding term in Eq. (2.19) very small. The typical Strouhal numbers are known for specific scenarios. Usually, a value of $\mathrm{Sr} \approx 0.4$ is given for the corrugated pipe whistling (see e.g., [52]). Therefore the local acceleration is ca. twice as big in magnitude compared to the convective one.

2.3.3 Comments on characteristic lengths in periodic structures

Characteristic lengths of periodic structures are naturally associated with the proportions of a single cell (i.e. an elementary unit of a repeating structure). Acoustic wavelengths for which the effects of the medium periodicity is most distinct might be of the same order. However, actually, a significant amount of effort has been spent in order to turn this feature. First and foremost, one of the ultimate goals of the metamaterials research is designing structures modifying the sound at subwavelength scales (see, e.g., [23]). A representative case is given here as well in Sec. 4.1.3.

Second, considering the scenarios with the flow, there is still the issue of scales disparity between the hydrodynamic and acoustic perturbations (see e.g., [26]). Quite often, it is only a relatively small component of the single cell that plays a role of the decisive geometrical proportion regarding the unsteady flow. To give some examples: the trailing edge radius of the single corrugation takes part on the Strouhal number definition (see Sec. 3.1); the diameter of the heat exchanger tube governs the frequency of vortex shedding even when the tube occupies only a few percent of the unit cell volume (see Sec. 4.2.3).

2.4 Linearization of the governing equations

Equations (2.5), (2.8), (2.11) together with the ideal gas law (2.1) constitute a closed set describing the motion of fluid particles:

$$\frac{\mathrm{D}\rho}{\mathrm{D}t} = -\rho\boldsymbol{\nabla}\cdot\boldsymbol{u}\,, \tag{2.21}$$

$$\rho\frac{\mathrm{D}\boldsymbol{u}}{\mathrm{D}t} = -\boldsymbol{\nabla}p + \boldsymbol{\nabla}\cdot\boldsymbol{\tau} + \boldsymbol{f}\,, \tag{2.22}$$

$$\rho c_p\frac{\mathrm{D}T}{\mathrm{D}t} - \frac{\mathrm{D}p}{\mathrm{D}t} = \kappa\nabla^2 T + \tau : \boldsymbol{\nabla}\boldsymbol{u}\,, \tag{2.23}$$

$$p = \frac{\rho R T}{M_m}\,. \tag{2.24}$$

This set is known as the compressible Navier-Stokes equations. Even numerical solutions to the complete set is highly demanding. In order to get insight into specific problems, some simplification is needed and a conveniently chosen linearization is one of the most employed approaches.

2.4.1 Fundamental assumptions of linearization for aeroacoustical problems

It is assumed that the dynamic variables might be decomposed to a sum of their mean values (denoted by a subscript 0) and departures from these

values (denoted by a prime) as follows

$$\rho(\boldsymbol{x},t) = \rho_0(\boldsymbol{x}) + \varepsilon\rho'(\boldsymbol{x},t)\ , \tag{2.25}$$
$$\boldsymbol{u}(\boldsymbol{x},t) = \boldsymbol{u}_0(\boldsymbol{x}) + \varepsilon\boldsymbol{u}'(\boldsymbol{x},t)\ , \tag{2.26}$$
$$p(\boldsymbol{x},t) = p_0(\boldsymbol{x}) + \varepsilon p'(\boldsymbol{x},t)\ , \tag{2.27}$$
$$T(\boldsymbol{x},t) = T_0(\boldsymbol{x}) + \varepsilon T'(\boldsymbol{x},t)\ , \tag{2.28}$$
$$\boldsymbol{f}(\boldsymbol{x},t) = \boldsymbol{f}_0(\boldsymbol{x}) + \varepsilon\boldsymbol{f}'(\boldsymbol{x},t)\ , \tag{2.29}$$

where ε is a small dimensionless parameter. Note that the mean values are constant in time but not necessarily in space. Generally, it is possible to allow for more terms in the expansion, which is usually called the weakly-nonlinear case (see, e.g., [53]). However, within this work, all terms of order $\mathcal{O}\left(\varepsilon^2\right)$ are considered negligible (the only exception being the Kuznetsov equation, see p. 58).

The classic acoustics of stagnant media relies on the assumption of constant p_0 and ρ_0 and completely vanishing $\boldsymbol{u}_0$. Here, the assumption is somewhat relaxed: the mean quantities shall satisfy the incompressible steady mean flow equations without any sources (i.e. $\boldsymbol{f}_0 = \boldsymbol{0}$). In the scenarios studied in this work the mean temperature field T_0 is constant in space (i.e. there are no hot gas exhausts, heated walls etc.). Therefore the mean flow quatntities must obey the following (see e.g., [47]):

$$T_0 = \text{const.}\ , \tag{2.30}$$
$$\boldsymbol{\nabla}\cdot(\rho_0\boldsymbol{u}_0) = 0 \tag{2.31}$$
$$\rho_0\left(\boldsymbol{u}_0\cdot\boldsymbol{\nabla}\right)\boldsymbol{u}_0 = -\boldsymbol{\nabla}p_0 + \boldsymbol{\nabla}\cdot\boldsymbol{\tau}_0\ , \tag{2.32}$$

where $\boldsymbol{\tau}_0$ is the viscous stress tensor defined in terms of $\boldsymbol{u}_0$ (and similar notation is employed below for its perturbations). The energy equation for the incompressible mean flow with uniform temperature distribution reduces to:

$$\tau_0 : \boldsymbol{\nabla}\boldsymbol{u}_0 = 0\ . \tag{2.33}$$

2.4.2 Linearized Navier-Stokes equations in time domain

Substituting the relations from the previous section to Eqs. (2.21)–(2.24) one obtains after some manipulations (see, e.g., [47, 54]):

$$\frac{\partial \rho'}{\partial t} + \rho_0 \boldsymbol{\nabla} \cdot \boldsymbol{u}' = -\boldsymbol{u_0} \cdot \boldsymbol{\nabla} \rho' \tag{2.34}$$

$$\rho_0 \frac{\partial \boldsymbol{u}'}{\partial t} + \boldsymbol{\nabla} p' - \boldsymbol{\nabla} \cdot \boldsymbol{\tau}' = -\rho' \boldsymbol{u}_0 \cdot \boldsymbol{\nabla} \boldsymbol{u}_0 - \rho_0 \boldsymbol{u}' \cdot \boldsymbol{\nabla} \boldsymbol{u}_0 - \rho_0 \boldsymbol{u}_0 \cdot \boldsymbol{\nabla} \boldsymbol{u}' \tag{2.35}$$

$$\frac{\partial p'}{\partial t} - \rho_0 c_p \frac{\partial T'}{\partial t} + \kappa \nabla^2 T' = \rho_0 c_p \boldsymbol{u}_0 \cdot \boldsymbol{\nabla} T' - \frac{\boldsymbol{u}_0 \cdot \boldsymbol{\nabla} p_0}{T_0} T' - \boldsymbol{u}_0 \cdot \boldsymbol{\nabla} p' - \boldsymbol{u}' \cdot \boldsymbol{\nabla} p_0 \tag{2.36}$$

where

$$\boldsymbol{\tau}' = \mu \left[(\boldsymbol{\nabla} \boldsymbol{u}') + (\boldsymbol{\nabla} \boldsymbol{u}')^{\mathrm{T}} \right] - \frac{2}{3} \mu \left(\boldsymbol{\nabla} \cdot \boldsymbol{u}' \right) \mathbb{I} \tag{2.37}$$

and the linearized viscous dissipation function has been omitted as small (see e.g., [47]).

The four quantities (ρ', $\boldsymbol{u}'$, p', T') are governed by three equations. The necessary closure is provided by linearization of the ideal gas law:

$$\frac{p'}{p_0} = \frac{\rho'}{\rho_0} + \frac{T'}{T_0} \,. \tag{2.38}$$

However, special attention must be given to the fulfillment of the linearity, along with the right interpretation of the perturbation quantities in specific cases. The following three subsections are dedicated to this problem.

2.4.3 Nature of perturbation quantities

A deeper understanding and physical intuition should be supplied to Eqs. (2.34)–(2.36) or their frequency domain equivalents. As mentioned in the Introduction, the "acoustic quantity" means the "quantity directly responsible for the propagation of the wave-like density perturbations". From the theory review up to this point it follows, that for a low Mach number flow and uniform T_0 distribution, it actually means any density perturbation. Provided with the above-introduced equations, the verbal description with appropriate formal representation is given now.

First, assume that $\boldsymbol{u}_0 = \boldsymbol{0}$, the fluid is inviscid and thermally non-conducting. For simplicity, let ρ_0 and p_0 be constant in space. In that case, it is possible to derive the classic (d'Alembertian) wave equation for the pressure or density perturbations:

$$\nabla^2 p' - \frac{1}{c_0^2} \frac{\partial^2 p'}{\partial t^2} = \boldsymbol{\nabla} \cdot \boldsymbol{f}' \,, \tag{2.39}$$

$$\nabla^2 \rho' - \frac{1}{c_0^2} \frac{\partial^2 \rho'}{\partial t^2} = \frac{1}{c_0^2} \boldsymbol{\nabla} \cdot \boldsymbol{f}' \,. \tag{2.40}$$

Clearly, the quantity $c_0 = \sqrt{\gamma p_0/\rho_0}$ represents the phase velocity of sound propagation. It is also clear that any solenoidal (divergence-free) force field does not interact with the acoustic field.

Problems arise, when the wave equation is derived for the velocity perturbations. Still under assumption of $\boldsymbol{u}_0 = \boldsymbol{0}$, it is straightforward to rearrange the first order equations and eliminate quantities to obtain:

$$\nabla^2 \boldsymbol{u}' + \boldsymbol{\nabla} \times \boldsymbol{\nabla} \times \boldsymbol{u}' - \frac{1}{c_0^2} \frac{\partial^2 \boldsymbol{u}'}{\partial t^2} = -\frac{1}{\rho_0 c_0} \frac{\partial \boldsymbol{f}'}{\partial t} \,. \tag{2.41}$$

Nevertheless, two traits separate the last expression from the wave equations given above. First, the left-hand-side operator contains the term $\boldsymbol{\nabla} \times \boldsymbol{\nabla} \times \boldsymbol{u}'$. Second, any unsteady force field may act as an effective source (even the solenoidal one).

In order to give this discrepancy a physical interpretation, recall, that the velocity field can be described by means of Helmholtz decomposition:

$$\boldsymbol{u} = \boldsymbol{\nabla}\varphi + \boldsymbol{\nabla} \times \boldsymbol{\Psi} \,, \tag{2.42}$$

where φ and $\boldsymbol{\Psi}$ denote the scalar velocity potential and the vector potential respectively.

Taking the divergence of Eq. (2.42) recalling that $\boldsymbol{\nabla} \cdot (\boldsymbol{\nabla} \times \boldsymbol{A}) = 0$ for any smooth vector field $\boldsymbol{A}$ one obtains:

$$\boldsymbol{\nabla} \cdot \boldsymbol{u} = \nabla^2 \varphi = \frac{1}{\rho} \frac{\mathrm{D}\rho}{\mathrm{D}t} \,, \tag{2.43}$$

where the last equality follows from the continuity equation (e.g. Eq. (2.21)). Similarly, $\boldsymbol{\nabla} \times (\boldsymbol{\nabla} h) = \boldsymbol{0}$ for any smooth scalar field h, which is empoyed to obtain:

$$\boldsymbol{\nabla} \times \boldsymbol{u} = \boldsymbol{\nabla} \times \boldsymbol{\nabla} \times \boldsymbol{\Psi} = -\boldsymbol{\nabla}^2 \boldsymbol{\Psi} = \boldsymbol{\omega} \,, \tag{2.44}$$

where the constraint $\nabla \cdot \boldsymbol{\Psi} = 0$ was assumed in the last equalities and $\boldsymbol{\omega} = \boldsymbol{\nabla} \times \boldsymbol{u}$ is the flow vorticity.

Two important facts follow from the last paragraphs. The scalar velocity potential is the only part of the decomposition that can be held responsible for the velocities connected to the density changes. On the other hand, the flow vorticity is associated solely with the hydrodynamic instabilities. Hence the definition of acoustic perturbation velocity $\boldsymbol{u}'_{\mathrm{ac}}$ in terms of the scalar velocity potential perturbations φ':

$$\boldsymbol{u}'_{\mathrm{ac}} = \boldsymbol{\nabla}\varphi' \,, \tag{2.45}$$

while keeping track of the vorticity development as the key to understanding the hydrodynamics of the process.

Equation (2.41) might be transformed to describe purely acoustical interactions by substituting the scalar velocity potential and requiring that the imposed force field undergoes the same treatment (i.e. that it shall be split into curl-free and divergence-free parts).

It is not necessary to continue such an analysis of the 2nd order wave equations here. However, it is of great importance to emphasize that in principle, one cannot be a priori sure of the true nature of the velocity field in Eqs. (2.34)–(2.36). Note that it is possible to have (at least locally) nonzero $\boldsymbol{u}'$ while maintaining unchanged ρ'.

Moreover, almost the same issues emerge when interpreting the pressure field perturbations p'. Similarly, there are pressure instabilities that do not change the density field. Clearly, it is possible to satisfy Eq. (2.35) while keeping $\rho' = 0$ and yet allowing for nonzero pressure and velocity perturbations. As far as they are incompressible, the linearized continuity (2.34) and energy equations (2.36) are fulfilled as well. Therefore, a careful discussion is needed before a velocity or pressure perturbation might be labeled as an acoustical one.

Eqs. (2.34)–(2.36) are arranged to show the flow-acoustic interactions. The left-hand-sides would be present unchanged if the classic acoustics of the non-moving medium was considered. The right-hand-sides contain terms due to the nonzero mean flow $\boldsymbol{u}_0$. Some of them can act as the sources to the ρ' field. However, it would be necessary to closely determine the source behavior due to the unsteady flow below.

To conclude, the inherent nonlinearity of the Navier-Stokes equations for a compressible fluid has been bypassed by means of linearization. Therefore, lots of techniques known from the acoustics of the non-moving media are readily at hand and the first order of the flow-acoustic interaction is present. On the other hand, questions of the perturbations' nature come along as the trade-off. Intuitively, there is also a question of the nonlinear flow-acoustic interactions. The latter two are partially solved within the theory of aeroacoustic analogies below.

2.4.4 Convected wave equation

Suppose that the fluid is inviscid and thermally non-conducting, there are no external force fields and only the plane waves in the x direction can propagate in a uniform flow $\boldsymbol{u}_0 = U_0\boldsymbol{e}_1$ (with U_0 and $\boldsymbol{e}_1$ denoting the mean velocity magnitude and the unit vector in x direction respectively). Such conditions are well-suited for the low-frequency wave propagation through a uniform duct with the flow if the mean flow profile can be replaced by the constant U_0 (the so-called plug flow).

Under these assumptions, a second order wave equation, called the con-

vected wave equation can be derived by eliminating among Eqs. (2.34)–(2.36):

$$\frac{\mathrm{D}^2 p'}{\mathrm{D}t^2} - c_0^2 \frac{\partial^2 p'}{\partial x^2} \equiv \frac{\partial^2 p'}{\partial t^2} + 2U_0 \frac{\partial^2 p'}{\partial x \partial t} - \left(c_0^2 - U_0^2\right) \frac{\partial^2 p}{\partial x^2} = 0 \,. \tag{2.46}$$

An important solution to this equation is a superposition of the downstream and upstream running waves:

$$p'(x,t) = p^+ \exp^{\mathrm{i}\omega t - \mathrm{i}k_+ x} + p^- \exp^{\mathrm{i}\omega t + \mathrm{i}k_- x} \,, \tag{2.47}$$

where p^+ and p^- denote the amplitudes of the downstream and upstream propagating pressure waves respectively and

$$k_\pm = \frac{\omega}{c_0 \pm U_0} \tag{2.48}$$

or

$$k_\pm = \frac{k_0}{1 \pm \mathrm{Ma}} \,, \quad k_0 = \frac{\omega}{c_0} \,. \tag{2.49}$$

Convected wave equation of the same form might be formulated for the acoustic velocity u' (note that the above given discussion about the nature of the velocity perturbation is considerably simplified in 1D case). Therefore a solution similar to Eq. (2.47) is relevant for the plane waves of acoustic velocity:

$$u'(x,t) = u^+ \exp^{\mathrm{i}\omega t - \mathrm{i}k_+ x} + u^- \exp^{\mathrm{i}\omega t + \mathrm{i}k_- x} \,, \tag{2.50}$$

where again the u^+ and u^- denote the amplitudes of the downstream and upstream propagating velocity waves, respectively.

For the case of uniform U_0 the acoustic pressure and velocity are bound by the linearized momentum equation in the form:

$$\rho_0 \frac{\partial u'}{\partial t} + U_0 \frac{\partial u'}{\partial x} = -\frac{\partial p'}{\partial x} \,. \tag{2.51}$$

Upon substitution from Eqs. (2.47) and (2.50) it is clear that the absolute values of propagating pressure and velocity waves' amplitudes are coupled by an (impedance) relation:

$$p' = \rho_0 c_0 u' \,, \tag{2.52}$$

which is the same result that is known from the classic acoustics of non-moving medium. This is very useful when determining the transmission coefficients of a duct with the flow (see Sec. 3.1). However, note that this is only a particular case, its simplicity owing to the uniform nature of U_0. Otherwise, more complicated relations take place.

2.4.5 Limitations of the linearized Navier-Stokes equations

It follows from the classical textbook analysis concerning the linear acoustics of stagnant media (see e.g., [49]) that the small density perturbations $\rho' \ll \rho_0$ correspond to the acoustic velocities small compared to the adiabatic speed of sound:

$$u_{\mathrm{ac}} \ll c_0 \tag{2.53}$$

and, in turn, the pressures connected to the acoustic density changes are small compared to the quantity $\rho_0 c_0^2$. It follows that the linearized approach covers a vast field of applications.

However, from the preceding section, it is clear that the fluctuations of acoustical nature constitute only a part of the (general) velocity and pressure perturbations. As a rule of thumb, it is a lot easier to satisfy the linearization assumptions for the acoustical part than the hydrodynamical one. As it has been pointed out above, the velocity and pressure are scaled differently for acoustical and hydrodynamical purposes. Therefore, the single linearization for both kinds of instabilities could be questionable.

Several hydrodynamical phenomena are essentially nonlinear. From the point of the linearized equations, they appear as exponentially growing perturbations. Usually, they are constrained by some nonlinear saturation mechanism that does not take part within the linearized framework. Among the most well-known cases, there are perturbations of a thin shear layer leading to its roll-up into discreet vortices (the so-called Kelvin-Helmholtz instability) and the boundary layer separation past the cylindrical objects forming characteristic alternating vortex pattern (the so-called von Kármán vortex street).

The mentioned phenomena are beyond description by the linearized Navier-Stokes equations due to a lack of nonlinear saturation. The possibility of their triggering potentially endangers the application of the linearized approach. Therefore different approaches were derived, splitting the compressible and incompressible parts of the whole system. They retain the linearity of the acoustical perturbations but allow for the coupling with the nonlinear formulation of the incompressible flow (see e.g., [55, 56]).

The major drawback is that this approach effectively prevents the acoustical equations from being transformed into the frequency domain. Since most of the techniques of solving wave propagation problems in periodic media are derived based on the time-harmonic framework, this is a severe obstacle. Therefore the linearization in the hydrodynamical part is sometimes assumed in order to employ specific techniques (such as the Floquet-Bloch approach, see e.g., [39]).

2.5 Aeroacoustic analogies

Fundamental ideas behind the so-called aeroacoustical analogies are quite different compared to the linearization considerations presented above. The main point is to show that there is a class of wave equations with sources arising from the fluid motions without any a priori prescribed forcing. Hence, all the conservation equations are considered without right-hand-sides.

2.5.1 Lighthill's analogy

The mass flux $\rho \boldsymbol{u}$ in the continuity equation is formally identical to the momentum density in the momentum equation. Eliminating this term by taking the time derivative of Eq. (2.6) and divergence of Eq. (2.4) the following expression is obtained

$$\frac{\partial^2 \rho}{\partial t^2} = \boldsymbol{\nabla} \cdot \boldsymbol{\nabla} \cdot (\rho \boldsymbol{u}\boldsymbol{u} + \mathbb{I} p - \tau) \ . \tag{2.54}$$

Now a term $c_0^2 \nabla^2 \rho$ is subtracted from both sides, which results in an expression formally resembling the wave equation

$$\frac{\partial^2 \rho}{\partial t^2} - c_0^2 \nabla^2 \rho = \boldsymbol{\nabla} \cdot \boldsymbol{\nabla} \cdot \left[\rho \boldsymbol{u}\boldsymbol{u} + \mathbb{I} \left(p - c_0^2 \rho \right) - \tau \right] \ , \tag{2.55}$$

where the quantity in the square brackets is often called the Lighthill's stress tensor. Note that at this point it is not necessary for c_0 to have any physical meaning other than it has to have dimensions of velocity. Provided that ρ_0 and p_0 are some density and pressure values that are constant in time and space, it is even possible to re-write the last equation in a form in which the (d'Alembertian) wave operator acts on the density perturbations:

$$\frac{\partial^2}{\partial t^2} (\rho - \rho_0) - c_0^2 \nabla^2 (\rho - \rho_0) = \boldsymbol{\nabla} \cdot \boldsymbol{\nabla} \cdot \left\{ \rho \boldsymbol{u}\boldsymbol{u} + \mathbb{I} \left[(p - p_0) - c_0^2 (\rho - \rho_0) \right] - \tau \right\} \ . \tag{2.56}$$

This expression suggests that the key to the motions of a compressible fluid is the wave equation with this special right-hand-side. Moreover, the equation is exact because no approximations have been imposed so far and therefore, it contains all nonlinear effects. However, there are some severe issues.

The single equation is still expressed in terms of the full set of variables. At this point of derivation, Eq. (2.56) is often (and rightfully) labeled only as a re-arrangement of the Navier-Stokes equations rather than their solution. The physical interpretation is not clear as well (there is no estimation of the perturbation magnitude; it is not clear what c_0 shall represent etc.).

Provided that the pressure and density perturbations are small, c_0 is the adiabatic speed of sound and the flow is isentropic, the middle term in the right-hand-side of Eq. (2.56) that represents entropy fluctuations vanishes. If the characteristic length of flow variations is small compared to the typical sound wavelength, then the argumentation from Sec. 2.3.1 (p. 8) applies here as well and for the low Mach numbers the source flow is effectively incompressible. The remainder of the Lighthill's stress tensor might be scaled the same way as in Sec. 2.3.2 (p. 9) to obtain:

$$\rho_0 \boldsymbol{u}\boldsymbol{u} - \tau = \rho_0 U^2 \left\{ \boldsymbol{u}^*\boldsymbol{u}^* - \frac{1}{\mathrm{Re}} \left[\boldsymbol{\nabla}^*\boldsymbol{u}^* + (\boldsymbol{\nabla}^*\boldsymbol{u}^*)^{\mathrm{T}} \right] \right\} . \tag{2.57}$$

It follows that the term $\rho_0 \boldsymbol{u}\boldsymbol{u}$ governs the dynamics for the high Reynolds numbers. Moreover, it is not the viscous stress tensor that acts as a source in Eq. (2.56), but its spatial variations. These are usually considered unimportant compared to the rapid evolution of flow instabilities. The term $\rho_0 \boldsymbol{u}\boldsymbol{u}$ is called the Reynolds stress because of its resemblance with the term arising from the Reynolds averaging of the Navier-Stokes equations (see Sec. 2.6.1, p. 25).

Therefore, in the low Mach and high Reynolds number limit the wave equation for the density perturbations generated by an unsteady flow reads (see e.g., [18]):

$$\frac{\partial^2 \rho'}{\partial t^2} + c_0^2 \nabla^2 \rho' = \boldsymbol{\nabla} \cdot \boldsymbol{\nabla} \cdot (\rho_0 \boldsymbol{u}\boldsymbol{u}) . \tag{2.58}$$

It is straightforward to show that the same equation holds for the pressure perturbations as well, but the identity only holds in the low Mach number limit. Otherwise, the term of fluctuating entropy is subject to a different operator of a different multipole expansion order [46]. That causes a controversy regarding Lighthill's analogy in hot flows, but that stays beyond the scope of this work.

In a broader context, what has been done in the last equations is transforming the problem of sound generated within the unsteady flow to an analogous non-moving medium (hence the term "analogy"). However artful it appears, there are two major drawbacks. First, not only the "acoustic sources per se" (meaning the actual sources supplying power to the field) but various other effects of kinematic nature due to sound field convection are described as "sources" (e.g. Doppler shifts, refraction at shear or boundary layers). Second, it is not rare that the turbulent fluctuations in the source domain are, to some extent, governed by the flow-acoustic interactions. Then the right-hand-sides of Eqs. (2.56) or (2.58) cannot be thought of as an independent source, but only as one of the constituents of a complex feedback-loop system.

On the other hand, the particular simplicity of Eq. (2.56) allows for the immediate application of theoretical tools known from classic acoustics of stagnant media, such as the Green's function solution. This will be discussed in the following section.

Regardless of the approximation, the right-hand-side of Lighthill's analogy for the density consists of the double divergence of a tensor. In terms of the multipole expansion, it means that the source is of quadrupolar order and therefore radiates relatively weakly to the far-field (see Appendix C). By further reasoning (not necessary to be detailed here), it is found that the mechanical efficiency of converting turbulent kinetic energy into sound is proportional to Ma^5 in the low Mach number limit (see e.g., [18]). This explains why it is often possible and well-justified to entirely neglect the aeroacoustic effects when the hydrodynamics of free-space turbulence is concerned.

2.5.2 Curle's analogy

The situation is different when solid bodies are present within the region of turbulence. There is a formal solution to Lighthill's analogy for the case of a non-moving body by Samuel Newby Curle, published shortly after Lighthill's constituting articles [57]. A further generalization for bodies of arbitrary motion, motivated by the problems of turbines and propellers, was found by Shôn Eirwyn Ffowcs Williams and David Hawkings [13]. Only the former is required by the following chapters. The latter is mentioned because, ahistorically, Curle's analogy is, in fact, the Ffowcs Williams-Hawkings analogy for non-moving bodies and sometimes it is referenced as such.

The key step is defining an auxiliary function $f(\boldsymbol{x})$ that is positive outside the rigid body and negative inside it (see Fig. 2.1). Subsequently, the Heaviside function $\mathrm{H}[f(\boldsymbol{x})]$ is introduced (see Appendix B, p. 99). It follows that it equals 0 for a point inside the body and 1 everywhere else. Let us suppose the low Mach and high Reynolds number limit, that the body is rigid and the no-slip condition applies on its surface. The wave equation for the density perturbations then takes the form [18, 57]

$$\frac{\partial^2}{\partial t^2}\left(\mathrm{H}\rho'\right) - c_0^2\nabla^2\left(\mathrm{H}\rho'\right) = \boldsymbol{\nabla}\cdot\left[\boldsymbol{\nabla}\cdot\left(\mathrm{H}\rho_0\boldsymbol{u}\boldsymbol{u}\right)\right] - \boldsymbol{\nabla}\cdot\left[\left(p'\mathbb{I} + \rho_0\boldsymbol{u}\boldsymbol{u}\right)\cdot\boldsymbol{\nabla}\mathrm{H}\right] \,. \tag{2.59}$$

Apart from the Heaviside function, the first term on the right-hand-side is the same as in the preceding case (Eq. (2.58)) and it is of quadrupolar nature. The second one represents the reaction of the body surface to the turbulent motions and by order, it is a dipole. It can be shown that the latter term is dominating for the low Mach numbers [18] and its efficiency of turning turbulent kinetic energy into sound scales with Ma^3, which is a significant intensification compared to the free-space turbulence.

An integral analogue of Eq. (2.59) is obtained by means of the three-dimensional free-space Green's function (see Appendix B, p. 99):

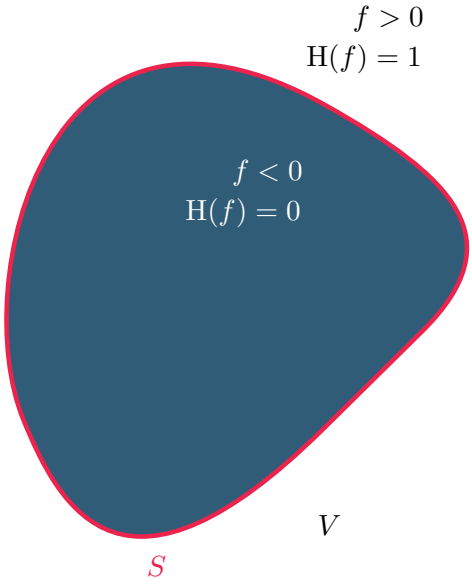

Figure 2.1: Illustration for the introduction of the Heaviside step function.

$$\left(\mathrm{H}c_0^2\rho'\right) = -\boldsymbol{\nabla}\cdot\oiint_S \frac{p'\left(t-\frac{|\boldsymbol{x}-\boldsymbol{y}|}{c_0}\right)}{4\pi|\boldsymbol{x}-\boldsymbol{y}|}\boldsymbol{n}\,\mathrm{d}S(\boldsymbol{y})\,, \tag{2.60}$$

where $\boldsymbol{n}$ is the (outer) normal vector to the surface S. In the far field (Fraunhofer) approximation ($|\boldsymbol{x}| \to \infty$, $p' = c_0^2\rho'$) it reads [18]

$$p'(\boldsymbol{x},t) \approx \frac{\boldsymbol{x}}{c_0|\boldsymbol{x}|^2}\frac{\partial}{\partial t}\cdot\oiint_S p'\left(t-\frac{|\boldsymbol{x}|}{c_0}+\frac{\boldsymbol{x}\cdot\boldsymbol{y}}{c_0|\boldsymbol{x}|}\right)\boldsymbol{n}\,\mathrm{d}S(\boldsymbol{y})\,. \tag{2.61}$$

Note that the integral represents an unsteady lift force:

$$\boldsymbol{F} = \oiint_S p'\left(t-\frac{|\boldsymbol{x}|}{c_0}+\frac{\boldsymbol{x}\cdot\boldsymbol{y}}{c_0|\boldsymbol{x}|}\right)\boldsymbol{n}\,\mathrm{d}S(\boldsymbol{y})\,. \tag{2.62}$$

2.5.3 Vortex sound theory

Despite the elegance of Lighthill's theory (counting in the Curle's solution), an important question still remains unresolved: what is the local fluid flow behavior that gives rise to the aeroacoustical sources? There is not much physical intuition on "the double divergence of the dyadic product of the velocity vector with itself". The issues with Curle's analogy are rather similar. The unsteady lift force is the dominant cause of sound production from the flow past the solid bodies. However, what is the typical condition under

which the flow exerts an unsteady lift force? This section is dedicated to a very condensed and limited review of the efforts to resolve such matters.

An often quoted statement, originally due to Ernst-August Müller and Frank Obermeier [58], says that "the vortices are the voice of the flow". The exceptional role of vortex motion in sound generation and the subsequent designation "the vortex sound theory" begins with the article of the same name by Alan Powell [59]. The first justification for such terms is given by expanding the source term in the Lighthill's wave equation (2.58):

$$\boldsymbol{\nabla}\cdot\boldsymbol{\nabla}\cdot(\rho_0\boldsymbol{u}\boldsymbol{u}) = \rho_0\boldsymbol{\nabla}\cdot(\boldsymbol{\omega}\times\boldsymbol{u}) + \frac{1}{2}\rho_0\nabla^2 u^2 \,, \tag{2.63}$$

where $\boldsymbol{\omega} = \boldsymbol{\nabla}\times\boldsymbol{u}$ is the vorticity and $u = |\boldsymbol{u}|$. If the sound-producing flow has a finite extent, the second term vanishes faster with the distance from the source than the first one (see [58] or Appendix C here). Hence, the second term is sometimes labeled as the "non-radiating source" (e.g., [58]).

There are well-established aeroacoustic analogies that build on the source terms explicitly containing the vorticity. Probably, a worldwide most renowned one is the analogy due to Michael Howe (e.g. [18]), while the central European authors often refer to the work of Wilhelm Möhring (e.g. [60]). In the following, Howe's approach is preferred, although Möhring's one would be possible as well after some manipulations.

The key underlying aspect is introducing a new aeroacoustic variable, the (specific) total enthalpy B:

$$B = i + \frac{1}{2}u^2 = e + \frac{p}{\rho} + \frac{1}{2}u^2 \,, \tag{2.64}$$

with $i = e + p/\rho$ denoting the specific enthalpy. This definition suggests that the total enthalpy consists of the enthalpy (as the heat content) and the kinetic energy of the macroscopic motion superimposed on the molecular motions governed by the Maxwell-Boltzman distribution.

Assuming the homentropic flow the wave equation for the total enthalpy fluctuations in the low Mach number limit is derived in the form [61]:

$$\frac{1}{c_0^2}\frac{\mathrm{D}_0^2 B'}{\mathrm{D}_0 t^2} - \boldsymbol{\nabla}^2 B' = \boldsymbol{\nabla}\cdot(\boldsymbol{\omega}\times\boldsymbol{u}) \,, \tag{2.65}$$

where

$$\frac{\mathrm{D}_0 B'}{\mathrm{D}_0 t} = \frac{\partial B'}{\partial t} + \boldsymbol{\nabla}\varphi_0\cdot\boldsymbol{\nabla}B' \,, \tag{2.66}$$

$$B' = \frac{p'}{\rho_0} + u' u_0 \,. \tag{2.67}$$

It follows that according to Howe's analogy, the listener is allowed to be placed in an irrotational mean flow rather than in the fluid at rest, which would be the Lighthill's case. In the far-field with vanishing mean flow velocity, the relation of the total enthalpy fluctuations to the acoustic pressure is simple:

$$p' = \rho_0 B' \ . \tag{2.68}$$

The quantity $\rho_0 (\boldsymbol{\omega} \times \boldsymbol{u})$ has the dimensions of force (more specifically, the volume density of a force, but the "density of" is often dropped for simplicity). It resembles the relation known from the theory of fictitious forces (not only) in rotating fluids (see e.g., [50]). Therefore, some authors call $\rho_0 (\boldsymbol{\omega} \times \boldsymbol{u})$ the Coriolis force. It provides an useful insight into the nature of the source term.

The "compressible behavior" of the $\boldsymbol{\omega} \times \boldsymbol{u}$ field is responsible for the generation (or dissipation) of the acoustic perturbations. Consequently, only the domains of nonvanishing vorticity has to be focused (in low Mach number flow). These are usually much less spatially extended compared to the domains of nonvanishing flow velocity, for which the Lighthill's stress tensor generally should be investigated. An illustrative example is given in Fig. 2.2. A flow issues from an inlet channel into free-space passing through a periodic lattice of a heat exchanger. Only in the vicinity of the coolant tubes and (to some extent) in their wake the vorticity is of importance.

The link with the pressure instabilities (as required by the Curle's analogy) is not complicated to be shown now. Considering the motion of incompressible, inviscid fluid, the Poisson equation for pressure might be derived by taking the divergence of the momentum equation (2.8) and employing the incompressibility constraint ($\boldsymbol{\nabla} \cdot \boldsymbol{u} = 0$):

$$\nabla^2 p = -\rho_0 \boldsymbol{\nabla} \cdot (\boldsymbol{u} \cdot \boldsymbol{\nabla} \boldsymbol{u}) = -\frac{1}{2} \rho_0 \nabla^2 u^2 - \rho_0 \boldsymbol{\nabla} \cdot (\boldsymbol{\omega} \times \boldsymbol{u}) \ , \tag{2.69}$$

where the identity $(\boldsymbol{u} \cdot \boldsymbol{\nabla}) \boldsymbol{u} = \boldsymbol{\omega} \times \boldsymbol{u} + \frac{1}{2} \nabla u^2$ was employed in the last step. It follows from the no-slip boundary condition for velocity that an appropriate boundary condition for the pressure equation at the rigid wall is $\boldsymbol{\nabla}_\perp p = 0$, where $\boldsymbol{\nabla}_\perp p$ is the gradient in the direction normall to the wall. Therefore, the pressure exerted by the fluid to the rigid body strongly depends on the value of $\boldsymbol{\nabla} \cdot (\boldsymbol{\omega} \times \boldsymbol{u})$ close to the wall.

Two remarks are given for the sake of completeness. There is a more general enthalpy-based analogy by Philip E. Doak [62], that allows for relaxing of some of the assumptions (such as nonconstant compressibility or nonvanishing vorticity and entropy gradients outside the source domain). The theory of analogies is rounded off by the concept of generalized acoustic analogy by Marvin E. Goldstein [63] showing the correspondence between the Navier-Stokes equations and the Euler equations with appropriately formulated sources, linearized around a well-chosen mean flow. The generality of neither is necessary in the following.

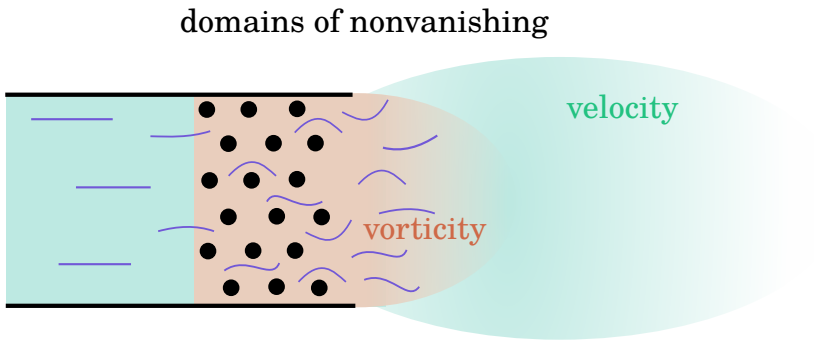

Figure 2.2: Schematic representation of the flow issuing from an inlet channel through a heat exchanger grille into a free-space. The domains of nonvanishing velocity (blue) and vorticity (red) are marked.

2.5.4 Howe's energy corollary

The last findings are conveniently expressed by the formula that is called the Howe's energy corollary (at least within this work – the terminology is not settled). It follows from the nature of the source in Eqs. (2.63) or (2.65) that the power imposed on the acoustic field might be evaluated utilizing the well-known relation that the instantaneous power (density) is calculated as $\boldsymbol{f} \cdot \boldsymbol{u}_{\mathrm{ac}}$. Let Ω denote a domain of nonvanishing vorticity. Then substituting the Coriolis-force-like term into the last expression the mean acoustic power $\langle \mathcal{P} \rangle$ supplied to the field (or dissipated from it) is given as [64, 46]:

$$\langle \mathcal{P} \rangle = \left\langle \int_{\Omega} -(\boldsymbol{\omega} \times \boldsymbol{u}) \cdot \boldsymbol{u}'_{\mathrm{ac}} \, \mathrm{d}\Omega \right\rangle , \tag{2.70}$$

where $\langle ... \rangle$ denotes an appropriate time averaging (e.g. over a period of the fundamental frequency of the unsteady base flow).

This formula is very important from multiple points of view. First, it is shown again that only the regions with nonvanishing vorticity contribute to the aeroacoustical sound generation and dissipation. Second, there is feedback between the acoustic field and the generating flow. Third, based on the orientation and phase relations among $\boldsymbol{\omega}$, $\boldsymbol{u}$ and $\boldsymbol{u}'_{\mathrm{ac}}$ the flow might be acoustically generative as well as dissipative. Fourth, the locations of the most pronounced sound generation or dissipation in a standing wave coincide with the acoustic velocity anti-nodes (not the pressure ones).

This is vital to the formulation of the phenomenological considerations introduced below (p. 44).

2.6 Equations related to turbulence in an incompressible fluid

Specific properties of turbulent motions in fluids are often considered one of the most challenging fluid dynamics topics in its theoretical, experimental and computational forms. Consistently adhering to the aim of this governing equations summary, only a very narrow sector of the turbulence modeling is reviewed.

Details of the theory and its applications to the numerical simulations might be found in various excellent textbooks (see e.g., [65, 66]). A regularly updated source listing the variety of models and their alterations along with validation cases is provided by NASA [67].

In this work, the mean flow velocities are of low Mach numbers and the length scale of hydrodynamic perturbations is small compared to the typical sound wavelengths, so that the fluid compressibility might be neglected for the turbulent flow modeling (see Sec. 2.3.1). Consequently, the Navier–Stokes equations are expressed as follows

$$\boldsymbol{\nabla} \cdot \boldsymbol{u} = 0 \,, \tag{2.71}$$

$$\rho_0 \frac{\partial \boldsymbol{u}}{\partial t} + \rho_0 \left(\boldsymbol{u} \cdot \boldsymbol{\nabla}\right) \boldsymbol{u} = -\boldsymbol{\nabla} p + \mu \nabla^2 \boldsymbol{u} \,. \tag{2.72}$$

This form is simpler than the full set of compressible equations (2.21) – (2.23). Nevertheless, the coupled equations (2.71), (2.72) are still nonlinear and there are some significant issues connected to the smallest spatial scale that must be resolved in order to get plausible results. Generally, a three-dimensional computational mesh should have a number of discrete points proportional to $\mathrm{Re}^{\frac{9}{4}}$ [50] shall all the major qualitative phenomena taking part in the turbulence dynamics be resolved. Therefore it is a matter of eminent application relevance to have a suitable approximate framework and to be aware of its strengths and weaknesses.

A simple and efficient solution to this issue consists of neglecting practically irrelevant scales by an appropriate averaging or filtering. From the two major approaches, RANS (see below p. 25) and LES (standing for the Large Eddy Simulations – see e.g., [68, 27]), only the former is employed within this work.

2.6.1 Reynolds-averaged Navier-Stokes equations

The key idea (dating back to Osborne Reynolds) is to get the mean flow field of turbulent flow by decomposing the instantaneous velocity and pressure fields to their mainstream and fluctuating values

$$\boldsymbol{u}(\boldsymbol{x},t) = \overline{\boldsymbol{u}}(\boldsymbol{x},t) + \boldsymbol{u}'(\boldsymbol{x},t) \;, \tag{2.73}$$

$$p(\boldsymbol{x},t) = \overline{p}(\boldsymbol{x},t) + p'(\boldsymbol{x},t) \;, \tag{2.74}$$

where the (Reynolds') averaging operator is defined as follows:

$$\overline{\boldsymbol{u}}(\boldsymbol{x},t) = \frac{1}{T}\int_0^T \boldsymbol{u}\left(\boldsymbol{x},t+s\right)\,\mathrm{d}s \tag{2.75}$$

where T denotes time span much longer than the typical fluctuation periods. The operation is similar for pressure or any other quantity. A more rigorous approach is built on argumentation replacing the somehow ill-defined time-averaging in Eq. (2.75) by the ensemble-averaging in a different sense (see e.g., [68]).

Note that nothing has been assumed about the orders of magnitude. There are cases (e.g. the wake behind a single tube of the heat exchanger – see Sec. 4) in which the fluctuation of the quantity is of the same order as its mainstream value. Therefore, it is necessary not to limit the magnitude of the fluctuations in a way that is common when linearizing the equations.

The governing equations for the turbulent mainstream are derived by substituting Eqs. (2.73)–(2.74) to the incompressible Navier-Stokes equations (2.21) – (2.23) and applying the averaging operator (2.75). After the outlined manipulations, the equations are obtained in the form:

$$\boldsymbol{\nabla}\cdot\overline{\boldsymbol{u}} = 0 \;, \tag{2.76}$$

$$\rho_0\frac{\partial\overline{\boldsymbol{u}}}{\partial t} + \rho_0\left(\overline{\boldsymbol{u}}\cdot\boldsymbol{\nabla}\right)\overline{\boldsymbol{u}} = -\boldsymbol{\nabla}\overline{p} + \mu\nabla^2\overline{\boldsymbol{u}} - \boldsymbol{\nabla}\cdot\left(\rho_0\overline{\boldsymbol{u}'\boldsymbol{u}'}\right) \;. \tag{2.77}$$

So the averaged quantities are governed by the same equations (called the Reynolds-averaged Navier-Stokes equations – RANS) as the original system, apart from the last term in the averaged momentum equation (2.77). It couples the mainstream and the fluctuation field. There is no rigorous way of obtaining its value from the averaged quantities. A straightforward attempt to employ the governing equations for fluctuations to use their solution for evaluation of $\overline{\boldsymbol{u}'\boldsymbol{u}'}$ only shows the persistence of the issue: a third-rank tensor $\overline{\boldsymbol{u}'\boldsymbol{u}'\boldsymbol{u}'}$ emerges as a vital part of the system. Similarly, it is possible to compose the next order of equations only to find out that a fourth-rank tensor is required and so on. This is the well-known problem of RANS closure.

The additional term in Eq. (2.77) is the so-called Reynolds stress and it has been encountered in this work before because its double divergence occurs at the right-hand-side of the Lighthill's wave equation (2.58). The definitions given here and in Sec. 2.5.1 does not match perfectly due to different context. In order to fully identify both Reynolds stress terms, a thorough discussion regarding the averaging time duration compared to the typical sound period

etc. would be needed. However, it is common in aeroacoustic literature to label the source term of the Lighthill's equation as the Reynolds stress tensor (see e.g., [18]) even though the Reynolds averaging does not belong among the steps of the Lighthill's analogy derivation.

2.6.2 Boussinesq assumption and Menter's k-ω SST model

The Reynolds stress is responsible for the mainstream momentum diffusion due to fluctuations. That it is indeed an another stress imposed on a fluid particle is more apparent by a slight re-arrangement of the right-hand-side of Eq. (2.77):

$$-\boldsymbol{\nabla}\overline{p}+\mu\nabla^2\overline{\boldsymbol{u}}-\boldsymbol{\nabla}\cdot\left(\rho_0\overline{\boldsymbol{u}'\boldsymbol{u}'}\right)=\boldsymbol{\nabla}\cdot\left\{-p\mathbb{I}+\mu\left[\boldsymbol{\nabla}\boldsymbol{u}+(\boldsymbol{\nabla}\boldsymbol{u})^{\mathrm{T}}\right]-\rho_0\overline{\boldsymbol{u}'\boldsymbol{u}'}\right\}\,. \tag{2.78}$$

The key idea is that since the turbulent fluctuations act on the mainstream properties as a factor contributing to the momentum diffusion, they might be phenomenologically replaced by some sort of effective viscosity. This approach is called the Boussinesq assumption (see [69] for the original article). Unlike the viscosity arising from the material properties, the turbulent eddy viscosity $\mu_T(\boldsymbol{x},t)$ is a true field (non-constant in space and time), because it reflects the local changes to the effective stress tensor (the right-hand-side of Eq. (2.78)) due to turbulent motions. Formally it is introduced as a part of the Reynolds stress tensor expansion:

$$-\rho_0\overline{\boldsymbol{u}'\boldsymbol{u}'}=\mu_T\boldsymbol{S}-\frac{2}{3}\rho_0 k\mathbb{I}\,, \tag{2.79}$$

where

$$\boldsymbol{S}=\frac{1}{2}\left[\boldsymbol{\nabla}\overline{\boldsymbol{u}}+(\boldsymbol{\nabla}\overline{\boldsymbol{u}})^{\mathrm{T}}\right]\,, \tag{2.80}$$

$$k=\frac{1}{2}\overline{\boldsymbol{u}'\cdot\boldsymbol{u}'}\,, \tag{2.81}$$

with $\boldsymbol{S}$ and k denoting the (averaged) strain-rate tensor and the turbulent kinetic energy, respectively.

Hence, the problem of RANS closure is transposed to finding equations governing the right-hand-side of Eq. (2.79). There are many different models attempting to solve this issue. Their overview might be found e.g. in [67]. In this work, only one of them is employed, the so-called k-ω shear stress transport (SST) model, originally designed by Florian Menter [70].

The full statement of the model equations is lengthy, but it is not necessary here because their coefficients nor any other part were edited in the following

sections. Implementation according to [71] is employed without changes. Therefore, only the main ideas are presented here in short.

The turbulent eddy viscosity in this model is proportional to $\rho_0 k/\omega$, where ω is the specific dissipation rate of the modeled turbulent motions (hence the k-ω in the name of this model). Menter's approach blends two older models: k-ω, suitable near the wall and k-ε, suitable in the free stream. Coefficients in the governing equations for ω and k change with the distance from the wall. Hence, it is possible to maintain a dedicated description of the boundary layers as well as the flow patterns in the free stream, which is important in the sections below.

Chapter 3

Sound transmission and generation along the corrugated surfaces

Surfaces with corrugations – regardless of whether they form a tube or a plate – are important in many industrial applications such as lining or piping. They can be found in a vast variety of machinery and devices: flexible risers, air-conditioners (e.g. [15]) or turbofan engine nacelles (e.g. [72]), to name some examples. Consequently, investigation of the acoustic waves traveling along such surfaces is of high practical relevance. The nature of the mentioned practical applications demands the presence of a nonzero mean flow within a studied device. Therefore, it is necessary to deal with the simultaneous presence of both the acoustical and hydrodynamical perturbations and their coupling.

Relevance for this thesis is apparent from the fact that the geometrical dimensions of a single corrugation are typically small compared to the size of the whole device. Hence, depending on the typical wavelengths investigated, the corrugated surfaces can form an effective one-dimensional locally periodic medium. It calls for exploiting the periodicity to simplify the description.

In the first part of this section, the possibility to linearize the governing equations describing the sound transmission above the corrugated plate is analyzed. Subsequently, the phenomenological model for the sound generation in a corrugated pipe is proposed.

3.1 Corrugated plate: Simulation of linear transmission

As it was shown above in the section dedicated to the aeroacoustic analogies, the equations describing complex flow-acoustic phenomena are generally nonlinear. However, the problems concerning sound transmission are often successfully described within the linearized framework (see, e.g., the comments in [41]). Frequently, the (quasi-)plane waves (defined by their angular frequencies, wave vectors, complex amplitudes etc.) are employed. It opens a

convenient possibility to exploit tools of the applied mathematics defined in the frequency domain (see, e.g., the textbook by Tam [73]). Moreover, many very useful and common acoustic quantities are defined only in the frequency domain (e.g., impedance or transmission coefficient).

Hence, it is natural to use the linearized frequency domain approach not only in theoretical considerations or experimental data processing but for numerical simulations as well – see e.g., the (presumably) founding article of Kierkegaard et al. [74]. Considering the aeroacoustics of periodic structures, there would be an appealing opportunity to exploit the framework known from the solid-state physics (see e.g., [3]): it shall be possible to reduce the description of the system to a single building block (the so-called unit cell) and employ the Floquet-Bloch theory to derive the features of the whole system. In a semi-analytical approach, it has been introduced to the field of aeroacoustics by Dai and Aurégan [39, 40]. However, the necessary condition for employing such an approach in the numerical simulations is, that the linearization is justified in the entire volume of the unit cell. As we shall see in the following paragraphs, this might be questionable.

This section is organized as follows: First, an experiment concerning sound transmission above the corrugated plate is introduced. Subsequently, the computational framework is proposed to obtain comparable transmission coefficients. The rest of the section is dedicated to a comparison of the experimental and numerical results, along with a discussion of the apparent discrepancies. The section is concluded with an evaluation of the Floquet-Bloch theory applicability.

3.1.1 Underlying experiment

The underlying experiment was described in detail in [75] (see Fig. 3.2). A rectangular channel with a mean flow of 24 $\mathrm{m} \cdot \mathrm{s}^{-1}$ and inner dimensions 40 mm by 50 mm has a corrugated wall. The 16 identical corrugations are 4 mm in width and depth. Their trailing edges are rounded with a 1 mm curvature radius. The length of a corrugation segment is 12 mm. See Fig. 3.1.

The main focus is the transmission coefficients of sound waves propagating downstream and upstream, respectively denoted as T^+, T^-. The experiments show (see [75]) that there are spectral bands exhibiting both lower and higher values of transmission coefficient compared to the one without flow (see Fig. 3.11 below). Besides, the Laser Doppler Velocimetry (LDV) measurement took place providing information about the unsteady flow at the corrugation.

3.1.2 Linearized Navier-Stokes equations in the frequency domain

Either by substituting $p'(\boldsymbol{x}, t) = \hat{p}'(\boldsymbol{x})e^{\mathrm{i}\omega t}$ (and similarly for the otehr quantites) or replacing the perturbation in Eq. (2.27) by

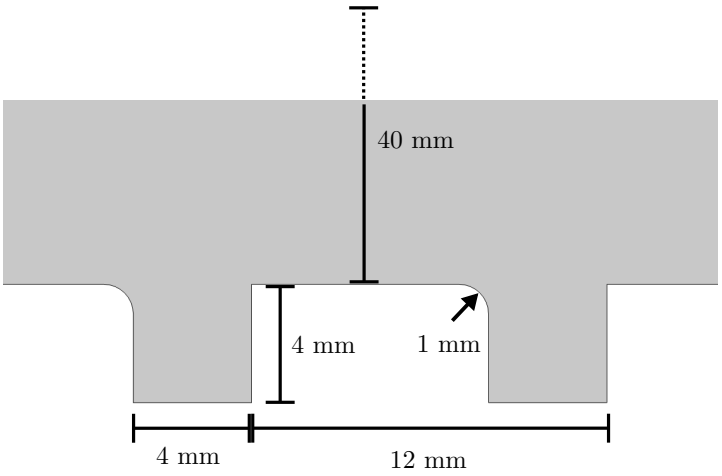

Figure 3.1: Geometry of the corrugated segment.

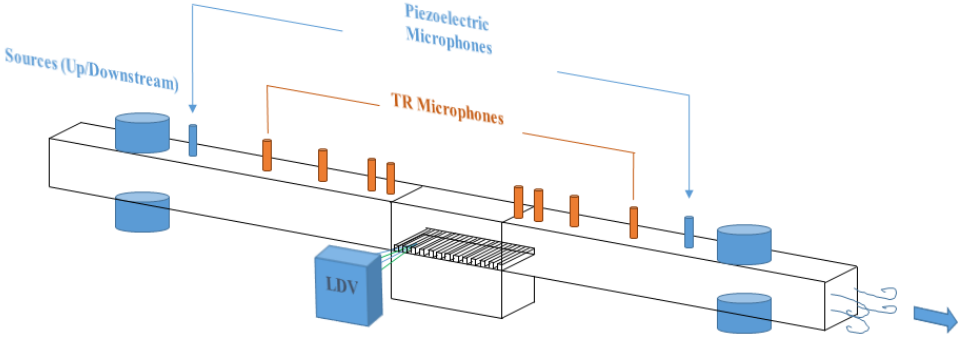

Figure 3.2: Sketch of the experimental setup from [75].

$$p(\boldsymbol{x},t) = p_0(\boldsymbol{x}) + \hat{p}'(\boldsymbol{x})e^{\mathrm{i}\omega t}\,, \tag{3.1}$$
$$\boldsymbol{u}(\boldsymbol{x},t) = \boldsymbol{u}_0(\boldsymbol{x}) + \hat{\boldsymbol{u}}'(\boldsymbol{x})e^{\mathrm{i}\omega t}\,, \tag{3.2}$$
$$\rho(\boldsymbol{x},t) = \rho_0 + \hat{\rho}'(\boldsymbol{x})e^{\mathrm{i}\omega t}\,, \tag{3.3}$$
$$T(\boldsymbol{x},t) = T_0 + \hat{T}'(\boldsymbol{x})e^{\mathrm{i}\omega t}\,, \tag{3.4}$$

the frequency domain counterpart of Eqs. (2.34)–(2.36) is obtained:

$$\mathrm{i}\omega\hat{\rho}' + \rho_0\boldsymbol{\nabla}\cdot\hat{\boldsymbol{u}}' = -\boldsymbol{u_0}\cdot\boldsymbol{\nabla}\hat{\rho}' \tag{3.5}$$
$$\mathrm{i}\omega\rho_0\hat{\boldsymbol{u}}' + \boldsymbol{\nabla}\hat{p}' - \boldsymbol{\nabla}\cdot\hat{\boldsymbol{\tau}}' = -\hat{\rho}'\boldsymbol{u}_0\cdot\boldsymbol{\nabla}\boldsymbol{u}_0 - \rho_0\hat{\boldsymbol{u}}'\cdot\boldsymbol{\nabla}\boldsymbol{u}_0 - \rho_0\boldsymbol{u}_0\cdot\boldsymbol{\nabla}\hat{\boldsymbol{u}}' \tag{3.6}$$
$$\mathrm{i}\omega\hat{p}' - \mathrm{i}\omega\rho_0 c_p\hat{T}' + \kappa\nabla^2 T' = \rho_0 c_p\boldsymbol{u}_0\cdot\boldsymbol{\nabla}\hat{T}' - \frac{\boldsymbol{u}_0\cdot\boldsymbol{\nabla}p_0}{T_0}\hat{T}' - \boldsymbol{u}_0\cdot\boldsymbol{\nabla}\hat{p}' - \hat{\boldsymbol{u}}'\cdot\boldsymbol{\nabla}p_0 \tag{3.7}$$

Note that in order to contain the amplitude as well as the phase information

$\hat{p}(\boldsymbol{x})' \in \mathbb{C}$, so the relation between the time-domain and frequency-domain perturbations is

$$p'(\boldsymbol{x}, t) = \mathrm{Re}\left[\hat{p}'(\boldsymbol{x}) e^{\mathrm{i}\omega t}\right] , \tag{3.8}$$

for given ω.

Note that the generality of the time-domain equations (2.34)–(2.36) is still contained in their frequency-domain version by Fourier's theory owing to the fact that all the equations concerned are linear.

The mean flow quantities ($\boldsymbol{u}_0$, p_0) must be provided by an appropriate simulation of the steady incompressible flow (see below). Mean temperature $T_0 = 293.15$ K is assumed constant (see Sec. 2.3.1).

3.1.3 Set-up of the numerical simulations

Due to the high computational demands, only a 2D slice of the experimental set-up is simulated.

The workflow of the numerical simulations follows an already established procedure (see e.g., [54, 76]), which is summarized in Fig. 3.3. The computations are set within the environment of Comsol Multiphysics 5.5 (and the results of the mean flow values were also verified by the finite-volume solver Ansys Fluent). First, the mean flow quantities are calculated assuming the incompressible flow with k-ω SST model. Before the mean pressure and velocity can be supplemented to the numerical evaluation of the linearized Navier-Stokes equations, it is necessary to map the mean quantities between the mesh appropriate for the turbulent flow calculation and the one designed to capture the acoustic features.

Although it is not that interesting from the aeroacoustical point of view, it is necessary to provide enough length downstream for the turbulent profile development (see Fig. 3.4). The inlet with prescribed velocity is therefore placed far from the domain of interest (about 40 channel diameters – which was checked as sufficient by evaluation of the centerline velocity). The outlet boundary condition is set as usual by considering zero (over-)pressure. The no-slip condition is imposed on the walls.

Simulations of the linearized Navier-Stokes equations (LNSE) take place in a smaller domain (because the prolonged inlet channel is not important in this case, see Fig. 3.5). A plane wave enters the system through a subdomain either upstream or downstream of the corrugations by prescribed superposition of the field quantities p', $\boldsymbol{u}'$, T' and the plane wave ones (in Comsol, this is called the background acoustic field – BAF):

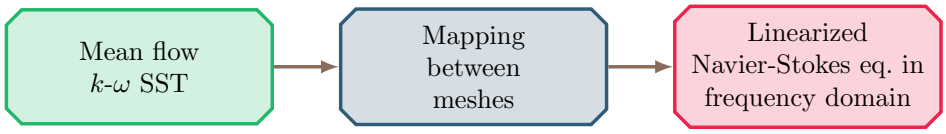

Figure 3.3: Workflow of the numerical simulations.

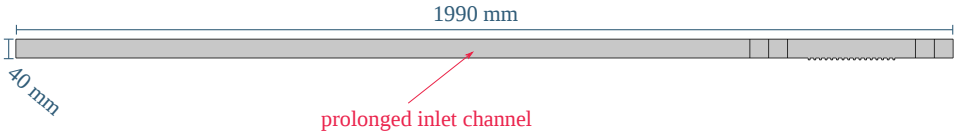

Figure 3.4: Geometry employed for the computation of the mean flow quantities.

$$\hat{p}' \to \hat{p}' + \hat{p}_{\mathrm{BAF}} e^{\mathrm{i}k_{\pm}x} \,, \tag{3.9}$$

$$\hat{u}_1' \to \hat{u}_1' - \frac{1}{\mathrm{i}\omega\rho_0}\frac{\partial}{\partial x}\left(\hat{p}_{\mathrm{BAF}} e^{\mathrm{i}k_{\pm}x}\right) \,, \tag{3.10}$$

$$\hat{u}_2' \to \hat{u}_2' \,, \tag{3.11}$$

$$\hat{T}' \to \hat{T}' + \frac{p_0 T_0}{\rho_0 c_p}\hat{p}_{\mathrm{BAF}} e^{\mathrm{i}k_{\pm}x} \,, \tag{3.12}$$

where $\hat{p}_{\mathrm{BAF}}$ is the pressure plane wave amplitude and $u_{1,2}$ denote the acoustic velocity components along the duct axis and perpendicular to it, respectvely. Note that as long as the system is linear, the transmission parameters are independent of its value. See p. 15 for definition of the convected wavenumbers $k_{\pm}$.

Perfectly matched layers [54] are set at both sides of the domain to attenuate the propagating and reflected waves. At the walls, the no-slip isothermal condition is imposed, i.e.:

$$\hat{\boldsymbol{u}}'_{\mathrm{wall}} = 0 \,, \qquad \hat{T}'_{\mathrm{wall}} = 0 \,. \tag{3.13}$$

The mean flow of 24 $\mathrm{m}\cdot\mathrm{s}^{-1}$ corresponds to $\mathrm{Ma} = 0.07$. The demand for transmission coefficients (along with the possibility of Floquet-Bloch approach) suggests that only the low-frequency limit allowing for quasi-plane wave propagation inside the duct stays in focus. Therefore the (first) cut-off frequency for the mentioned duct (ca. 3500 Hz) provides an upper frequency limit to the considerations.

There are multiple characteristic lengths to be taken into account when designing the computational meshes. First, the turbulent mean flow is considered. It is necessary to resolve the laminar viscous sublayer near the

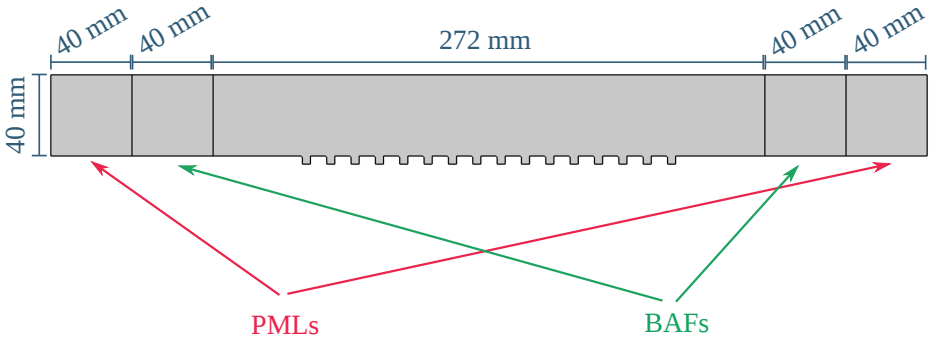

Figure 3.5: Geometry employed for the linearized Navier-Stokes equations computation.

walls. Its approximate extent is given by the dimensionless wall distance $y^+ < 5$ [50], where:

$$y^+ = \frac{\rho_0 y u_\tau}{\mu} \,, \quad u_\tau = \sqrt{\frac{\tau_{\text{wall}}}{\rho_0}} \,, \tag{3.14}$$

with the so-called friction velocity u_τ derived from the shear stress τ_{wall} exerted by the fluid to the wall. The value of the latter is unknown in general prior to the simulation. In order to get some insight, approximate relations are available. First, the wall shear stress is related to the free-stream fluid velocity U_∞ (see e.g., [50])

$$\tau_{\text{wall}} = C_f \left(\frac{1}{2} \rho_0 U_\infty^2 \right) \,, \tag{3.15}$$

where the proportionality constant C_f is called the skin (or Fanning) friction coefficient (or factor). There are multiple approximate ways of obtaining its value. Since here only the basic estimation is in place it is not necessary to discuss subtle differences. The so-called Prandtl's universal law of friction for smooth pipes is employed (see e.g., [50]):

$$\frac{1}{\sqrt{C_f}} = 2 \log_{10} \left(\sqrt{C_f} \text{Re} \right) - 0.8 \,, \tag{3.16}$$

which must be solved numerically. For the studied scenario $C_f \approx 0.0194$ and subsequently the friction velocity $u_\tau \approx 2.5\,\text{m} \cdot \text{s}^{-1}$. The laminar viscous sublayer thickness ($y^+ \approx 5$) is then assessed as 30 µm (see Fig. 3.6 for comparison with the simulated profile). Hence, the element closest to the wall was chosen to have a thickness of 12 µm (the elements were of the 2nd order for the velocity and the 1st order for the pressure). The element size

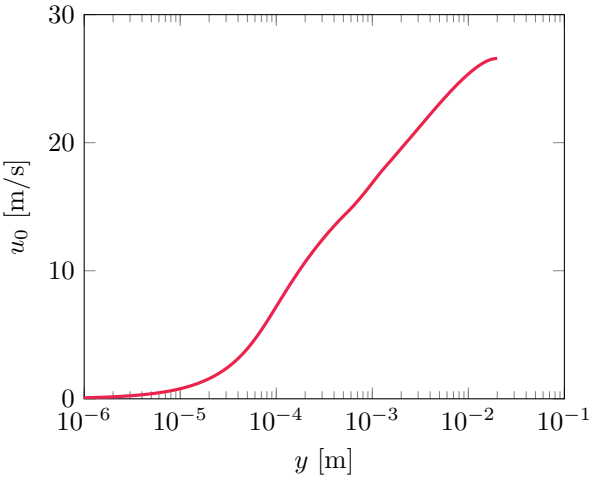

Figure 3.6: Mean flow profile upstream of the corrugated section. The viscous sublayer as well as the log-layer (see e.g., [50]) are clearly recognizable.

was allowed to grow up to 1.5 mm around the center of the flow profile, where the spatial variations almost cease.

Similarly, it is necessary to resolve the boundary layer mesh in the LNSE simulation. Estimation of the thermoviscous boundary layer thickness for the acoustic plane wave propagating above a plate with no-slip isothermal boundary condition ($\boldsymbol{u}'_{\text{wall}} = 0$, $T'_{\text{wall}} = 0$) is given by (see e.g., [49]):

$$\delta_\mu = \sqrt{\frac{2\mu}{\rho_0 \omega}}\,, \tag{3.17}$$

where ω and μ denote the angular frequency and the shear viscosity, respectively. For the highest below investigated frequency (3.5 kHz) $\delta_\mu \approx 37\,\mu\text{m}$ and consequently, the size of the element closest to the wall was chosen to be $10\,\mu\text{m}$ ($\approx \delta_\mu/4$). The mesh density cannot decrease too fast with the distance from the wall as there are multiple phenomena connected to the acoustically excited shear waves above the wall (see e.g., [61]) and the shear layer above the corrugation volume must be resolved as well. Therefore, the maximum size of the element was again 1.5 mm, which corresponds to ca. 61 elements per shortest wavelength investigated. Quadratic lagrangian elements were employed for all three perturbation quantities thus yielding a problem with 1,650,000 degrees of freedom.

In order to check that the results are indeed independent of the mesh parameters choice, the number of the elements above the corrugations, where most of the flow-acoustic phenomena take place, were doubled (see Fig. 3.7). Differences in the transmission coefficient values between the cases with and without mesh refinement were under 2 %.

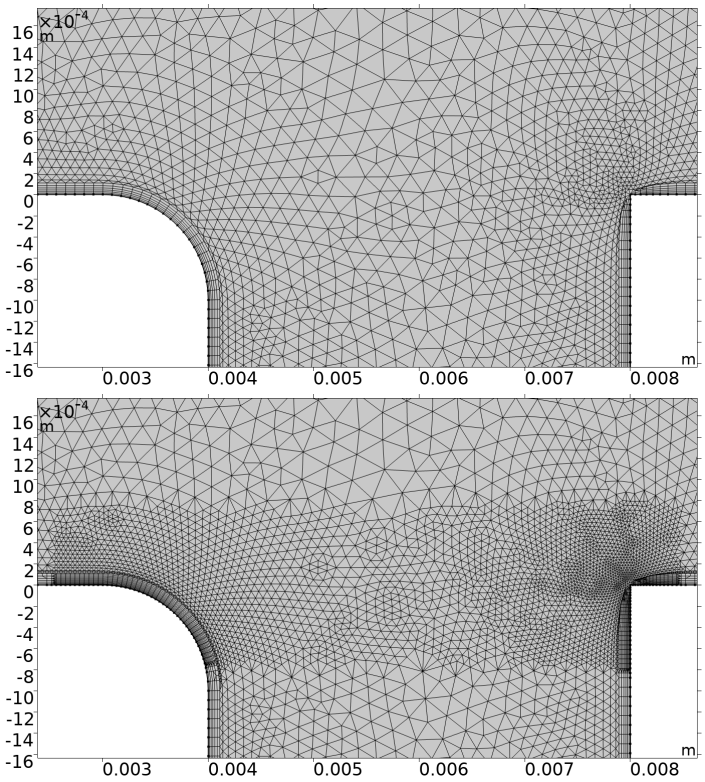

Figure 3.7: Illustration of the mesh refinement in order to verify independence of the results on the mesh parameters choice.

3.1.4 Results of the simulations

First, the mean flow results shall be reviewed in brief (see Figs. 3.8–3.10). Inside every corrugation, a vortex is formed similarly to the textbook benchmarking example of the lid-driven cavity flow (see e.g., [77]). The flow separation takes place at the trailing edge (see detail in Fig. 3.10) thus forming a shear layer above the corrugation volume. It follows from the above-given theory, that such locations with strong velocity gradients are of special interest for the aeroacoustics – most of the flow-acoustic phenomena take place there.

Subsequently, the focus shall be turned to the LNSE simulations. Amplitudes of the upstream and downstream propagating acoustic pressure waves are obtained employing the values of $p'(x,\omega)$ and $u'(x,\omega)$ averaged over the channel height and making use of the formulae arising from equations in Sec. 2.4.4:

$$\hat{p}^{+} = \frac{1}{2}\left(\hat{p}' + \rho_0 c_0 \hat{u}'\right) \ , \tag{3.18}$$

$$\hat{p}^{-} = \frac{1}{2}\left(\hat{p}' - \rho_0 c_0 \hat{u}'\right) \ . \tag{3.19}$$

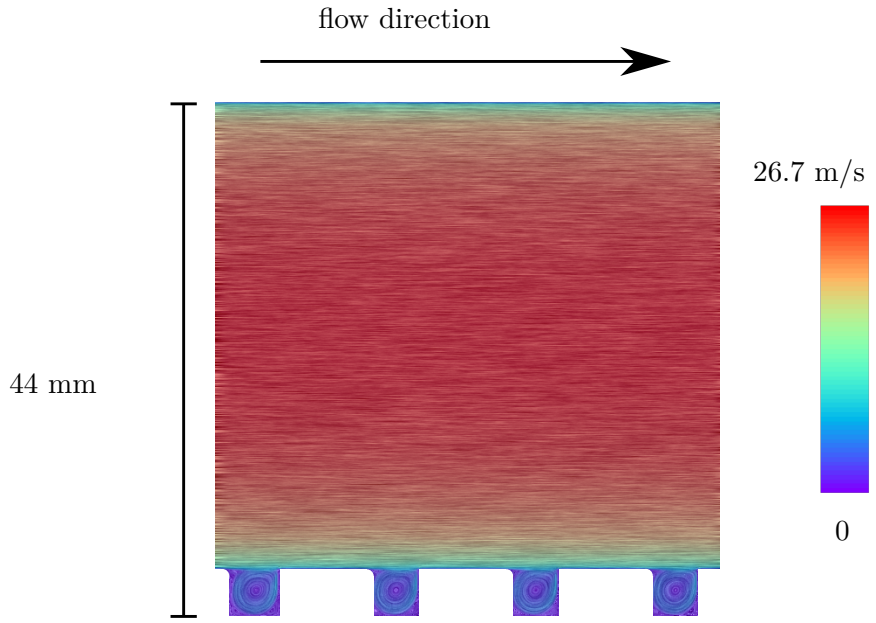

Figure 3.8: Mean flow in the channel with one corrugated wall. For clarity, only a part of the whole length is depicted. The visualization is made by the line integral convolution technique (LIC) (see e.g., [78]), the color scale reflects the velocity magnitude.

The plane wave transmission properties of the corrugated section might be described by the scattering matrix:

$$\begin{bmatrix} \hat{p}^{+}_{\mathrm{down}} \\ \hat{p}^{-}_{\mathrm{up}} \end{bmatrix} = \begin{bmatrix} \mathsf{T}^{+} & \mathsf{R}_{\mathrm{down}} \\ \mathsf{R}_{\mathrm{up}} & \mathsf{T}^{-} \end{bmatrix} \begin{bmatrix} \hat{p}^{+}_{\mathrm{up}} \\ \hat{p}^{-}_{\mathrm{down}} \end{bmatrix} , \tag{3.20}$$

where $\hat{p}$, T, R denote the amplitude of the pressure, transmission coefficient and reflection coefficient, respectively (generally, all the values are complex), while the subscripts up/down denote the evaluation upstream and downstream from the corrugated segment and superscripts $\pm$ mark the downstream and upstream propagation. For illustration, $\hat{p}^{+}_{\mathrm{up}}$ denotes the pressure amplitude of the downstream propagating wave evaluated upstream of the corrugation segment.

Generally, evaluation of both upstream and downstream wave propagation are required to obtain the scattering matrix components leading to a set of four coupled algebraic equations for T^{+}, T^{-}, R_{up} and $\mathsf{R}_{\mathrm{down}}$. However, the efficiency of the perfectly matched layers proves to be so good that the wave reflections from them are negligible. Therefore, the transmission coefficient calculation might be simplified:

$$\mathsf{T}^{+} \approx \frac{p^{+}_{\mathrm{down}}}{p^{+}_{\mathrm{up}}} , \qquad \mathsf{T}^{-} \approx \frac{p^{-}_{\mathrm{up}}}{p^{-}_{\mathrm{down}}} . \tag{3.21}$$

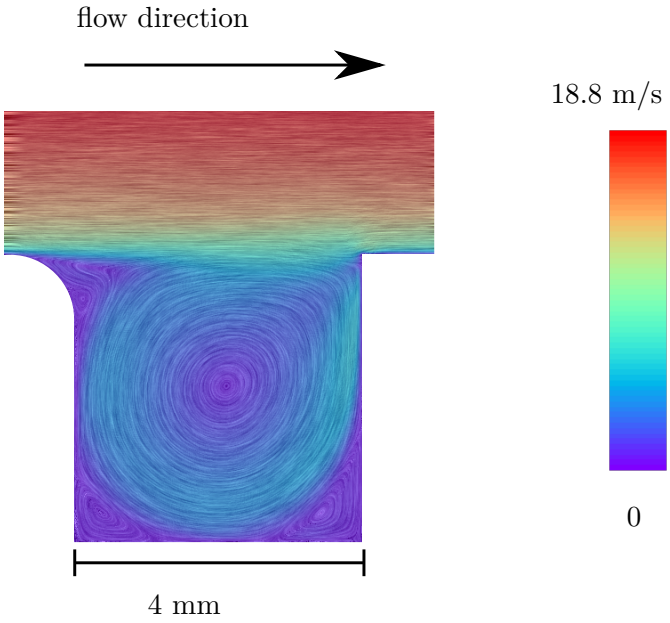

Figure 3.9: Detail of the mean flow inside a corrugation. The color scale reflects the velocity magnitude.

Results of the T^{+}, T^{-} computations are depicted in Fig. 3.11. Compared to the case without flow, there is a dip in the transmission around 1 kHz for both propagation directions. This feature qualitatively agrees well with the experimental results. Conversely, based on the experiment, there shall be a "gain" compared to the no-flow case at ca. 2 kHz. In the simulated curve we see an increase, but the value of $|\mathsf{T}^{\pm}|$ does not exceed the scenario without flow (it is rather aligned with it).

It follows from the above-given figures that the acoustic boundary layer is always thicker than the viscous sublayer of the mean flow, which means (see e.g., [79]) that there is an influence between the acoustic and turbulent attenuation and a non-negligible difference between downstream and upstream acoustic transmission shall be expected. This is in accordance with the results of the simulations.

The slope of the transmission coefficient without flow is different between the experiment and the simulation. This is due to the "missing walls" in the simulation set-up (the side walls of the channel are left out in 2D simulations along with their thermoviscous boundary layers).

Generally, the overall shape of the simulated transmission curves qualitatively corresponds to the experimental ones, but the absolute values of the transmission coefficient are different. The transmission minimum around 1 kHz should be deeper and the transmission maximum around 2 kHz should be much higher. Moreover, there is a slight shift in the frequency of the transmission maximum between the simulation and the experiment.

Before the analysis of the discrepancies between the experiment and the

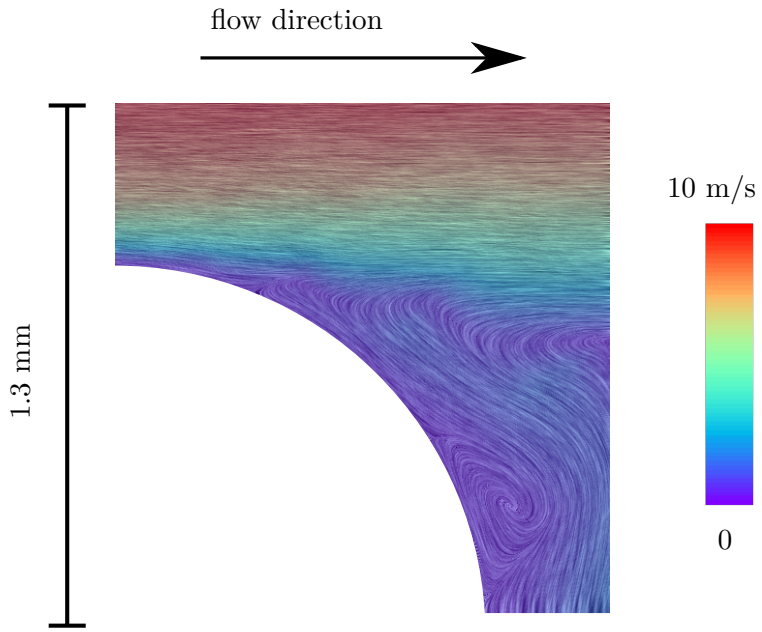

Figure 3.10: Flow separation at the trailing edge of the corrugation. The color scale reflects the velocity magnitude.

simulation proceeds, it is useful to investigate the tendencies in the transmission coefficient changes with variation of the mean flow parameters. Two parameters were altered: the mean flow velocity ($\mathrm{Ma} = 0.06, 0.07, 0.08$) and the trailing edge radii ($r = 0.5\,\mathrm{mm}, 1\,\mathrm{mm}, 1.5\,\mathrm{mm}$). Resulting T^+ coefficients are depicted in Fig. 3.12. First, T^+ is given as a function of frequency. Evidently, the positions of the transmission maxima and minima are dependent both on the mean flow velocity and the trailing edge radii. To reveal the mentioned dependence, it is beneficial to use the Strouhal number as the independent variable (i.e. to scale the frequency):

$$\mathrm{Sr} = \frac{f(W+r)}{c_0 \mathrm{Ma}}\,, \tag{3.22}$$

where W and r denote the corrugation width and the trailing edge radius, respectively. The choice of $W + r$ as the characteristic length is often justified (see e.g., [52]) by the fact that the rounding of the trailing edge shifts the point at which the flow separation takes place, thus enabling a longer path for the vorticity shed at the edge.

The transmission curves align in minimum at $\mathrm{Sr} = 0.2$ and this value is in agreement with the experimental results [75]. The minimum is deeper for higher flow speeds or sharper trailing edges and vice versa. The transmission maximum is located between $\mathrm{Sr} \approx 0.33 - 0.38$, which is a lower value than reported from the experiment (maximum at $\mathrm{Sr} \approx 0.4$ was found [75]). Again, the slope from the minimum to the maximum is steeper for higher flow speeds or sharper trailing edges and vice versa. However, one could intuitively expect

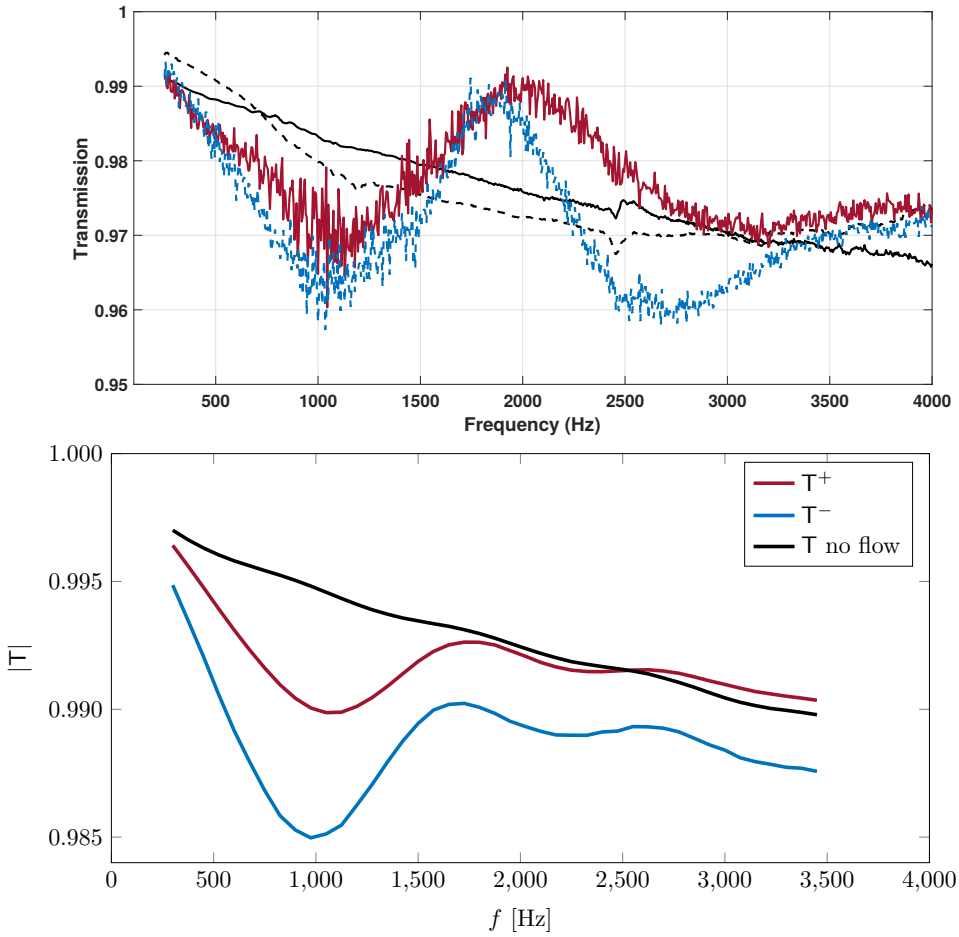

Figure 3.11: Top: Measured transmission coefficient above the corrugated plate [75]. T^+, T^- and T without flow in red, blue and black respectively (the dashed black with a reversed source-receiver configuration). Bottom: Simulated transmission coefficients.

bigger differences among the transmission curves given the ca. 15% variation of the Mach number.

Significant differences are found by investigating the perturbation velocity field at a single corrugation (specifically the 15th corrugation in the experiment as well as in the simulations, see Fig. 3.13). The frequency of 1800 Hz was used (i.e. the one closest to the transmission maximum). Velocity perturbations from the LNSE simulations (i.e. acoustic and hydrodynamic parts summed up) form a shear wave above the cavity extended over many corrugations. For comparison, the time-domain simulation of the incompressible unsteady RANS (URANS) equations in the time domain was conducted (with the inflow boundary condition perturbed with the same frequency as investigated in LNSE). In Fig. 3.13 the difference between the mean flow and an instantaneous velocity distribution (i.e. thy hydrodynamical perturbations) is depicted. Evidently, these are qualitatively different from the perturbation velocities

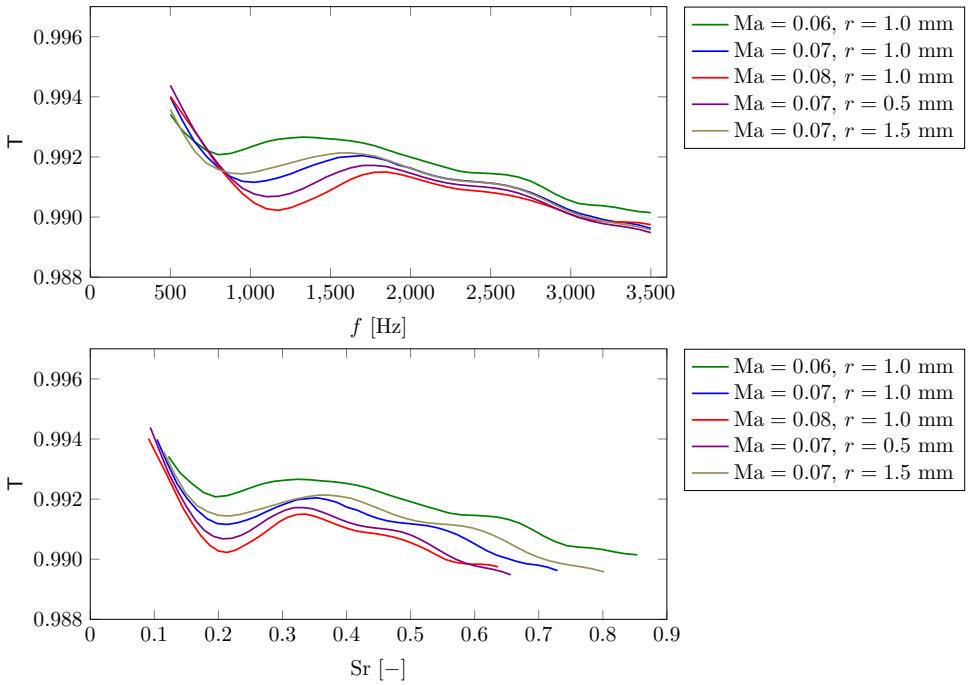

Figure 3.12: Transmission coefficients in the downstream direction for various flow speeds and radii of the corrugation trailing edges. Top: Transmission coefficient as a function of frequency. Bottom: Transmission coefficient as a function of Strouhal number.

predicted by LNSE: there are vortical structures with a very different typical length convected above the corrugation. Finally, the experimental results from the LDV measurements are given [75]. Clearly, they are much closer to the (nonlinear) URANS than to the linearized equations.

At this point, it is clear that some of the aspects of the numerical simulation results are in decent correspondence with the experimental data. Nevertheless, the impact of the flow on the transmission properties is generally weaker than expected and the local distribution of the perturbation velocities is qualitatively different from the experiments and URANS simulations.

It is assumed that the problem is the linearization of the hydrodynamical part of the equations. Although the convective nonlinearity of the acoustic velocities $\boldsymbol{\nabla}\varphi'$ is negligible for small density perturbations, an analogous constraint for the hydrodynamical perturbations $\boldsymbol{\nabla} \times \boldsymbol{\Psi}'$ is not at hand. Further note that the perturbations resembling the boundary layer separation (see Fig. 3.13) shall be governed by the (essentially nonlinear) Prandtl's equations (see e.g., [50]).

It follows that it is questionable to unconditionally maintain the single linearization for all perturbation quantities in the entire domain. On the other hand, the mentioned issue loses its significance with the distance from the non-planar boundary. It explains why the linearization of the conservation equations in the frequency domain can be successful despite

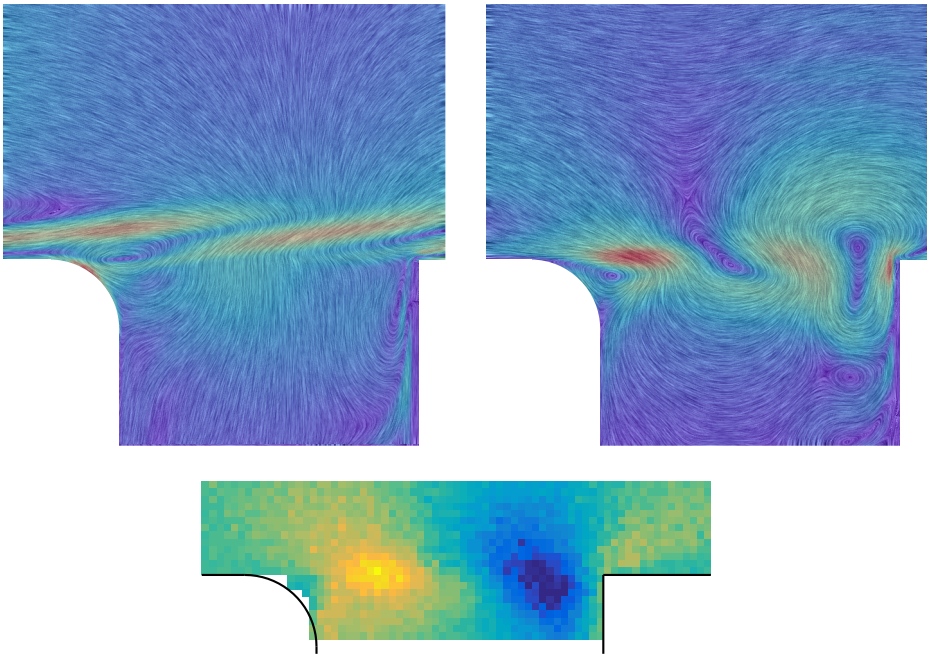

Figure 3.13: Three instantaneous perturbation flow fields under the same mean flow velocity (Ma = 0.07) and imposed frequency (1800 Hz). Top left: Linearized Navier-Stokes equations. Top right: URANS. Bottom: Experiment [75] (vertical velocity component only).

the just given reservations. For instance, if the geometrical discontinuities are effectively removed from the system by employing artificial impedance boundary condition obtained by homogenization (see e.g., [40]) or when the frequency domain approach serves as a basis for general reasoning (see e.g., [42]) or experimental data evaluation (see e.g., [41]), but not for simulations valid in each point in the domain.

In an influential article of Kierkegaard et al. [74], in which the frequency domain LNSE simulations are introduced, a slightly different scenario is studied in terms of material parameters of the fluid: due to high speeds even the mean flow is weakly compressible, but the isentropic relation between density and pressure is assumed (for the perturbation quantities as well). Moreover, it could be hypothesized that the discrepancies between the experimental and numerical results are significantly smaller for a single obstacle with a low amount of problematic regions (such as an orifice in the waveguide [74] or sudden duct expansion [80]) than for the periodic structure, in which the problematic locations are repeated and their mutual influence cannot be a priori excluded.

Note, that these considerations are of great influence for applicability of the Floquet-Bloch theory in the LNSE numerical simulations, as the periodic boundary conditions suggest that the problematic locations are repeated infinitely many times. Moreover, there is a technical issue connected to the finite element formulation: with non-zero mean velocities the equations yield

a non-Hermitian operator for the eigenvalue problem [81]. Therefore, the operator spectrum is continuous and extraction of the physically relevant eigenvalues is highly complicated.

3.2 Phenomenological model for the sound generation in corrugated pipes

The last sections dealt with the sound transmission properties in the linear regime. Therefore, the sound wave might be attenuated or reinforced by the flow-acoustic coupling, yet the wave itself is imposed on the system externally. However, it is possible that the sound might be generated from the unsteady flow without external driving. This is particularly well-known as the 'singing' or 'whistling' of the corrugated pipes (see e.g., the review [15]).

This inherently nonlinear phenomenon has been in focus of many articles dealing with the subject from the experimental point of view ([82, 83, 84, 85, 86, 87, 88, 89]) as well as the theoretical one ranging from simplified analytical formulations ([52, 86, 90]) to costly numerical simulations ([91, 92, 93]). In order to bypass solving the compressible Navier-Stokes equations retaining at least some of their nonlinearities, the motivation here is to find a suitable phenomenological formulation. It is known that the (quasi-)periodic shear layer instabilities might be phenomenologically replaced by the nonlinear oscillators of the van der Pol type. This way was widely employed by the authors dealing with the vortex-induced vibrations ([94, 95, 96, 97, 98, 99]) or in the field of general nonlinear mechanics as well (see, e.g., [100, 101, 102, 103, 104]).

This approach has already been proposed in the acoustics of flow excited resonators such as corrugated pipes ([105, 106]). The task here is to revisite its design in order to capture the key traits and incorporate them into the phenomenological model with subsequent testing against the experimental data.

3.2.1 Nature of the sources

Before proposing the specific form of the phenomenological equations, it is necessary to take a look at the qualitative behavior of the compressible fluid dynamics inside the corrugated pipe. Namely, to the process of the flow-acoustic coupling.

The root of the operation principle is the feedback-loop depicted in Fig. 3.14. Similarly to the case studied above, the hydrodynamic instabilities lead to vorticity shedding past the corrugation trailing edge. The convected vorticity acts as the sound source reinforcing the standing acoustic wave inside the pipe. In turn, due to the unstable flows sensitivity, the hydrodynamic instabilities are synchronized with the acoustic field, which leads to periodic behavior of the flow-acoustic perturbation field throughout the pipe.

The Howe's energy corollary (2.70) provides a suitable starting point for further considerations. In a standing wave, as prevails in the resonator, the sound is generated or dissipated at the acoustic velocity anti-nodes. Conversely, at the acoustic velocity nodes, the flow-acoustic interactions are

weaker. This behavior was confirmed by the experiments as well as the numerical simulations (see e.g., [92, 52]). The flow can produce as well as dissipate the sound based on the interplay between factors in Eq. (2.70) (i.e., regarding the phase and direction of the velocities and the vorticity).

The surface between the flow along the pipe axis and the fluid inside the corrugation constitutes an unstable shear layer. Hydrodynamic instabilities grow along the path over the corrugation. However, the nonlinear saturation phenomenon takes place as the flow perturbations do not grow infinitely. It occurs when the vorticity ascribed to the unstable shear layer rolls up to a flow pattern that resembles a point vortex (in planar cross-section along the pipe axis).

Let U denote a free-stream mean flow velocity in the bulk of the pipe and u_{ac} the acoustic velocity amplitude. The nonlinear saturation effects might appear already for the magnitudes ratio $u_{\mathrm{ac}}/U \approx 10^{-2}$. The oscillations exhibiting a good stability were found for $u_{\mathrm{ac}}/U \approx 10^{-1}$ (see e.g., [52, 107]).

Schematically, there are two mechanisms of the perturbations' generation. In an initial state, when the fluid is not yet insonified, the unconditional instability of the shear layer at the boundary of the corrugation volume must be considered. Practically, there is no possibility for the flow to be ideally steady and uniform. From inevitable flow instabilities the first very weak sound sources emerge. From these weak sources the sound field inside the pipe builds up and eventually the resonances corresponding to the pipe eigenfrequencies come along. Finally, the shedding of vorticity at the corrugation's trailing edge (synchronized with the acoustic velocity) constitutes the main sound source [52].

To sum up, a suitable phenomenological model is needed that would explain the sound generation in the corrugation segment. It follows from the review of aeroacoustic analogies (see p. 18) as well as from Eq. (2.70) that the nature of the sound source corresponds to a force driving. Taking into account the instability of the shear layer, a model shall be chosen that posses the ability to start up just from small random fluctuations around the equilibrium values. On the other hand, the nonlinear saturation mechanism has to be present. When the corrugation segment is much smaller than the wavelength (which is the usual case), the description could be simplified by considering the segment a point sound source. As it follows from the Howe's energy corollary, the feedback-loop between the source and acoustic field is governed by the acoustic velocity. Hence, the van der Pol-like oscillator ascribed to the point source with a right-hand-side proportional to local acoustic velocity fulfills the requested features. See Appendix D (p. 105) where the basic analysis of the van der Pol equation supports some of these claims.

Assume that the pipe diameter is much smaller compared to the pipe length. Therefore, the corrugated pipe is treated as an "open–open" one-dimensional resonator. It is apparent from the following how the equations could be derived for the "closed–open" case (e.g. a tube downstream of a choked valve). However, only the former is considered in the following.

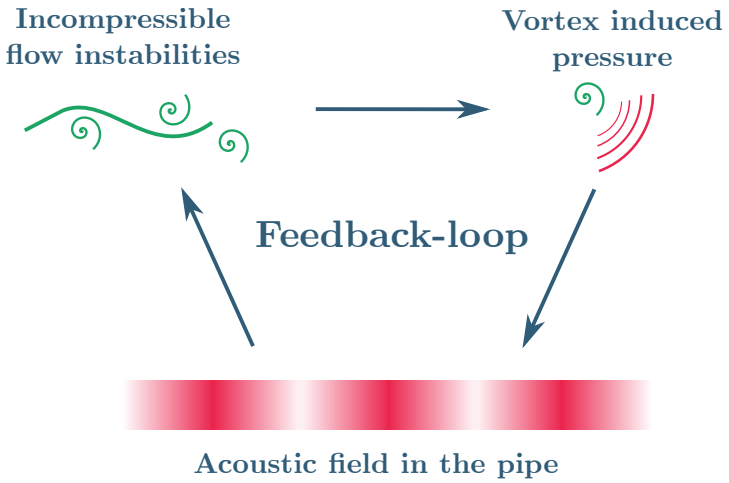

Figure 3.14: Schematic illustration of the feedback-loop mechanism.

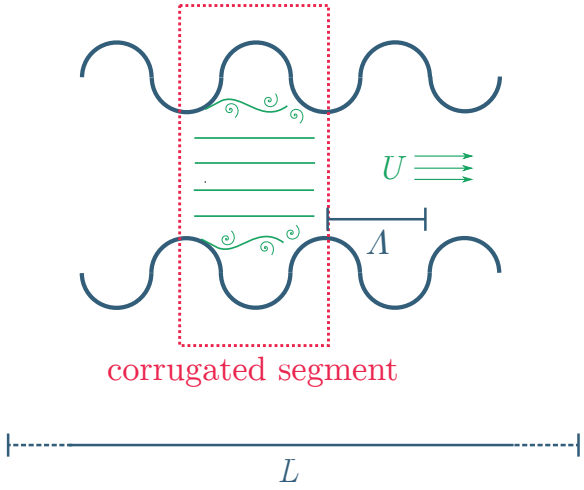

Figure 3.15: Schematic diagram of the quantities introduced to describe the corrugated segment.

3.2.2 Model equations

Suppose that the mean flow U is uniform and steady along the corrugated pipe of length L. The x axis is oriented along the centerline of the pipe. Elementary phenomenological acoustic pressure sources P_n are modeled by the van der Pol equation with a nontrivial right-hand-side. For a source P_n located at the n-th corrugation at x_n the following phenomenological equation can be defined (see e.g., [105, 106])

$$\frac{\mathrm{d}^2 P_n}{\mathrm{d}t^2} + A\omega_S \left[\left(\frac{P_n}{B\rho_0 U^2} \right)^2 - 1 \right] \frac{\mathrm{d}P_n}{\mathrm{d}t} + \omega_S^2 P_n = C \frac{\partial p'}{\partial x}\bigg|_{x=x_n} , \quad n = 1, ..., N , \tag{3.23}$$

ω_S is the Strouhal (angular) frequency, A, B and C are parameters of the

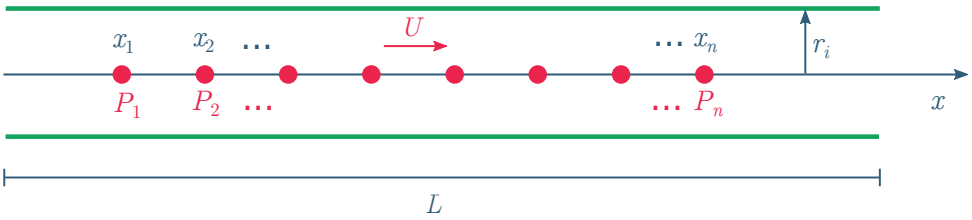

Figure 3.16: Diagram of the simplified phenomenological model for the sources inside the corrugated pipe.

source described below, ρ_0 is the constant mean air density and N represents the number of corrugations. Note that the spatial derivative of the acoustic pressure p' is proportional to the local acoustic acceleration. The Strouhal angular frequency ω_S is defined as

$$\omega_S = 2\pi \mathrm{Sr} \frac{U}{\Lambda} \,. \tag{3.24}$$

The characteristic length Λ is defined in the same manner as above: it is the width of the corrugation augmented by the trailing edge radius (see e.g., [52]). Here, the Strouhal number is considered to be a chcracteristic constant of the given system. Naturally, when the Strouhal number is obtained from the experimental data, it slightly varies due to mode-locking, hysteresis, etc. (see e.g., [89]).

It follows from the analysis in Appendix D as well as from the previous works on the related subjects (see e.g., [95]) that the nonlinearity parameter A may be and shall be small. Moreover, it is shown below that small variations of its precise value does not affect the system behavior significantly. The coefficient of coupling C has the dimension of acceleration. It reflects events linked locally to the single corrugation, its vorticity shedding frequency, and the sound field. The latter is represented by the (angular) frequency of the fundamental axial mode $\pi c_0/L$. Therefore the scaling is proposed in the form

$$C = -\frac{\pi c_0}{L} \omega_S \Lambda \Gamma \,, \tag{3.25}$$

where Γ is a nondimensional coefficient responsible for coupling. The minus sign reflects the fact that the acceleration is proportional to the negative pressure gradient in the momentum equations. The remaining parameter B is shown below to be governing the limit cycle size.

The highest values of vorticity are found at the trailing and leading edges of the corrugation. Therefore, the sound generation and dissipation due to the unsteady flow occurs predominantly in these regions. This feature is captured by assigning a van der Pol-like source to every corrugation. From the aeroacustic analogies (see p. 18) and the multipole expansion (see p. 102) follow that the nature of the source correspond to the dipole term resembling the external force distribution f'. Therefore, a suitable form of the wave equation for the acoustic pressure p' reads (see Eq. (2.39) above):

$$\frac{\partial^2 p'}{\partial t^2} - c_0^2 \frac{\partial^2 p'}{\partial x^2} = -c_0^2 \frac{\partial f'}{\partial x} \ . \tag{3.26}$$

The phenomenological force distribution is obtained as a sum of individual contributions from the sound sources P_n located at points x_n:

$$f' = \sum_{n=1}^{N} P_n \delta(x - x_n) \ , \tag{3.27}$$

where δ denote the Dirac delta function (see Fig. 3.16 for schematic illustration and Appendix B on p. 99 for the generalized functions properties).

For the time being, the thermoviscous and radiation losses are neglected. Hence, assuming that both of the open ends are ideal pressure release surfaces, the sound field inside the pipe can be expressed as the sum of orthogonal modes:

$$p'(x,t) = \sum_{m=1}^{M} q_m(t) \sin \frac{m\pi x}{L} \ . \tag{3.28}$$

Theoretically, the value of M shall approach infinity. However, for a practical case it is possible to truncate it at some finite integer without losing the decisive features. To further support this claim, note that the whole 1D considerations are limited by the low-frequency assumption.

Now, the orthogonality of the modes is utilized. Eq. (3.28) is substituted in Eqs. (3.23) and (3.26). Both sides of the wave equation are with spatial mode of consecutively changing mode number and integrated along the pipe length L. A set of $M + N$ ordinary differential equations is obtained for M modal amplitudes q_m and N phenomenological sources P_n:

$$\ddot{q}_m + \left(\frac{m\pi c_0}{L}\right)^2 q_m = \frac{2m\pi c_0^2}{L^2} \sum_{n=1}^{N} P_n \cos \frac{m\pi x_n}{L} \ , \tag{3.29}$$

$$\ddot{P}_n + A\omega_S \left[\left(\frac{P_n}{B\rho_0 U^2} \right)^2 - 1 \right] \dot{P}_n + \omega_S^2 P_n = -\frac{\pi^2 c_0}{L^2} \omega_S \Lambda\Gamma \sum_{m=1}^{M} m q_m \cos \frac{m\pi x_n}{L} \ , \tag{3.30}$$

where the dot denotes the derivative with respect to the time t.

At this point, the proposed system of equations is not realistic. Neglecting all losses would inevitably lead to infinite values of q_m for most cases. Hence, it is necessary to introduce losses and some other corrections into the idealized framework. These features supplement the previous attempts in [105, 106] and allows for to betterer assesment of the limits of the model.

First, the presence of the corrugations affects the local speed of sound, because the waveguide is not uniform. To account for the compliance of

the corrugations, the effective speed of sound in the low-frequency limit is introduced [108]:

$$c = \frac{c_0}{\sqrt{1 + \dfrac{V}{S\ell}}} \,, \tag{3.31}$$

where V, S, and ℓ denote the corrugation volume, the cross-sectional area of the pipe, and corrugation pitch respectively. Obviously, the effective sound speed c is always lower than the adiabatic speed of sound in the free-field c_0. The effective value c is employed henceforth.

Next, the length-correction due to nonzero radiation impedance is considered, taking into account the nonzero mean flow. There are multiple models describing this feature (see e.g., [109]). It is interesting to point out that this question has not been fully resolved for general flow parameters yet. Nevertheless, in all considered cases, the length correction is smaller than the tube radius r_i. Hence, if $r_i \ll L$, the importance of the end correction is negligible to the proposed phenomenological approach.

In order to discuss the introduction of losses, consider the formula due to Ingard and Singhal [110] for eigenfrequencies ω_m of the "open-open" duct with flow. Employing a slightly different notation for convenience and using the effective quantities introduced here it reads:

$$\omega_m = \left(1 - \mathrm{Ma}^2\right) \frac{m\pi c}{L} - \mathrm{i}\left(\delta_{\mathrm{tv}} + \delta_{\mathrm{turb}} + \delta_{\mathrm{end}}\right) \,, \tag{3.32}$$

where δ_{tv}, δ_{turb} and δ_{end} denote the (coefficients of) thermovisous losses, turbulent attenuation and end losses due to the convection respectively. The specific formula for the turbulent losses is disregarded here. The approximate relations are known for the smooth pipe, but for the corrugated one numerical calculations would be necessary. Finiteness of the van der Pol equation's limit cycle partially emulates these losses. Moreover, the search for the model parameters below shows that it is not necessary to artificially augment the other losses to compensate in order to maintain the desired qualitative behavior.

Now the task is to examine the relative magnitude of the remaining attenuation coefficients in the low Mach and high Reynolds number limit. The coefficients for a circular duct with $r_i \ll L$ are found as follows [110]

$$\delta_{\mathrm{tv}} = \frac{1}{2r_i}\sqrt{\frac{\omega_m \mu}{2\rho_0}}\left(1 + \frac{\gamma - 1}{\sqrt{\mathrm{Pr}}}\right) \,, \tag{3.33}$$

$$\delta_{\mathrm{end}} = \frac{2\left(1 - \mathrm{Ma}^2\right)c}{3L} \ln\left(\frac{1 + \mathrm{Ma}}{1 - \mathrm{Ma}}\right) \,, \tag{3.34}$$

where μ, γ and Pr denote the (shear) viscosity, the adiabatic exponent (the heat capacity ratio) and the Prandtl number respectively. In the low Mach number limit, Eq. (3.34) is expanded retaining only the leading terms:

$$\delta_{\mathrm{end}} = \frac{4c}{3L}\mathrm{Ma} + \mathcal{O}\left(\mathrm{Ma}^3\right) \ . \tag{3.35}$$

The term in brackets in Eq. (3.33) is approximately $\approx 3/2$. If the small frequency shifts due to the thermoviscous losses and nonvanishing flow are neglected, one obtains:

$$\frac{\delta_{\mathrm{tv}}}{\delta_{\mathrm{end}}} \approx \frac{9\sqrt{2}}{32}\sqrt{\frac{m\pi\mu L}{r_i^2 c\mathrm{Ma}^2}} \sim \frac{\sqrt{m}}{10} \ , \tag{3.36}$$

where the pipe radius in the order of centimeters, its length of meters and the Mach number $\sim 10^{-2}$ were assumed in the last expression. Hence, the end losses outweigh the thermoviscous ones even for relatively high frequencies. In the spirit of this estimation, the eigenfrequencies may be approximated

$$\omega_m \approx \frac{m\pi c}{L} - \mathrm{i}\frac{4c}{3L}\mathrm{Ma} \ . \tag{3.37}$$

Now, the modal equations (3.29) are altered by introducing a damping term that produces the same imaginary part as it would correspond to the last relation. Omitting again the terms of $\mathcal{O}\left(\mathrm{Ma}^2\right)$, the governing equations assume the form:

$$\ddot{q}_m + \left(\frac{8c}{3L}\mathrm{Ma}\right)\dot{q}_m + \left(\frac{m\pi c}{L}\right)^2 q_m = \frac{2m\pi c^2}{L^2}\sum_{n=1}^{N} P_n \cos\frac{m\pi x_n}{L} \ , \tag{3.38}$$

$$\ddot{P}_n + A\omega_S\left[\left(\frac{P_n}{B\rho_0 U^2}\right)^2 - 1\right]\dot{P}_n + \omega_S^2 P_n = -\frac{\pi^2 c}{L^2}\omega_S\Lambda\Gamma\sum_{m=1}^{M} m q_m \cos\frac{m\pi x_n}{L} \ . \tag{3.39}$$

It is useful to scale the equations and so the dimensionless quantities are introduced:

$$\sigma = \frac{\pi x}{L} \ , \qquad \tau = \frac{\pi c t}{L} \ , \tag{3.40}$$

$$\tilde{P}_n = \frac{P_n}{B\rho_0 U^2} \ , \qquad \tilde{q}_n = \frac{q_n}{B\rho_0 U^2} \ , \tag{3.41}$$

$$\xi = \frac{\omega_S\Lambda}{c}\Gamma \tag{3.42}$$

and hence

$$\ddot{\tilde{q}}_m + \left(\frac{8\mathrm{Ma}}{3\pi}\right)\dot{\tilde{q}}_m + m^2\tilde{q}_m = \frac{2m}{\pi}\sum_{n=1}^{N}\tilde{P}_n \cos m\sigma_n \ , \tag{3.43}$$

$$\ddot{\tilde{P}}_n + A\nu\left(\tilde{P}_n^2 - 1\right)\dot{\tilde{P}}_n + \nu^2\tilde{P}_n = -\xi\nu\sum_{m=1}^{M} m\tilde{q}_m \cos m\sigma_n \ , \tag{3.44}$$

where the dot denotes the derivative with respect to τ now and $\nu = \omega_S L/(\pi c)$ is the reduced driving frequency. The coefficients A, ξ, along with the Strouhal number Sr constitute the fitting parameters of the phenomenological system. It is clear that the coefficient B only scales the P_ns and q_ns and the system does not depend on it qualitatively.

The ad hoc added damping (the second term in Eq. (3.43)) is at least two orders smaller compared to m^2. Although any precise dependence is not known, it follows from the results below that the value of the coupling parameter ξ decreases with the number of corrugations.

3.2.3 Analysis of the equations

In order to analyze the proposed set of governing equations more closely, two standard techniques are employed. First, the linear stability analysis shows that the system is indeed capable of building up the oscillations from infinitesimal fluctuations. Next, the multiple scales perturbation method is utilized to show some of the nonlinear features. Both approaches are direct generalization of the techniques from the Appendix D (p. 105).

For clarity and simplicity, only a system consisting of one corrugation and one acoustic eigenmode (i.e. $M = N = 1$) is considered. This leads to a set of two coupled ordinary differential equations:

$$\ddot{\tilde{q}} + \left(\frac{8\mathrm{Ma}}{3\pi}\right)\dot{\tilde{q}} + \tilde{q} = \frac{2}{\pi}\tilde{P}\ , \tag{3.45}$$

$$\ddot{\tilde{P}} + A\nu\left(\tilde{P}^2 - 1\right)\dot{\tilde{P}} + \nu^2\tilde{P} = -\nu\xi\tilde{q}\ . \tag{3.46}$$

Despite the simplification, the set (3.45)–(3.46) is nonplanar and consequently the Poincaré-Bendixson theorem cannot be used to prove that there is a limit cycle [111]. Hence it is necessary to rely on the numerical results presented below.

Procedure of the linear stability analysis is well-known (see e.g., [111, 51] or Appendix D here), so only its outline is sufficient at this point. The dynamical system (3.45)–(3.46) is recasted as a set of four coupled differential equations of the 1st order:

$$\dot{\mathbf{X}} = \mathcal{F}(\mathbf{X})\ , \quad \mathbf{X} = [r, s, \tilde{q}, \tilde{P}]\ , \tag{3.47}$$

where $r = \dot{\tilde{q}}$ and $s = \dot{\tilde{P}}$. The sole equilibrium point is the origin itself (i.e. there is only for origin the equality $\mathcal{F}(\mathbf{X}_f) = 0$ holds). It is straightforward to show that adding more eigenmodes or corrugations ($M > 1,\ N > 1$) does not change that.

Next, small perturbations around the equilibrium values are introduced as $\mathbf{X} = \mathbf{X}_f + \mathbf{X}'$. Substituting this to the original system the following is obtained:

$$\dot{\mathbf{X}}' = \mathcal{L}\mathbf{X}' + \mathcal{O}\left(\mathbf{X}'^2\right) \ , \tag{3.48}$$

where $\mathcal{L}$ is the Jacobian $\mathcal{L} = \frac{\partial \mathcal{F}_i}{\partial X_j}|_{\mathbf{X}_f}$. Solution to the last problem is sought in the form $\mathbf{X}' = \overline{\mathbf{X}} e^{\lambda \tau}$. Therefore, the characteristc polynomial for λ reads:

$$\lambda^4 + (\zeta - A\nu)\,\lambda^3 + \left(\nu^2 - A\zeta\nu + 1\right)\lambda^2 + \left(\zeta\nu^2 - A\nu\right)\lambda + \frac{2\nu\xi}{\pi} - \nu^2 = 0 \ , \tag{3.49}$$

where ζ is a substitution for $8\mathrm{Ma}/3\pi$.

Applying the Routh-Hurwitz criterion (see e.g., [112]), at least one of the roots has a positive real part for any physically reasonable choice of the parameters. Therefore, the origin always repells the infinitesimal perturbations, which corresponds to the feature of building up the oscillations from the infinitesimal fluctuations. Numerical experiments on the values of λ were conducted for $\nu \in [0.5, 1.5]$, $A \in [10^{-3}, 10^{-2}]$, $\xi \in [10^{-5}, 10^{-1}]$. The resulting roots always exhibit a combination of stable and unstable focus (see e.g., [111, 51] for the terminology).

Next, a small nondimensional parameter ε is introduced in the following manner:

$$A = \varepsilon \ , \quad \frac{8\mathrm{Ma}}{3\pi} = \eta\varepsilon \ , \tag{3.50}$$

where $\eta \sim 1$. It follows that the damping term in (3.45) is of $\mathcal{O}(\varepsilon)$ as well.

Subsequently, to the order of ε^0 the following set of equations is obtained, that corresponds to two coupled linear harmonic oscillators in quantities P and q (the tildes are dropped henceforth for the sake of clarity):

$$\ddot{P} + \nu^2 P = -\nu\xi q \ , \tag{3.51}$$

$$\ddot{q} + q = \frac{2}{\pi} P \ . \tag{3.52}$$

Next, the linear tranformation is applied in order to decouple the equations:

$$\begin{bmatrix} P \\ q \end{bmatrix} = \begin{bmatrix} b & -1 \\ 4 & \frac{b}{2\pi\nu\xi} \end{bmatrix} \begin{bmatrix} y \\ z \end{bmatrix} \ , \tag{3.53}$$

where y, z are auxiliary variables and

$$b = \pi\left(1 - \nu^2\right) + \sqrt{\left(1 - \nu^2\right)^2 \pi^2 - 8\pi\nu\xi} \ . \tag{3.54}$$

Apart from the transformation the multiple scales expansion is employed:

$$\tau = \tau_0 + \varepsilon\tau_1 + \dots \,, \tag{3.55}$$
$$x = x_0 + \varepsilon x_1 + \dots \,, \tag{3.56}$$
$$y = y_0 + \varepsilon y_1 + \dots \,. \tag{3.57}$$

Very long expression are obtained after substitution of the last expressions to the original equations (3.45)–(3.46). Hence, for clarity only the equations containing the terms of order ε^0:

$$\frac{\partial^2 y_0}{\partial \tau_0^2} + \frac{b^2\nu^2 - 3\pi\nu\xi + 8b\nu\xi}{b^2 - 8\pi\nu\xi} y_0 = \mathcal{O}\left(\varepsilon^1\right) \,, \tag{3.58}$$
$$\frac{\partial^2 z_0}{\partial \tau_0^2} + \frac{b^2 - 8\pi\nu^3\xi - 8b\nu\xi}{b^2 - 8\pi\nu\xi} z_0 = \mathcal{O}\left(\varepsilon^1\right) \,. \tag{3.59}$$

When the terms of ε^1 and higher are neglected, the eigenfrequencies ω_y and ω_z are given as a square root of the respective linear term coefficients. Moreover, it follows from the full form of the equations that conditions for removing the ε^1 secular terms does not alter the ω_y, ω_z in this case. After some algebraic manipulations the expressions for the eqigenfrequencies are obtained:

$$\omega_y = \frac{1}{\sqrt{2\pi}} \sqrt{\pi\left(\nu^2+1\right) - \sqrt{\left(1-\nu^2\right)^2\pi - 8\nu\xi}} \,, \tag{3.60}$$
$$\omega_z = \frac{1}{\sqrt{2\pi}} \sqrt{\pi\left(\nu^2+1\right) + \sqrt{\left(1-\nu^2\right)^2\pi - 8\nu\xi}} \,. \tag{3.61}$$

Classic perturbation methods might not be sufficient to capture the mode-locked regions where the strong nonlinear effects take place. Note that rapid changes occur both in slow in fast substystems (see e.g., [113]). In the simplified case ($M = N = 1$), it is the solution in the neighborhood of $\nu = 1$.

The analytical values of ω_x exhibit good correspondence with the numerical solutions well below $\nu = 1$. At the certain threshold $\nu_{\min}$ the eigenfrequencies ω_x and ω_y begin to be complex-valued (and conversely start to be real-valued again at $\nu_{\max}$). The domain $\nu \in (\nu_{\min}, \nu_{\max})$ agrees very well with the mode locked-region identified in numerical solutions (see Fig. 3.17).

The frequencies are complex-valued when

$$\left(1-\nu^2\right)^2\pi - 8\nu\xi < 0 \,. \tag{3.62}$$

The quartic inequality is analytically solvable for given coupling parameter ξ. However, the results are very unwieldy and numerical solution is preferable.

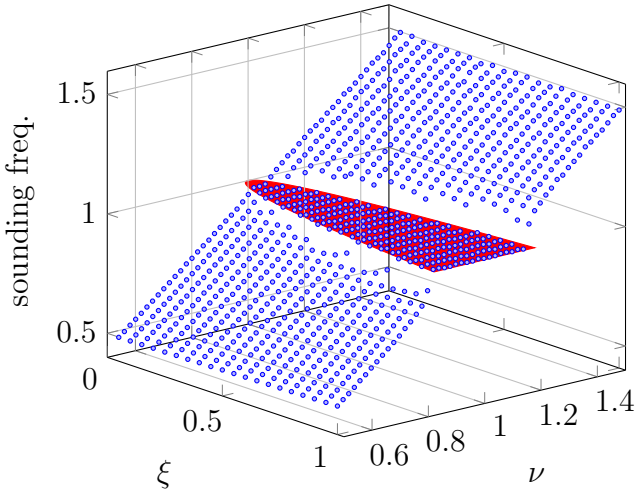

Figure 3.17: The dots corresponds to the steady-state angular frequencies of the internal sound pressure for given driving frequency ν and coupling coefficient ξ obtained by numerical solution of the Eqs. (3.45)–(3.46). The marked domain corresponds to the solution of Eq. (3.62)

The behavior illustrated above is shown in Fig. 3.17. The dots represent steady-state frequencies of q from the numerical solution of Eqs. (3.45)–(3.46) for the driving frequency ν, the feedback coupling ξ and $\mathrm{Ma} = 0.05$. The red marked domain corresponds to the complex-valued eigenfrequencies according to the relation (3.62). It is clearly demonstrated that when the eigenfrequencies are complex, the solution is mode-locked.

3.2.4 Numerical examples and model parameters

Numerical solution to the whole set of equations (3.43)–(3.44) is required in order to get closer to the experimental practice. The equations were solved employing the Python library SciPy [114]. Specifically, the adaptive fourth-order Runge-Kutta scheme ("rk45") was utilized.

The frequency of whistling grows with the velocity of the free-stream flow, so presumably (according to the Strouhal law) the phenomenological driving frequency increase as well (as in Eq. (3.24)). Two simulations presented below rely on such gradual variation of the driving frequency ν due to the changing flow speed U. Generally, because the scaling in Eqs. (3.41) depends on U, the time dependency $U(\tau)$ shall bring some new terms to the governing equations (3.43)–(3.44). Such terms are small enough to neglect them if the flow velocity U varies slowly

$$\left|\frac{1}{U^2}\right| \gg \left|\frac{1}{U^3}\frac{\mathrm{d}U}{\mathrm{d}\tau}\right| . \tag{3.63}$$

and the simulations are set accordingly.

Comparison with the experimental data is necessary to validate the model and find the fitting parameters. The experiments of Rudenko [87] were used for the validation. They were measured on a 350 mm long pipe, with 60 mm inlet and outlet tube smooth. The total of 53 corrugations spans over 230 mm of the corrugated section. The difference between the effective speed of sound c in the corrugated section and c_0 in the smooth part is less than 2% and is disregarded in the calculations (only the effective value c is employed).

The fitting parameters A, Sr, ξ shall be found from experimental data. As we cannot evaluate any derivatives in the fitting parameter space, some of the gradient-free optimization methods must be employed (sometimes refered to as "the zeroth order methods"). The genetic optimization was chosen as a well-tried option (see e.g., [115]).

Individuals were determined by three genes: the values of A, Sr and ξ. The fitness function was defined as the difference between the whisting frequency for given flow speed in experiment and the corresponding one one obtained from the numerical evaluation of the model equations (thus forming a single objective problem). The individuals chosen for breeding the next generation were picked based on the stochastic universal sampling [116].

The obtained parameter values are $A = 0.005$, $\mathrm{Sr} = 0.25$, $\xi = 0.0023$. The results of the simulated velocity sweep are depicted in Fig. 3.18 (the Fourier-transformed data from the numerical simulations in the form of a spectrogram are given). The phenomenon of mode-locking is clearly observable at the pipe resonances. Such behavior is well-known from many experimental works (see e.g., [52, 82, 84, 85]). Hence, its appearance supports the model validity.

In order to get a broader perspective, the experimenta data of Lim and Razi [89] were employed for comparison with our model as well. Results with the tube lengths of 0.45 m and 0.55 m and the number of corrugations 54 and 76 are plotted in Fig. 3.19. The characteristic length $\Lambda = 0.003$ m was the same for both cases. The fitting parameters were found from the experimental data employing genetic optimization. The nonlinearity parameter $A = 0.005$ was the same in both set-ups. The coupling parameters ξ equal to 0.0012 and 0.0009, as well as the Strouhal numbers Sr 0.37 and 0.35, were found for the shorter and the longer tube respectively.

The second numerical experiment consists of subjecting the studied system to a gaussian shaped velocity pulse (see Fig. 3.20). The geometry variables and fitting parameters were taken from the first case above (based on experiments by Rudenko [87], the velocity sweep in Fig. 3.18). The most striking here is the asymmetry caused by hysteresis, which has been reported to be one of the typical features of the corrugated pipes sound generation [52, 82, 83]. The system remains in the achieved state longer that it would correspond to the simple linear relations to the input parameters. Although there are experimental data showing the effects of hysteresis in whistling of corrugated pipes (e.g. [117]), we are adding this pure numerical, yet uncomplicated example for the sake of simplicity in order to show that the proposed model is capable of containing this phenomenon as well.

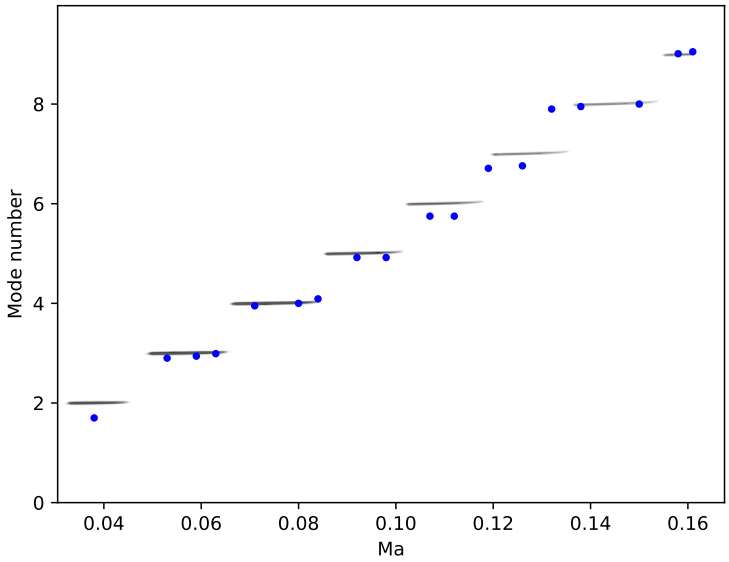

Figure 3.18: Spectrogram of the (scaled) acoustic velocity at the corrugated pipe's open end during a linear mean flow velocity sweep. The color scale is linear and therefore arbitrarily scalable by B. The circles mark the experimental values as read from [87] and subsequently scaled.

To complete the numerical treatment, some practical recommendations are given regarding the fitting the model to the experimental data. A good match can be found within a few generations of the genetic oprimization when the initial estimations of A, ξ, and Sr are well-chosen. It is straightforward to assess the initial Strouhal number from experimental data. The nonlinearity parameter A is approximately $\sim 10^{-3}$ and the solution is not very sensitive to its value. Often, it is sufficient to pass $A = 0.005$ as a constant and leave it out of the optimization process. On the contrary, the coupling parameter ξ alters the solution significantly. Its value decreases with the number of corrugations and generally $\xi \ll 1$ for most practical cases.

Finding the scaling parameter B from the sound amplitude is straightforward (see Eq. 3.41). Obtaining its value from experiments is not the optimization in the true sense of the word. However, it is worth to note, that the proposed model gives the estimation of the internal pressure field. Often, the experimental data are rather available for the radiated pressure and details of the radiation process (such as terminating impedance, flanged vs. unflanged opening etc.) must be taken into account. Based on the internal field measurements of Rudenko et al. [87], the value $B \sim 10^{-4}$ is obtained.

To conclude this section, note, that there are some discrepancies regarding the losses. First, Ingard and Singhal [110] considered a slighthly dissimilar experimental set-up when deriving their eigenfrequencies formula. Second, the role of turbulent losses might be of more importance. Hence, the coefficient of

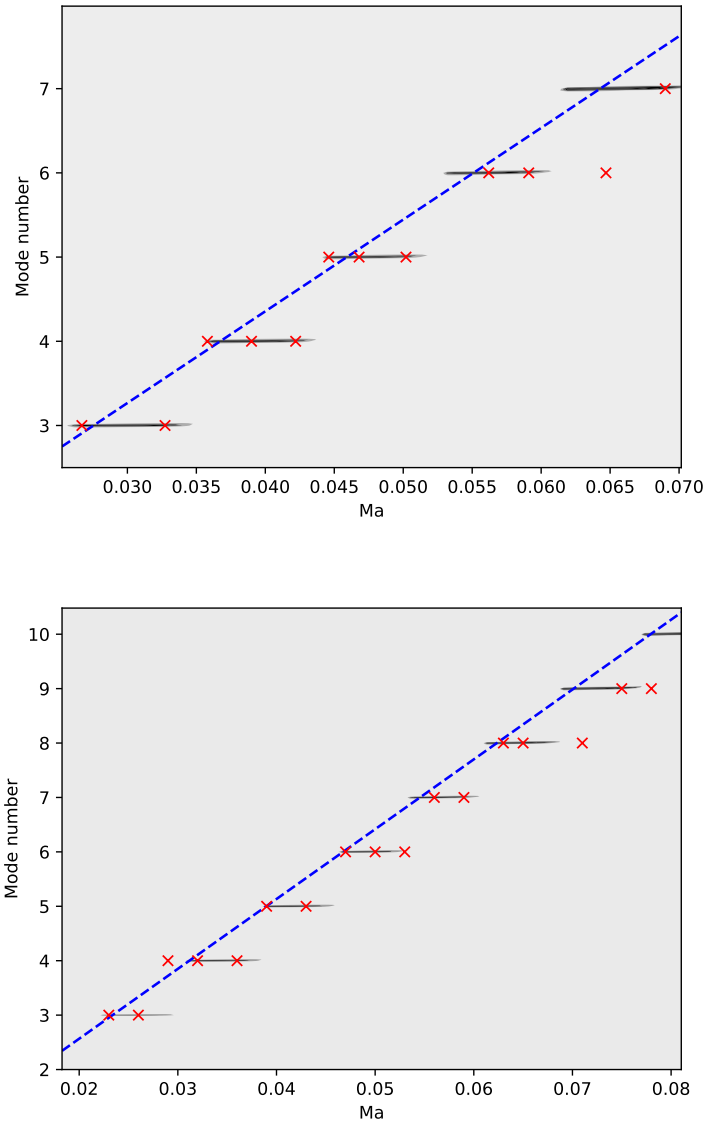

Figure 3.19: Spectrogram of the (scaled) acoustic velocity at the corrugated pipe's open end during a linear mean flow velocity sweep. The color scale is linear and therefore arbitrarily scalable by B. The crosses mark the experimental values as read from [89] and subsequently scaled. Top: tube length 0.45 m with 54 corrugations. Bottom: tube length 0.55 m with 76 corrugations.

the imaginary part in Eq. (3.37) might be different. In order to test that, it was allowed that the losses might be ad hoc multiplied by a constant during the optimization process. The obtained results always exhibit this constant ≈ 1, so the model of the losses appears to be correct.

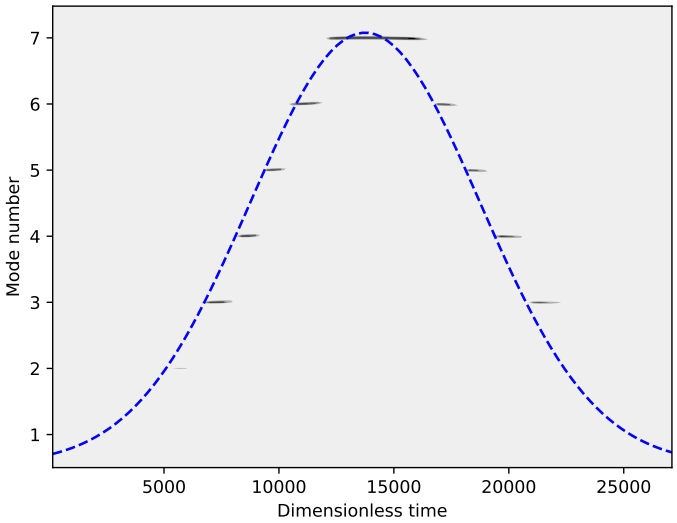

Figure 3.20: Spectrogram of the scaled acoustic velocity at the corrugated pipe's open end when subjected to a gaussian shaped velocity pulse. The color scale is linear and therefore arbitrarily scalable by B. The dashed line shows the instantaneous driving frequency ν.

3.2.5 Finite-amplitude weakly-nonlinear formulation

It follows from the experimental data (see e.g., [87]) that the acoustic quantities inside the corrugated pipes may reach amplitudes for which the weak finite-amplitude nonlinear formulation would be in place. As a supplement to the previous sections an example of such treatment is incorporated here as described in [118]. The framework from the cited article is meant to serve as a phenomenological model of the self-sustained sources in the 1D resonator with finite-amplitude waves in general. Therefore, the notation and some details are not identical to the small-signal case above. However, the correspondence is self-evident. The main difference is employing the velocity potential as the acoustic variable.

The effect of finite amplitudes to the sound propagations might be captured by various formulations of the wave equations (see e.g., [119]). Here, the one-dimensional Kuznetsov equation is employed, because it retains the d'Alebertian form of the operator (on the left-hand-side) and therefore the differences with regard to the previous infinitesimal amplitude case are clearly demonstrated:

$$c_0^2 \frac{\partial^2 \varphi'}{\partial x^2} - \frac{\partial^2 \varphi'}{\partial t^2} = \frac{\partial}{\partial t}\left(\frac{\partial \varphi'}{\partial x}\right)^2 + (\gamma - 1)\frac{\partial \varphi'}{\partial t}\frac{\partial^2 \varphi}{\partial x^2} - \zeta \frac{\partial^3 \varphi'}{\partial x^2 \partial t}\,, \tag{3.64}$$

where φ' are the perturbations of the velocity potential and ζ is the sound diffusivity coefficient. The equation is missing an integro-differential term

responsible for the thermoviscous losses in the acoustic boundary layer. However, considering the quasi-plane wave propagation, it can be ommitted and the diffusivity ζ shall be increased instead (see e.g., [120]).

Considering the velocity potential formulation a source term corresponding to the (volume density of) force distribution f which might be supplemented to Eq. (3.64) should take the form:

$$\int \frac{\partial f}{\partial t} \mathrm{d}x \ . \tag{3.65}$$

As above, we assume that the source is represented by an array of point-like sources and therefore:

$$f(x,t) = \sum_m g_m(t) \delta\left(x - x_m\right) \ . \tag{3.66}$$

where x_m is the location of the m-th source and $\delta(x)$ denotes the Dirac function and $g_m(t)$ is the instantaneous value of the m-th oscillating force term. The last expression (3.66) may be integrated according to (3.65) and substituted to (3.64) to obtain the the first of the model equations:

$$\begin{aligned} c_0^2 \frac{\partial^2 \varphi}{\partial x^2} - \frac{\partial^2 \varphi}{\partial t^2} = \\ \frac{\partial}{\partial t}\left(\frac{\partial \varphi}{\partial x}\right)^2 + (\gamma - 1)\frac{\partial \varphi}{\partial t}\frac{\partial^2 \varphi}{\partial x^2} - \zeta \frac{\partial^3 \varphi}{\partial x^2 \partial t} - \sum_m \frac{\partial g_m}{\partial t} \mathrm{H}\left(x - x_m\right) \ . \end{aligned} \tag{3.67}$$

where H denotes the Heaviside step function.

The acoustic velocity u' and the pressure p' are calculated from the velocity potential as

$$u' = \frac{\partial \varphi}{\partial x} \ , \tag{3.68}$$

$$p' = -\rho_0 \frac{\partial \varphi}{\partial t} + \frac{\rho_0}{2c_0^2}\left(\frac{\partial \varphi}{\partial t}\right)^2 - \frac{\rho_0}{2c_0^2} \sum_m g_m \mathrm{H}\left(x - x_m\right) \ , \tag{3.69}$$

where ρ_0 is the ambient density and a small term due to dissipation was omitted in the pressure equation.

An analogue to Eq. (3.23) is proposed in the form:

$$\ddot{g}_m + A\omega(\alpha^2 g_m^2 - 1)\dot{g}_m + \omega^2 g_m = \omega \eta \left.\frac{\partial \varphi}{\partial x}\right|_{x = x_m} \ , \tag{3.70}$$

where the dot denotes the derivative with respect to t and A, ω, η denote a coefficient of nonlinearity, an eigenfrequency and the feedback coefficient respectively. The parameter α governs the limit cycle size.

Next we introduce dimensionless quantities

$$t = \frac{L}{\pi c_0}\tau\ , \qquad x = L\sigma\ , \qquad \varphi = \frac{Lc_0}{\pi}\Phi$$
$$g = \rho_0 c_0^2 G\ , \qquad p = \pi^2 \rho_0 c_0^2 P$$

and recast the governing equations as

$$\frac{1}{\pi^2}\frac{\partial^2\Phi}{\partial\sigma^2} - \frac{\partial^2\Phi}{\partial\tau^2} = \frac{\partial}{\partial\tau}\left(\frac{\partial\Phi}{\partial\sigma}\right)^2 + (\gamma-1)\frac{\partial\Phi}{\partial\tau}\frac{\partial^2\Phi}{\partial\sigma^2} - \\ - \zeta^*\frac{\partial^3\Phi}{\partial\sigma^2\partial\tau} + \frac{1}{\pi^2}\sum_m \frac{\partial G_m}{\partial\tau}\mathrm{H}(\sigma-\sigma_m)\ , \quad (3.71)$$

$$\ddot{G}_m + \varepsilon\nu(\beta^2 G_m^2 - 1)\dot{G}_m + \nu^2 G_m = \nu\eta^*\left.\frac{\partial\Phi}{\partial\sigma}\right|_{\sigma=\sigma_m}\ , \quad (3.72)$$

where $\nu = \omega L/\pi c_0$ is the normalized frequency, $\beta = \alpha\rho_0 c_0^2$ and η^*, ζ^* denote the modified feedback and attenuation coefficients respectively and the dot represents the time derivative with respect to τ now.

To show the principal new phenomena the following scenario was simulated. Five point sources were placed equidistantly in the waveguide. Their frequencies were slowly growing (a linear sweep), starting slightly below the 2nd resonance frequency and ranging towards the 3rd one. Remaining parameters were chosen as follows: $\vartheta^* = 0.05$, $\zeta^* = 5\cdot 10^{-4}$, $A = 0.005$, $B = 10^{-4}$. The open ends of the tube are considered ideal pressure release surfaces and therefore the boundary conditions $p'_{\text{open-end}} = 0$ are employed.

Solution to Eqs. (3.71)–(3.72) are found numerically. In space the finite difference discretization is introduced, which effectively transforms the system into a large set of ordinary differential equations in time. The 4th order central finite difference scheme in space is introduced. The boundary conditions are taken into account by the ghost points (see e.g., [121]). The time domain equations are solved by the adaptive scheme using the Python library SciPy [114] (`scipy.integrate.odeint` based on FORTRAN `odepack` [122]).

Results of the numerical evaluation of Eqs. (3.71)–(3.72) are depicted in Fig. 3.21. Again, the nonlinear synchronization (mode-locking) occurs near the resonance frequency although not matching it perfectly.

In the mode-locked states a strong sound field due to the resonance is observed. The number of harmonics grows (the so-called wave steepening – see e.g., [53]) but the clear shockwaves are not formed because of the above mentioned detuning. As the driving moves further out of resonance the higher harmonics vanish. When the driving frequency gets close enough to the next resonance a sudden shift of the sounding frequency takes place.

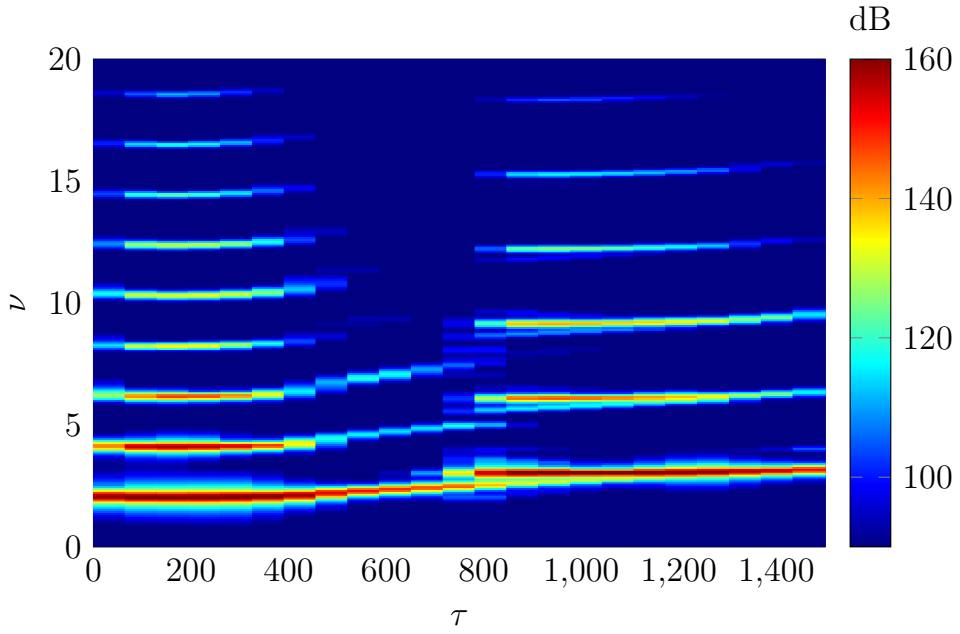

Figure 3.21: Spectrogram of the velocity (and therefore the driving frequency) sweep. Note the non-smooth change of the fundamental frequency due to mode-locking and the generation of higher harmonics when the system is close to resonance.

A weakspot of the combination Kuznetsov equation – van der Pol equation is the odd harmonic spectrum of the van der Pol oscillator. It is possible that the textbook case of successive harmonics build-up towards the shock formation is disrupted due to this feature.

Chapter 4

Heat exchangers as the sonic crystals

Heat exchangers are employed in a wide range of systems (computers, cars, power plants, air conditioners, ventilation systems etc.). In order to ease the thermal energy exchange by advective cooling, the heat exchangers are often used in combinations with fans. Hence, the problem of sound transmission through the periodic structure with flow arises. The generation of noise due to the unsteady flow through the coolant tube array might play a role as well.

In practical applications, the fans are the predominant sources of the sound. Their spectrum (see e.g., Fig. 4.1) consists of low-frequency tone-like components corresponding to the blade passing frequency and its harmonics along with the broadband contributions due to turbulence. The relative importance of the broadband noise is increased when the rotating machinery ingests an already disrupted flow [123] – such as the one taking place downstream of the heat exchanger (see Fig. 4.2). As depicted, the coolant tubes are often set to a staggered arrangement in order to provide the maximum flux around the tubes. Such structure is referred to as the hexagonal lattice in terms of sonic crystals. For the sake of unambiguity, note, that no other arrangement is studied below. Only the flow-acoustic interactions are considered in the following (there is no heat flux from the coolant tubes).

The section is organized as follows. First, the interactions of incoming acoustic waves with the periodic structure are estimated from dispersion diagrams (Sec. 4.1.1) and subsequently verified by the experimental data (Sec. 4.1.2). To conclude this subpart, an extension of the heat exchanger with the locally resonant structures is given as a case intended for future research (Sec. 4.1.3). Second, the sound generation from an unsteady flow past the heat exchanger tubes is dealt with by means of numerical simulations (Sec. 4.2.2). Dependence of the radiated intensity on the varying flow speed is given in Sec. 4.2.3.

4.1 Effects of the coolant tubes periodicity

The main goal of this section is to provide evidence that the heat exchanger (without flow) presents a valid example of a sonic crystal. The effects of flow

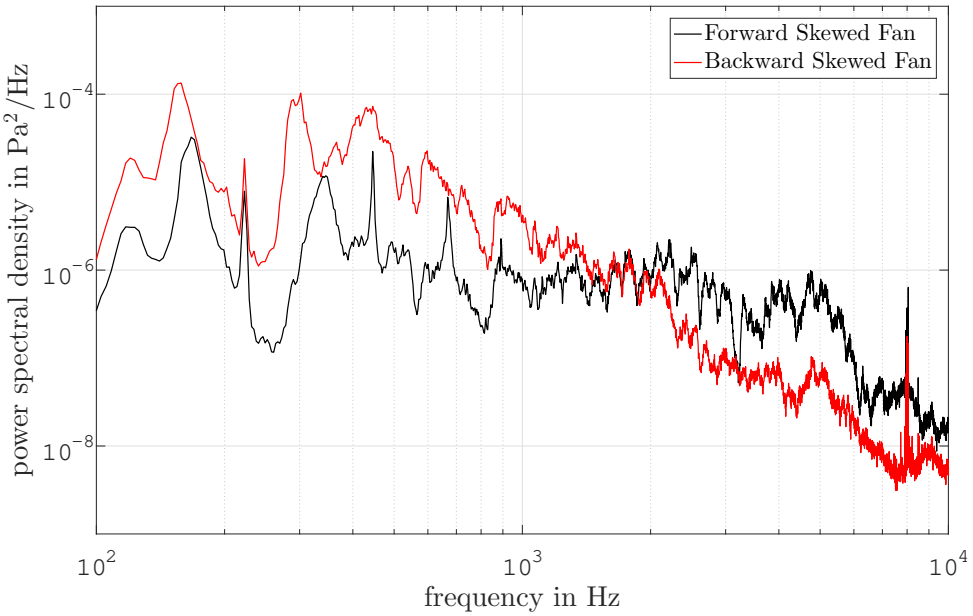

Figure 4.1: Two examples of axial fan spectra (from [124]). Aerodynamical details of the fan blades skew (see e.g., [125]) are not important here.

are discussed in Sec. 4.2.2 below.

Let us begin with the basic description of the hexagonal lattice as it is usually given in the field of acoustics of periodic structures (see e.g., [3, 21, 22, 23]). Tubes of the heat exchanger form a hexagonal (triangular) lattice with primitive vectors $\boldsymbol{a}_1$, $\boldsymbol{a}_2$. The reciprocal lattice has the hexagonal structure as well (only rotated by $\pi/6$) with primitive vectors given by [3]:

$$\boldsymbol{b}_i = 2\pi\varepsilon_{ijk}\frac{\boldsymbol{a}_j \times \boldsymbol{a}_k}{\boldsymbol{a_1} \cdot (\boldsymbol{a}_2 \times \boldsymbol{a}_3)} \,, \tag{4.1}$$

where ε_{ijk} is the Levi-Civita symbol. In 2D, the remaining vector is treated just as a unit vector perpendicular to both $\boldsymbol{a}_1$ and $\boldsymbol{a}_2$.

Wigner-Seitz cell is a primitive cell obtained by Voronoi tesselation (see e.g., [3]). When this construction is conducted in the reciprocal space, it results in the so-called (first) Brillouin zone. Owing to the symmetries, the first Brillouin zone can be further reduced to the irreducible Brillouin zone.

For simple crystal lattices (free of defects, locally resonant elements etc.) a rough estimation of the frequencies that are likely to be prevented from propagation can be made based on Bragg's diffraction law (see e.g., [3]). The condition of the maximal constructive interference between a plane wave impinging on the crystal and the one reflected from the successive crystal planes reads

$$n\lambda = 2d\sin\theta \,, \quad n \in \mathbb{N} \,, \tag{4.2}$$

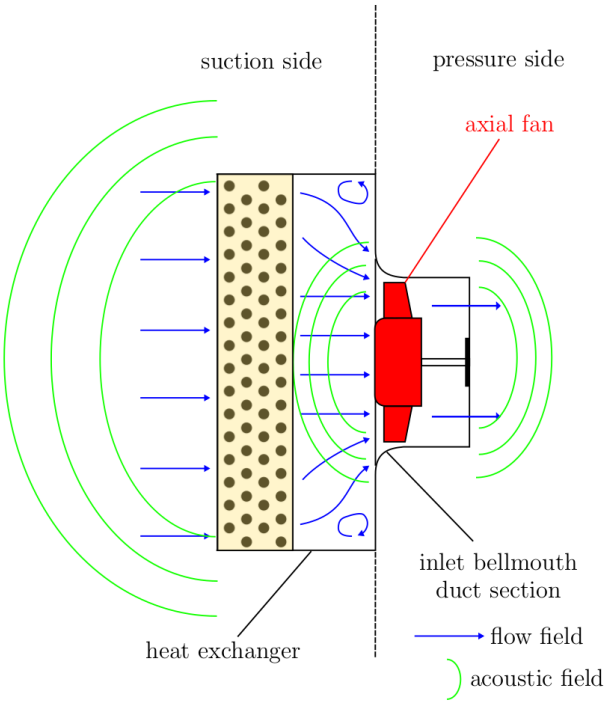

Figure 4.2: Schematic sketch of the heat exchanger arrangement with axial fan (from [124]).

where λ, d and θ denote wavelength of an impinging monofrequency plane wave, distance between crystallographic planes and angle measured between the wave propagation direction and the crystallographic plane, respectively, see Fig. 4.4. For normal incidence ($\theta \to \pi/2$) we obtain the first ($n = 1$) Bragg frequency f_B:

$$f_B = \frac{c_0}{\sqrt{3}a} , \tag{4.3}$$

where a is the lattice constant, c_0 the adiabatic speed of sound and $d = \sqrt{3}a/2$ for a hexagonal lattice.

An essential parameter of a sonic crystal lattice, its filling factor ff, is defined as the ratio of the insertion area to a whole unit cell area. Hence, for hexagonal lattice with lattice constant a and tube radius r:

$$ff = \frac{2\pi r^2}{\sqrt{3}a^2} . \tag{4.4}$$

4.1.1 Dispersion diagrams and bandgaps

A more detailed prediction of the bandgap structure is obtained from a dispersion diagram. Traditionally, the dispersion diagrams are obtained employing

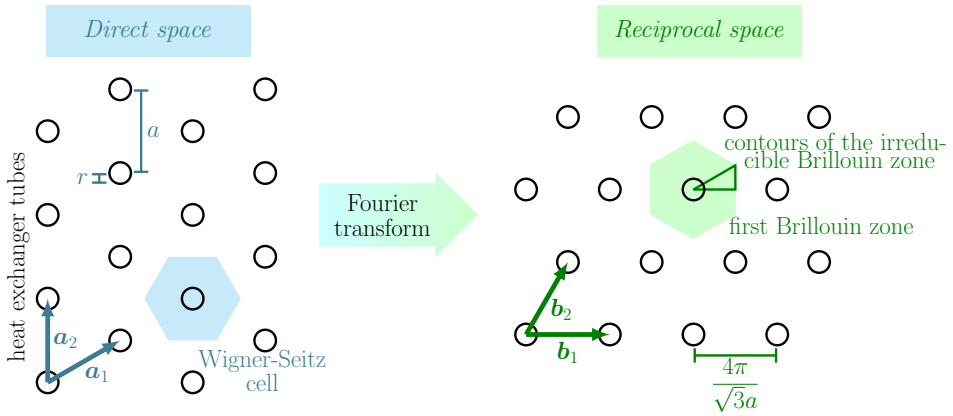

Figure 4.3: Illustration of direct and reciprocal lattices.The cooling tubes of a heat exchanger are indicated as black circles. The cooling tubes form a hexagonal lattice due to their staggered arrangement.

the plane wave expansion method (PWE) or its extensions. However, there are some doubts about its application in the fluid-solid sonic crystals due to convergence of the truncated Fourier series for high impedance contrast between the materials and the occurence of fictitious modes arising for the same reason (see [23, 22]). Hence, we retain the theoretical foundations, but the bandgap structure calculation is carried out with the finite element method (in Comsol Multiphysics 5.5).

By the Floquet-Bloch theory, the solution of the wave propagation phenomenon inside the (infinite) crystal lattice can be constructed from the basis of eigenfunctions obtained by solving the eigenvalue problem within the primitive cell with periodic boundary conditions (see Fig. 4.5 and refs. [3, 22, 23]):

$$\hat{p}(\boldsymbol{r}_0) = \hat{p}(\boldsymbol{r}_0 + \boldsymbol{r}_1)e^{-\mathrm{i}\boldsymbol{k}\cdot\boldsymbol{r}_1} \ . \tag{4.5}$$

where $\boldsymbol{k}$ is the (Bloch) wave vector and $\boldsymbol{r}_1$ the distance between respective boundaries. The time-harmonic behavior of the governing quantities is assumed with $e^{\mathrm{i}\omega t}$ sign convention, where ω is the angular frequency and $i = \sqrt{-1}$.

Due to symmetry, the irreducible Brillouin zone contains the only unique (Bloch) wave vectors and just the wave vectors pointing from the zone center to the contours of the irreducible Brillouin zone shall be investigated.

Frequency (in Hz) of a propagating mode is calculated from the angular eigenfrequencies obtained as the eigenvalues for a given Bloch wave vector $\boldsymbol{k}$. The resulting dispersion diagram (see e.g., Fig. 4.6) shows, that for some frequency bands there are no propagating modes. These are called complete bandgaps if they span over the whole irreducible Brillouin zone, or pseudo-bandgaps if they prevent the propagation in only one direction. The wave vectors are described employing the high-symmetry points of the reciprocal lattice (see the insets in the respective figures and see e.g., [22, 23]).

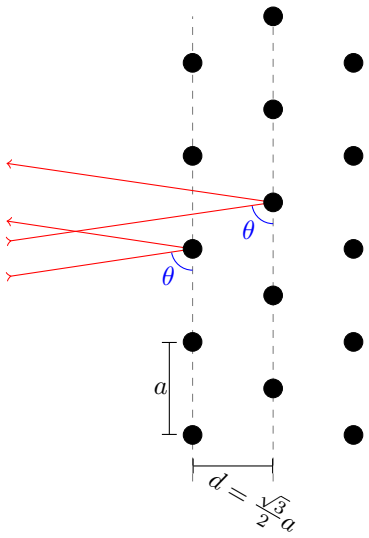

Figure 4.4: Schematic diagram of Bragg diffraction in a hexagonal lattice.

The dispersion relations $\omega = \omega(\boldsymbol{k})$ are acquired numerically, the hexagonal vicinity of a single cooling tube being the unit cell. For now, the air is assumed quiescent, inviscid and thermally nonconducting. Therefore, the Helmholtz equation is solved inside the unit cell:

$$\nabla^2 \hat{p} + k^2 \hat{p} = 0 \tag{4.6}$$

and the Neumann boundary condition for acoustic pressure is prescribed on the surface of the tubes ($\partial\hat{p}/\partial\boldsymbol{n} = 0$, with $\boldsymbol{n}$ denoting the surface's outer unit normal). The hats are dropped henceforth for simplicity. The simulations were conducted in Comsol Multiphysics 5.5 (Pressure Acoustics Interface, Frequency Domain) with the mesh parameters set for 12 elements per the shortest investigated wavelength (corresponding to 20 kHz).

Results of the two-dimensional calculations (assuming no variations of acoustic pressure along the coolant tubes) are given in Fig. 4.6 for two specific geometries: $a = 40$ mm with $r = 6$ mm, ($ff \approx 8\%$) and $a = 25$ mm with $r = 4.76$ mm, ($ff \approx 13\%$). These configurations are chosen for the posssibility of comparison with experimental data given below. They correspond to commercialy available heat exchangers.

First, notice that the rough approximation of the characteristic frequency of the bandgap by Bragg's law is valid. However, the filling factor is too low for the complete bandgap to open around the first Bragg frequency. Therefore, only a pseudo-bandgap in the Γ–M direction occurs and there is only a very narrow complete bandgap around 9 kHz and 15 kHz respectively. It is clear that the configuration with a higher filling factor exhibits wider bandgaps.

Naturally, the real device is three-dimensional and moreover, it is equipped with thin cooling fins extended across the coolant tubes with 2.2 mm spacing

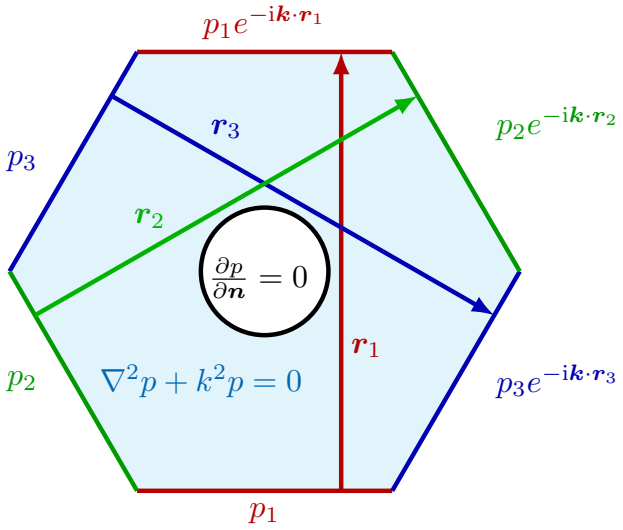

Figure 4.5: Periodic boundary conditions in a hexagonal unit cell.

for each geometry (see Fig. 4.8). For the sake of completeness, one shall investigate the three-dimensional unit cell in the shape of a hexagonal prism (which again results in the same shape of the Brillouin zone but scaled and rotated, see Fig. 4.7c).

As expected, the third dimension does not alter the composition of bandgaps (in the frequency region of interest), because the cut-off frequency of the transversal ("fin-to-fin") modes is slightly above 70 kHz. One sees from the dispersion diagram in Fig. 4.7a that the group velocity along the coolant tubes is zero.

On the other hand, the fins present closely spaced surfaces on which the thermoviscous losses take place. In order to capture this effect, another three-dimensional simulation over the wavevectors along Γ – M – K – Γ was conducted. Now, with the complete set of linearized Navier-Stokes equations (without flow) and the no-slip isothermal boundary conditions on the surface of the fins and the coolant tube. The same treatment of boundary layer mesh as given in Sec. 3.1.3 was employed.

The eigenfrequencies obtained in this setup are complex (the real and imaginary parts depicted in Fig. 4.7a and b, respectively). Comparison with the two-dimensional simulation without losses exhibits barely observable deviations of the real parts. Therefore, the bandgap structure is almost unaffected by the presence of the fins. This is not surprising, because the fin spacing (2.2 mm) is still much wider than the thermoviscous penetration depth (ca. 0.03 mm at 5 kHz, see Eq. (3.17) above).

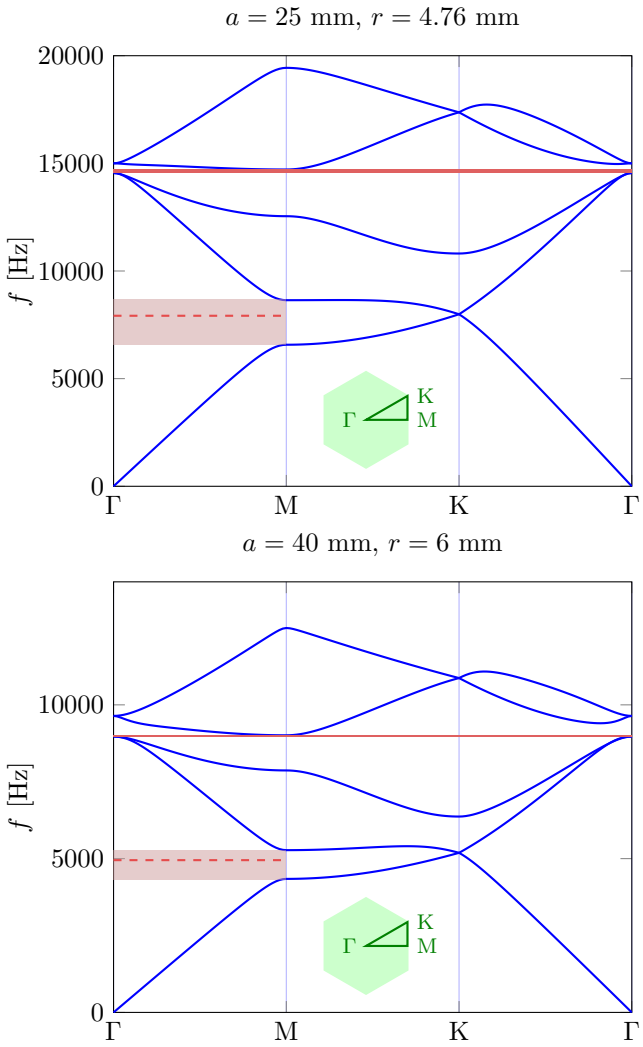

Figure 4.6: Dispersion diagrams for the hexagonal lattices with lattice constants 40 mm and 25 mm with tube radii 4.76 mm and 6 mm on the top and bottom respectively. Bragg frequency is marked by the red dashed line. The red fields show the pseudogap in the Γ – M direction and the narrow complete bandgap.

4.1.2 Comparison with experimental data

The results of the previous section were obtained with assumption of the periodic medium with infinite extent – this is embodied in the application of the periodic boundary conditions. Therefore, it is necessary to verify that these results are applicable in the real-world case of a heat exchanger consisting of four rows of coolant tubes.

The experiment is described in detail in [124]. In order to control the input signal, the axial fan was replaced by the loudspeaker and various signals were employed to assure that the experimental results are independent of the specific excitation (two fan noises, the log-sine chirp and the white noise were

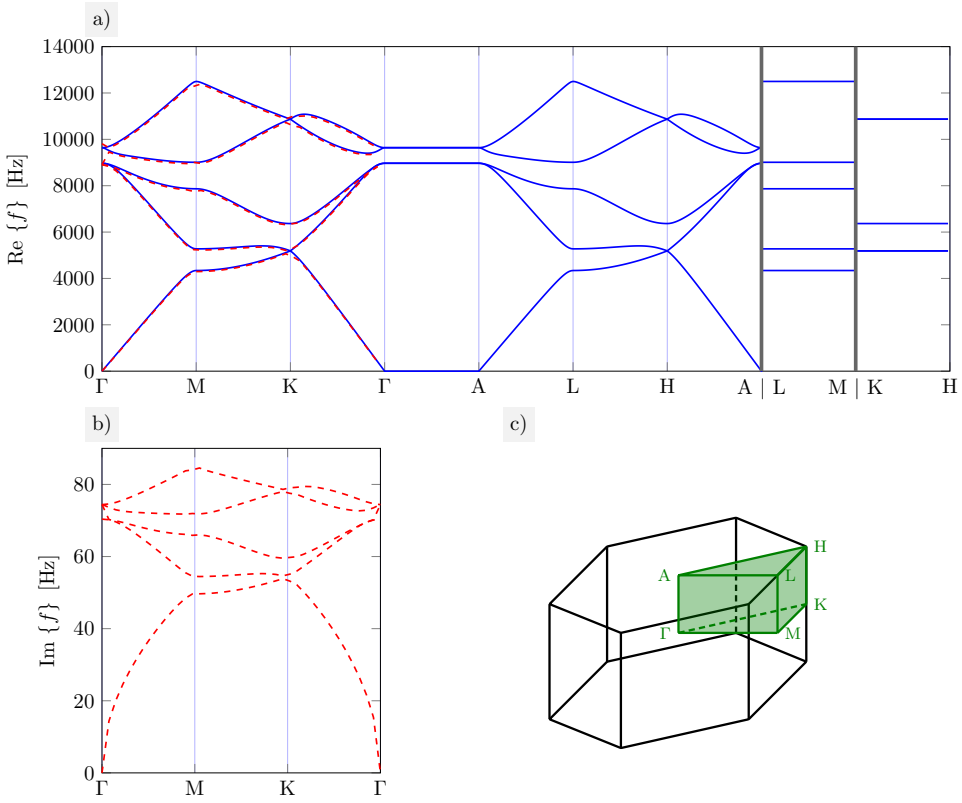

Figure 4.7: Dispersion diagrams (a,b), the Brillouin zone (c) and the irredcible Brillouin zone (green volume in c) for the three-dimensional case taking the presence of cooling fins into account. The lattice constant $a = 40$ mm and the tube radii $r = 6$ mm. The blue curves are obtained from the simulations without losses and the red ones from the solution of the linearized Navier-Stokes equations. From [124].

employed). The key measured quantity was the insertion loss: the difference between the sound powers obtained for the same excitation with empty heat exchanger housing and the housing with coolant tubes and fins. The length of the coolant tubes inside the heat exchanger housing is 0.8 m. The housing profile is a square 0.8 m $\times$ 0.8 m.

The numerical simulations were conducted again but now for the 2D slice of the experimental setup (see Fig. 4.9). As it was commented above, the two-dimensional, inviscid and thermally non-conducting approach shall suffice. Hence, the Helmholtz equation was employed. A plane wave entering the system was prescribed and the perfectly matched layers (PMLs) were employed to mimic the anechoic room, in which the real experiment took place [124]. The walls of the housing as well as the walls of the inlet were considered perfectly rigid. The mesh had 12 second-order elements per the shortest investigated wavelength. The transmitted sound power was calculated from the intensity evaluated at the semi-circle surrounding the heat exchanger (see Fig. 4.9). Due to demanding requirements on the computational mesh density, the simulations are restricted by the upper limit of 10 kHz.

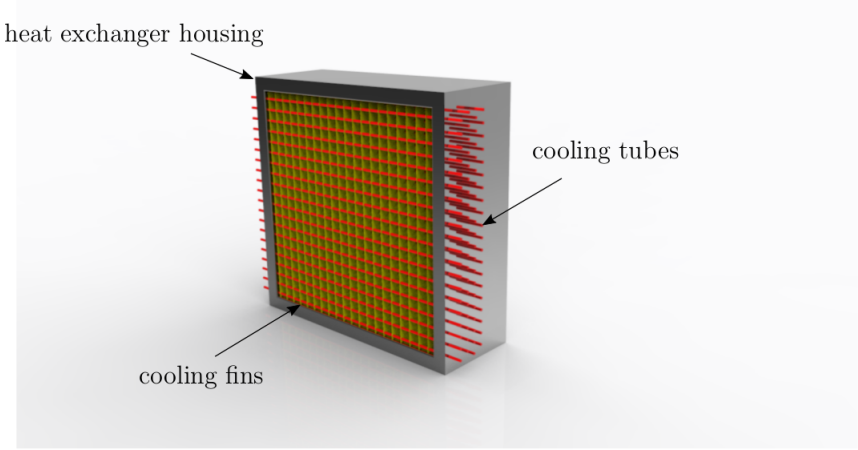

Figure 4.8: Sketch of the heat exchanger housing with coolant tubes and cooling fins (from [124]).

Comparison of numerical and experimental results is given in Fig. 4.10. The bandgaps calculated in the preceding section are marked by colored areas. Clearly, the experimental results match well with the simulations of the 2D slice of the experimental setup. The deviations are attributable to the neglected viscosity and thermal conductivity. They are ~ 1 dB almost everywhere, so their effect is merely small. There is seeming amplification of the transmitted sound at ca. 400 Hz for both geometries. This is due to the resonance of the heat exchanger housing [124]. When the housing is filled with coolant tubes (and structurally reinforced by them), the resonance is slightly modified, which shifts the reference transmission of the housing and results in the amplification – naturally only a seeming one.

But first of all, the predicted bandgaps are well-observable on the experimental data as well. This finding is of great practical importance because it opens a way towards a computationally advantageous approach applicable in the heat exchanger design. For illustration, note, that the calculations of the 2D dispersion diagrams as given above is approximately 50times faster than the simulation of the 2D slice of the experiment.

4.1.3 Locally resonant structures

In the preceding section a computationally feasible framework for the acoustic design of the heat exchanger arrangement was introduced: knowing the characteristic frequency to be blocked one can estimate the lattice constant from the Bragg's law (Eq. (4.3)) and then tune the bandgap properties based on the 2D dispersion relations. Nevertheless, this approach yields impractical results when a low frequency shall be prevented from propagation – the basic scaling would return an unworkably vast heat exchanger. Therefore, it is not straightforward to block e.g. the blade passing frequency of the fan, which is

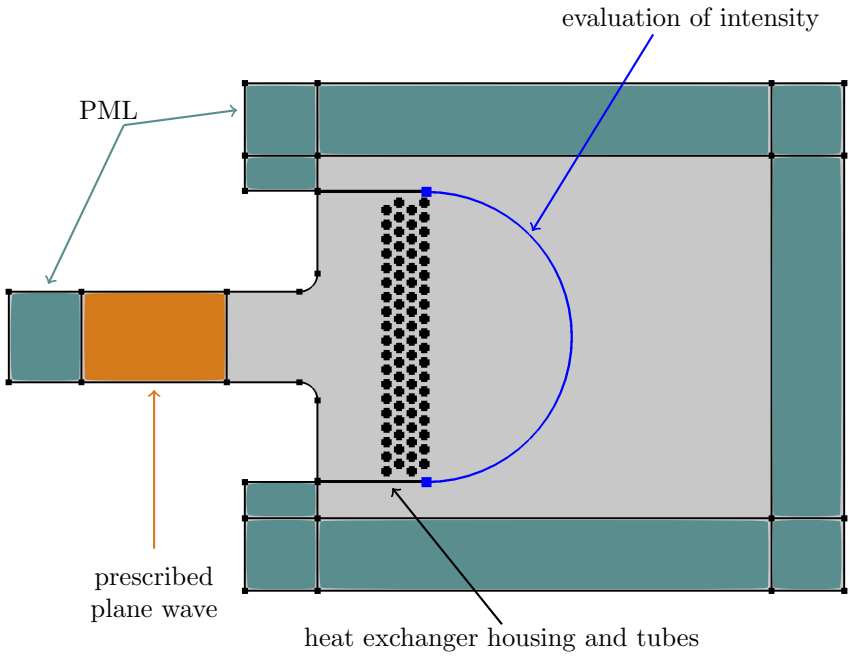

Figure 4.9: Computational setup of the simulation of the 2D experimental setup slice (from [124]).

usually well below 1 kHz for the heat exchangers from the experiment [124].

In order to reach the low frequencies, the locally resonant structures might be exploited, which benefit from coiling the space up to a "packed" resonator (see e.g., [126, 23]). A pilot example of such an approach for the heat exchangers is given now.

Another row is added to the heat exchanger (keeping the same lattice constant), yet now the scatterers are not the coolant tubes, but coiled metal sheets (see Fig. 4.11). The coiled-up structure acts as a quarter-wavelength resonator, which is capable of interacting with frequencies much lower than the Bragg frequency of the crystal.

To demonstrate the effect of adding the local resonances, the simulation of a 2D slice of the experiment was conducted with the presence of the coiled-up resonators. The computational setup was similar to the one given in Fig. 4.9. However, there were some alterations due to the geometry of the coils. As the spacing between the coiled sheets (2.4 mm) is quite narrow, the thermoviscous behavior might affect the local resonance. The thermoviscous penetration depth is ca. 0.1 mm at 500 Hz, so up to $\sim 10\%$ of the coiled waveguide cross section is occupied by the boundary layers. Hence, the linearized Navier-Stokes equations (with the resolved boundary layer mesh) were solved inside the resonators and coupled to the Helmholtz equation governing the rest of the domain.

Results of the computations are given in Fig. 4.12. Apart from the imprint

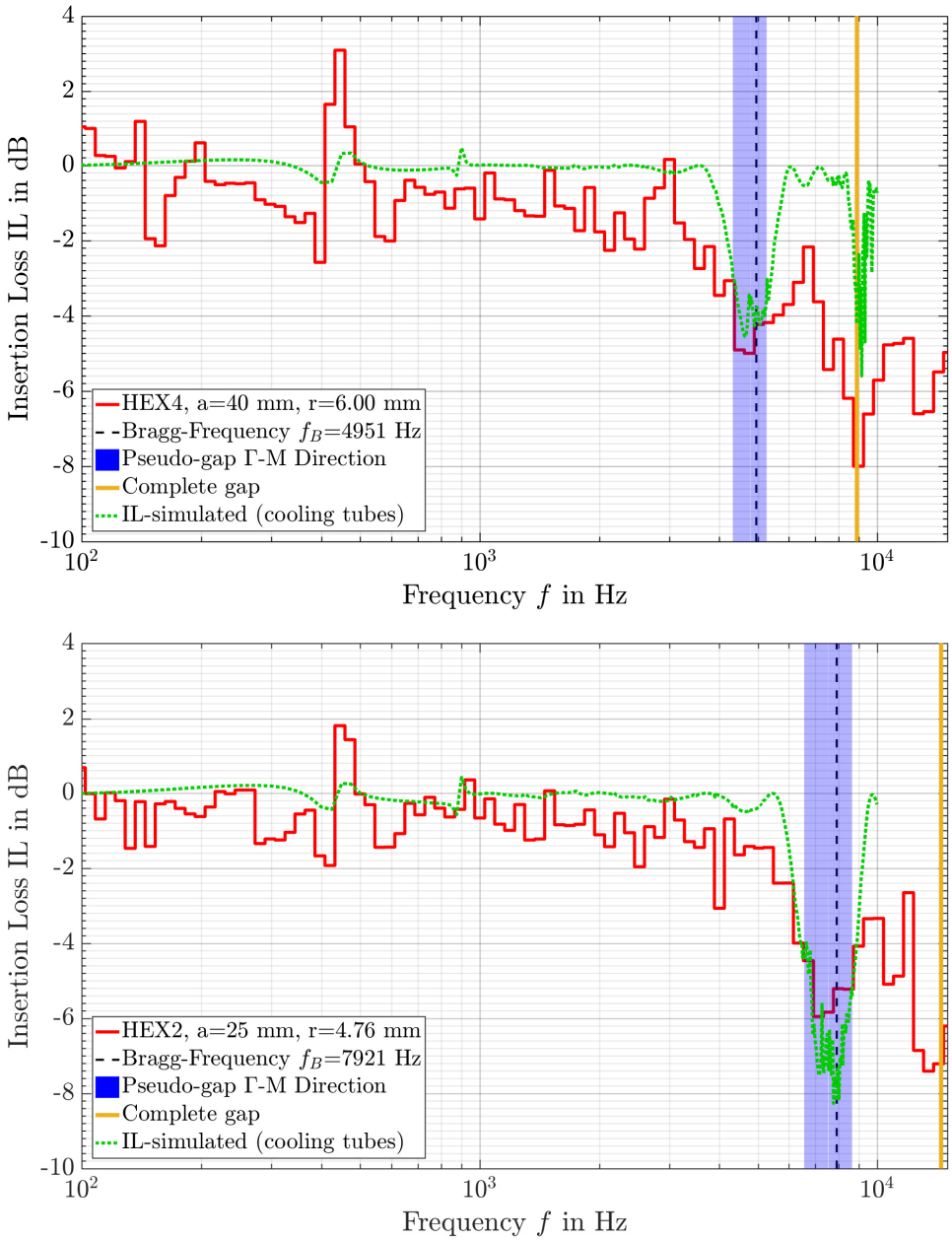

Figure 4.10: Comparison of the experimentally measured insertion loss (the red curve) with the numerical simulations (from [124]).

of the pseudo-bandgap in the Γ–M direction known from the previous sections, there are minima resembling a notch filter due to the resonances of the coils. Note that it is possible to tune and optimize the shape of the resonator so it reaches the blade passing frequency. This enables designing an optimized fan – exchanger couple emitting a significantly lower amount of noise.

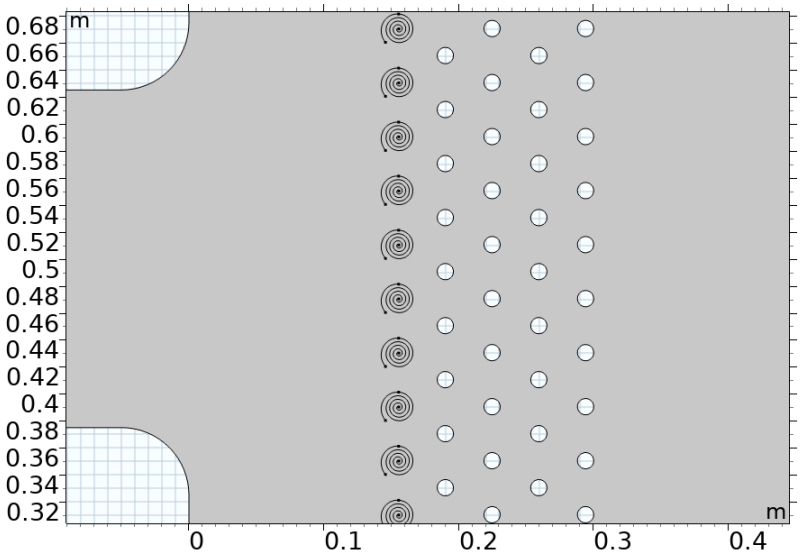

Figure 4.11: A detail from the geometry consisting of the heat exchanger investigated above (see Fig. 4.9) with added row of coiled up resonators.

4.2 Sound generation from unsteady flow through the heat exchanger

Until now the flow through the heat exchanger has been neglected. Due to similar reasoning, as it was given above for the transmission above the corrugated plate, it is not possible to linearize the hydrodynamic part of the governing equations. Consequently, there is no straightforward and indubitable way to incorporate the effect of the flow to the calculation of dispersion relations given above.

On the other hand, some useful insight might be obtained from the scaling considerations backed with the pilot numerical simulations. First, it is shown that the bandgap around the first Bragg frequency is very unlikely to overlap with the whistling frequency of the structure. Next, the sound radiation from the heat exchanger tube array is estimated in order to verify the applicability of previously known scaling.

4.2.1 Characteristic scales

Unsteady flow through the array of the heat exchanger tubes results in forming flow shapes that might be seen as the inception of the von Kármán vortex street, which however is never properly constituted due to the limited space (see Fig. 4.13). Nevertheless, the flow separation and occurrence of unsteady trailing wakes are evident. Assume that the vortex shedding (and therefore the peak whistling) frequency f_S is estimated by the Strouhal law

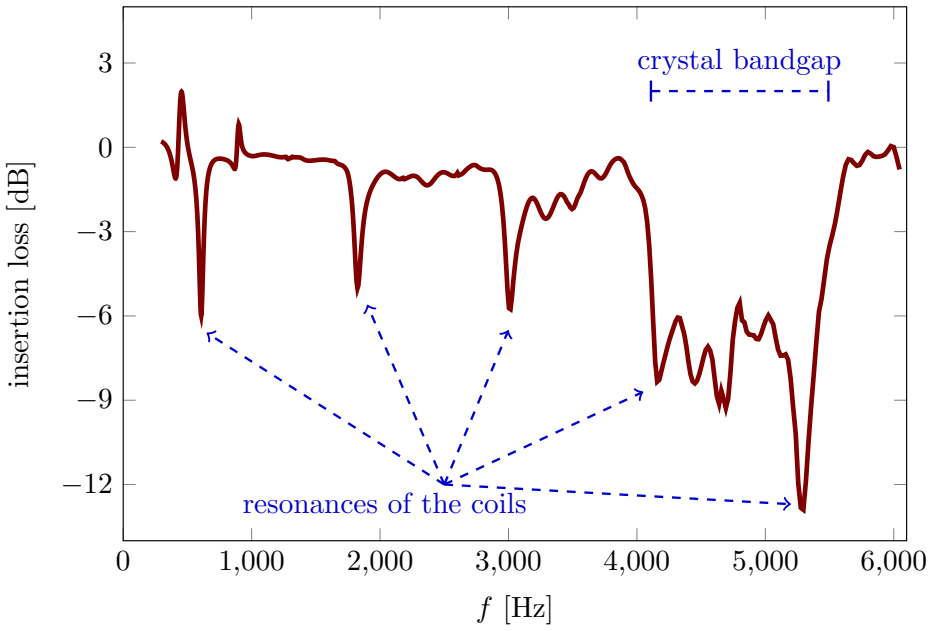

Figure 4.12: Insertion loss calculated for the coolant tube lattice ($a = 40$ mm, $r = 6.5$ mm) combined with the locally resonant coils (see Fig. 4.11).

$$f_S = \mathrm{Sr}\frac{U_0}{2r} , \tag{4.7}$$

where Sr, U_0 and $2r$ denote the Strouhal number, the characteristic velocity of the airflow far from the heat exchanger and the cooling tube diameter, respectively. The ratio of the Strouhal and Bragg (Eq. (4.3)) frequencies yields:

$$\frac{f_S}{f_B} = \frac{\sqrt{3}}{2}\mathrm{SrMa}\frac{a}{r} , \tag{4.8}$$

where $\mathrm{Ma} = U/c_0$ is the Mach number. Substituting from the definition of the filling factor ff for the hexagonal lattice (Eq. (4.4)) the following relation is obtained:

$$\frac{f_S}{f_B} = \sqrt[4]{\frac{3\pi^2}{4}}\frac{\mathrm{SrMa}}{\sqrt{ff}} . \tag{4.9}$$

By preliminary numerical experiments [118] it was found that an appropriate Strouhal number for the flow instabilities within the hexagonal lattice is ca. 0.2. Hence, the Strouhal and Bragg frequencies are separated by no less than one order of magnitude for low Mach number flows (two orders separation being presumably a more realistic typical case). It follows that the above-given reasoning considering the bandgap structure shall be relevant at least as a good approximation even for the case when a mild airflow through the heat exchanger takes place.

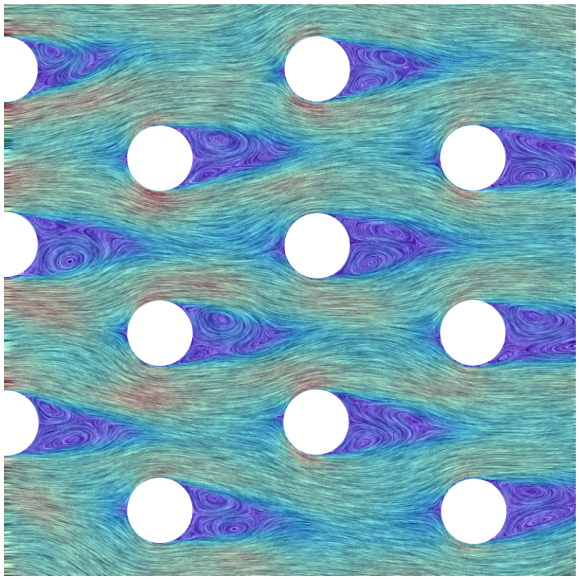

Figure 4.13: Qualitative example of the flow details past the heat exchanger cylinders.

It follows from the Strouhal law (Eq. (4.7)) that for low U_0 the radiated wavelengths will be much longer than the size of the whole heat exchanger tube array. We exploit this trait below for simplifying the numerical simulations: although the source domain is finite for the incompressible flow simulations, only a plane wave may propagate from it in the low frequency approximation (see e.g., [18, 127]) and the source region may be shrinked to a point for the considerations regarding the long wavelengths propagation.

There are many possible heat exchanger arrangements as well as their context (probably being only a part of a larger device). For definiteness, the same housing geometry with one of the previously introduced lattice arrangements is studied ($a = 40$ mm, $r = 6$ mm, 19 tubes in 4 rows). For simplicity and in order to avoid complicated discussion about specific reflections and wavefront spreading, it is assumed that the coolant tube array is placed within an infinite duct with the square cross section of the same dimensions as the housing (0.8 m $\times$ 0.8 m).

Only the two-dimensional simulations are conducted and it is assumed that their results are invariant along the coolant tube. Hence, for the purposes of calculating the values of the governing quantities on the faces of the tubes only the knowledge of 2D transversal slice is sufficient. This is an obvious simplification. It is reasonable as long as we can presume that the flow is synchronized along the tubes. Note that this is the case of the maximal sound radiation, so in other words, we are simulating the worst-case scenario, which is a valid engineering procedure.

4.2.2 Numerical simulations

It follows from Curle's analogy above (Sec. 2.5.2), that the reaction force to the unsteady hydrodynamical pressure presents the main source of the sound excitation for the low Mach number flow past rigid boundaries. Moreover, it follows from the preceding section that the whole heat exchanger is small compared to the characteristic wavelength radiated from the tube array. Hence, we simplify the treatment to the two-step simulations (as it is usual in the hybrid methods – see e.g., [26]).

First, the evolution of the unsteady flow through the tube array is simulated employing the URANS equations. Again, the $k-\omega$ SST turbulence model was employed with the same requirements on the computational mesh as given above (Sec. 3.1.3) The velocity was prescribed at the inlet, while zero (over-)pressure was imposed at the outlet of the computational domain.

From the URANS results the net unsteady force on a surface of the tube is obtained:

$$\boldsymbol{F}(t) = \oiint_S [p(\boldsymbol{y},t) - p_0(\boldsymbol{y})]\,\boldsymbol{n}\;\mathrm{d}S(\boldsymbol{y})\;, \tag{4.10}$$

where p, p_0, $\boldsymbol{n}$ denote the instantaneous hydrodynamic pressure, the (spatially non-constant) mean hydrodynamic pressure and the unit normal of the tube's surface, respectively. An equivalent point force is obtained by summation of the results of Eq. (4.10) for every coolant tube.

Only the component directed along the waveguide (say x) radiates to the far-field in the low frequency approximation. Subsequently, we obtain the inhomogeneous wave equation for the acoustic pressure perturbations far from the heat exchanger (see Eq. (2.39) above):

$$\frac{1}{c_0^2}\frac{\partial^2 p'}{\partial t^2} - \frac{\partial^2 p'}{\partial x^2} = -\frac{\partial f_x}{\partial x}\;, \tag{4.11}$$

where f_x is the x-component of the force density field, which can be expressed by the equivalent point force F_x located at $x=0$ as [18]:

$$f_x(x,t) = \frac{F_x(t)\delta(x)}{A}\;, \tag{4.12}$$

where A is the waveguide cross-sectional surface and δ denotes the Dirac function. The solution to the equation (4.11) is obtained employing the Green's function for the plane waves propagating from a point source inside a duct in the direction of positive x (see e.g., [18]):

$$G(x,\xi|t,\tau) = \frac{1}{2}c_0 \mathrm{H}\left(t-\tau-\frac{x-\xi}{c_0}\right)\;, \tag{4.13}$$

where H is the Heaviside step function.

Hence,

$$p'(x,t) = \int_{-\infty}^{t}\int_{-\infty}^{\infty} G(x,\xi|t,\tau)\frac{\partial}{\partial\xi}f_\xi(\xi,\tau)\ \mathrm{d}\xi\mathrm{d}\tau = \\ = \frac{c_0}{2A}\int_{-\infty}^{t}\int_{-\infty}^{\infty} \mathrm{H}\left(t-\tau-\frac{x-\xi}{c_0}\right)\frac{\partial}{\partial\xi}\left[F_\xi(\tau)\delta(\xi)\right]\ \mathrm{d}\xi\mathrm{d}\tau = \\ = \frac{F_x(t-\frac{x}{c_0})}{2A}\,. \quad (4.14)$$

The only requirement on the size of x is that it shall be big enough for the hydrodynamical instabilities past the tube array to cease. Then $p'(\boldsymbol{x},t)$ can be interpreted as the acoustic pressure.

The integration in Eq. (4.10) was conducted in Comsol and the subsequent uncomplicated data treatment in GNU Octave.

The sound radiation from a single cylinder in a free field resembles a dipole with the radiation lobes perpendicular to the U_0 direction (see e.g., [16, 18]) and the same behavior was confirmed for their array [128]. It follows that in a narrow waveguide a significant portion of the emitted sound does not propagate. As a direct consequence, the fundamental frequency is not dominating the spectrum in many cases presented below.

4.2.3 Effect of varying flow velocity

For the purposes of noise control, it is illustrative to evaluate the intensity I of propagating plane wave:

$$I = \frac{1}{T}\int_{T_0}^{T_0+T}\frac{p'^2(t)}{\rho_0 c_0}\ \mathrm{d}t\,, \quad (4.15)$$

where T_0, T denote time instant where the part of the investigated signal begins and T its length. The starting time T_0 was set to the beginning of the (quasi-)steady state of the radiated pressure signal and $T = 0.55$ s in the below-given cases.

In order to check the basic tendencies, seven values of U_0 were considered with the lattice parameters $a = 40$ mm, $r = 6$ mm. More precisely, the volume velocity $0.8 - 1.4$ m$^3 \cdot$ s^{-1} were considered for the channel of 0.8 m $\times$ 0.8 m. The values were chosen to correspond with the volume velocity reported for the practical appplication of the investigated heat exchanger arrangement [124].

As expected, the fundamental frequency grew with U_0 (from 29 Hz to 48 Hz), but the Strouhal number remained constant: Sr = 0.27. Note that even the wavelength connected to the 2nd harmonics of these fundamentals are still larger than the heat exchanger array, so the above-stated assumption

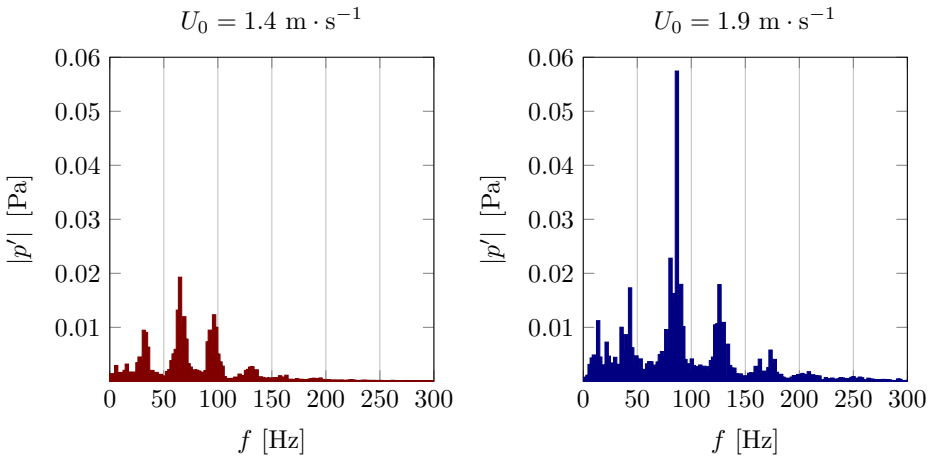

Figure 4.14: Spectra of the radiated sound pressure for $U_0 = 1.4$ m · s^{-1} (left) and $U_0 = 1.9$ m · s^{-1}. Note that 0.06 Pa ∼ 67 dB.

of compactness is valid. Examples of radiated sound pressure spectra are in Fig. 4.14. Amplitudes of the radiated sound pressure increase and the dominance of the 2nd harmonic becomes more pronounced with increasing U_0.

The sound intensity emitted from a single cylinder shall scale [16]

$$I \sim \rho_0 U_0^3 \mathrm{Ma}^3 \mathrm{Sr}^2 \,. \tag{4.16}$$

Hence, it is reasonable to fit this dependence to the numerically obtained values. For clarity (the $U_0^3\mathrm{Ma}^3$ dependence is hard to be checked visually) and for the noise control applicability the results are expressed in terms of sound intensity level L_I rather than the intensity itself:

$$L_I = 10 \log_{10} \frac{I}{I_0} \,, \quad I_0 = 10^{-12} \text{ W} \cdot \text{m}^{-2} \,. \tag{4.17}$$

The results are depicted in Fig. 4.15. Evidently, the scaling derived for a single cylinder (Eq. 4.15) applies to the array as well. It is highly probable that the deviations from the ideal curve are not due to a qualitatively new phenomenon but simply due to some degree of randomness in the signal, that would require much longer timespans to be studied by means of signal processing techniques. It should be taken into account, that the investigated signal consists of ca. 20 periods of the fundamental frequency and it is computationally demanding to calculate much longer ranges. The proportionality constant (found to be 90.2 here) is expected smaller than one for a single cylinder [16]. Note, however, that the presented scenario consists of 76 cylinders and that the coolant tubes inside the exchanger see much more perturbed flow than a solitary cylinder would (see Fig. 4.16), which in turn results in significantly higher pressure perturbations taking place near the coolant tubes' surfaces.

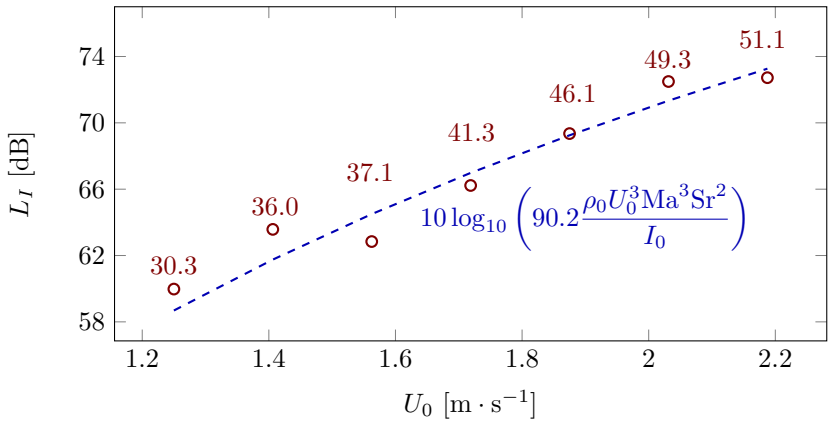

Figure 4.15: Sound intensity level radiated from the tube array (red circles), fitted theoretical prediction (blue dashed line) and the values of the radiated intensity in dB[A] (i.e. with the A weighting filter – numbers above the circles).

One shall take caution when interpreting the intensity level of the emitted noise. For noise control purposes, it is worth noting that the emitted frequencies are quite low and hence the A filtering presents a significant change to the data (see e.g., [129]). Therefore, the values of sound intensity level in dB[A] are given in Fig. 4.15 as well.

It was confirmed that the scaling of the radiated intensity $\sim \rho_0 U_0^3 \mathrm{Ma}^3 \mathrm{Sr}^2$ is relevant. Such an information provides an useful insight that might be supplemented to the heat exchanger design.

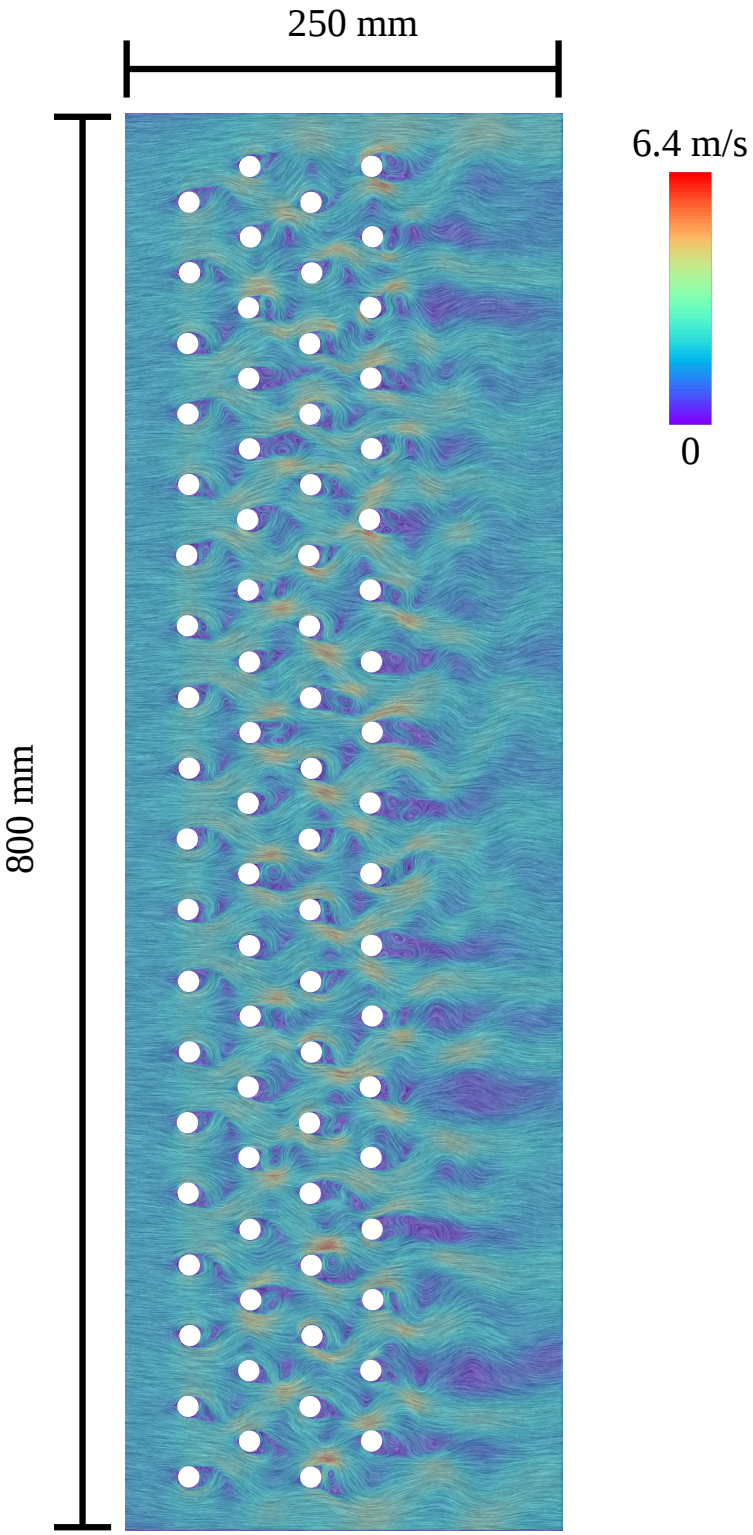

Figure 4.16: Instantaneous flow field through the coolant tubes array with $U_0 = 1.9\ \mathrm{m} \cdot \mathrm{s}^{-1}$. The color scale reflects the velocity magnitude.

Chapter 5

Conclusions

This thesis dealt with chosen topics from the aeroacoustics of periodic structures. The current state of the art is summarized in the Introduction along with the specific aims of this work.

A critical analysis of the application of the frequency-domain linearized Navier-Stokes equations on the case of sound transmission above a corrugated plate with non-zero airflow was conducted (Sec. 3.1). It was found out that the correspondence with the experiment is very limited in this case. It was shown that the explanation points at the questionable linearization of the hydrodynamical perturbations.

An extension and clarification of the previously proposed phenomenological model for sound generation in corrugated pipes were given (Sec. 3.2). Using optimization methods the model constants were found resulting in a good match with experiments. In order to assess the influence of finite-amplitude sound propagation on the source-resonance coupling, a weakly-nonlinear model was proposed as an extension to the linear one (Sec. 3.2.5). It was demonstrated that the higher harmonics are generated in the mode-locked states.

In Sec. 4 it was investigated how the periodic arrangement of heat exchanger coolant tubes can be described as a sonic crystal. It was shown that even for finite structures consisting of four rows of coolant tubes the theory of wave propagation through periodic media is applicable and proves to be in accordance with the experiment. Further, it was demonstrated that the thermoviscous losses do not alter the bandgap structure of the crystal, so they can be safely omitted in the preliminary design of the heat exchanger geometry (even with the presence of cooling fins). A pilot case of heat exchanger design exploiting the local resonance to block some of the low frequencies is given (Sec. 4.1.3). Finally, the noise generated by the unsteady flow through the tube array was investigated by numerical simulations (Sec. 4.2). It was demonstrated that the radiated sound intensity is proportional to the previously derived dependence valid for a single cylinder and the Strouhal law governs the fundamental frequency with $\mathrm{Sr} = 0.27$.

Specific aims of the thesis were fulfilled. The results were published (or sent

for publication – see below) as well as discussed at the international conferences (FCAC 2018, ICA 2019), seminars and workshops (meetings of COST Action DENORMS, DGLR Workshop Strömungsschall in Luftfahrt, Fahrzeug- und Anlagentechnik). Some of the results were obtained in cooperation with foreign organizations (Laboratory of Acoustics of Le Mans Université, Institute of Process Machinery and Systems Engineering, Friedrich-Alexander-University Erlangen-Nuernberg).

In the future, the investigation of the sound transmission above the corrugated plate can be re-expressed in terms of the governing equations linearized for the acoustic perturbations while retaining the nonlinearity of the hydrodynamical ones (see, e.g., [130, 56]) in order to avoid the discrepancies taking place with the fully linearized formulation. In the phenomenological model of sound generation in corrugated tubes, the influence of the radiation boundary conditions shall be studied to bring the model closer to the experimental results. Treatment of the periodic heat exchanger arrangements shall include the effects of inhomogeneous temperature field, as it would be for the working device, and experimental investigation of flow-acoustic interactions shall take place.

5.1 List of author's publications

5.1.1 Related to the thesis

Publications indexed in Web of Science – accepted & published

- HRUŠKA, Viktor, Michal BEDNAŘÍK and Milan ČERVENKA. *Weakly nonlinear oscillations of gas column driven by self-sustained sources.* MATEC Web of Conferences. 2019, **283**.

Publications indexed in Scopus – accepted & published

- HRUŠKA, Viktor, Michal BEDNAŘÍK and Milan ČERVENKA. *Method of estimation of frequency spectrum and power of the sound generated by an unsteady flow through a sonic crystal.* Proceedings of the International Congress on Acoustics (ICA), Aachen, Germany, 2019.

Publications indexed in Web of Science – submitted

- HRUŠKA, Viktor and Michal BEDNAŘÍK. *Time domain phenomenological formulation for the sound generation in corrugated pipes.* Submitted to Archive of Applied Mechanics.
- CZWIELONG, Felix, HRUŠKA, Viktor, BEDNAŘÍK Michal and Stefan BECKER. *On the acoustic effects of sonic crystals in heat exchanger arrangements.* Submitted to Applied Acoustics.

Other

- HRUŠKA, Viktor and Michal BEDNAŘÍK. *Fenomenologický model generování zvuku ve vroubkovaných trubicích a jeho modální řešení [Phenomenological Model of Sound Generation in a Corrugated Pipe and its Modal Solution]*. Akustické listy. 2017, **23**(1-4).

5.1.2 Not related to the thesis

Publications indexed in Web of Science – accepted & published

- HRUŠKA, Viktor and Pavel DLASK. *On a Robust Descriptor of the Flue Organ Pipe Transient*. Archives of Acoustics. 2020, **45**(3), 377-384.
- HRUŠKA, Viktor and Pavel DLASK. *Investigation of the Sound Source Regions in Open and Closed Organ Pipes*. Archives of Acoustics. 2019, **44**(3), 467-474.
- FRIČ, Marek and Viktor HRUŠKA. *The effect of resonance tubes on facial and laryngeal vibration – A case study*. Biomedical Signal Processing and Control. 2017, **37**,
- HRUŠKA, Viktor and Pavel DLASK. *Connections between Organ Pipe Noise and Shannon Entropy of the Airflow: Preliminary Results*. Acta Acustica united with Acustica. 2017, **103**(6), 1100-1105.

Bibliography

[1] V. Strouhal. Ueber eine besondere art der tonerregung. *Annalen der Physik und Chemie*, 241(10):216–251, 1878.

[2] Lord Rayleigh. XVII. on the maintenance of vibrations by forces of double frequency, and on the propagation of waves through a medium endowed with a periodic structure. *The London, Edinburgh, and Dublin Philosophical Magazine and Journal of Science*, 24(147):145–159, aug 1887.

[3] Charles Kittel. *Introduction to Solid State Physics*. John Wiley & Sons Inc, 2004.

[4] Arpan Gupta. A review on sonic crystal, its applications and numerical analysis techniques. *Acoustical Physics*, 60(2):223–234, mar 2014.

[5] M. S. Kushwaha, P. Halevi, L. Dobrzynski, and B. Djafari-Rouhani. Acoustic band structure of periodic elastic composites. *Physical Review Letters*, 71(13):2022–2025, sep 1993.

[6] M. Sigalas and E.N. Economou. Band structure of elastic waves in two dimensional systems. *Solid State Communications*, 86(3):141–143, apr 1993.

[7] R. Martínez-Sala, J. Sancho, J. V. Sánchez, V. Gómez, J. Llinares, and F. Meseguer. Sound attenuation by sculpture. *Nature*, 378(6554):241–241, nov 1995.

[8] Manvir S. Kushwaha. Stop-bands for periodic metallic rods: Sculptures that can filter the noise. *Applied Physics Letters*, 70(24):3218–3220, jun 1997.

[9] J. V. Sánchez-Pérez, D. Caballero, R. Mártinez-Sala, C. Rubio, J. Sánchez-Dehesa, F. Meseguer, J. Llinares, and F. Gálvez. Sound attenuation by a two-dimensional array of rigid cylinders. *Physical Review Letters*, 80(24):5325–5328, jun 1998.

[10] Carlos Barceló, Stefano Liberati, and Matt Visser. Analogue gravity. *Living Reviews in Relativity*, 8(1), dec 2005.

[11] M. J. Lighthill. On sound generated aerodynamically. i. general theory. *Proceedings of the Royal Society of London. Series A, Mathematical and Physical Sciences*, 211(1107):564–587, 1952.

[12] M. J. Lighthill. On sound generated aerodynamically. ii. turbulence as source of sound. *Proceedings of the Royal Society of London. Series A, Mathematical and Physical Sciences*, 222(1148):1–32, 1954.

[13] Shon Eirwyn Ffowcs-Williams and David Hawkings. Sound generation by turbulence and surfaces in arbitrary motion. *Philosophical Transactions of the Royal Society of London. Series A, Mathematical and Physical Sciences*, 264(1151):321–342, may 1969.

[14] M. L. Munjal. *Acoustics of ducts and mufflers with application to exhaust and ventilation system design*. Wiley, New York, 1987.

[15] B. Rajavel and M. G. Prasad. Acoustics of corrugated pipes: A review. *Applied Mechanics Reviews*, 65, 2013.

[16] M. S. Howe. *Acoustics of Fluid-Structure Interactions*. Cambridge University Press, aug 1998.

[17] Yves Aurégan, Vincen Pagneux, Jean-Francois Pinton, and Agnes Maurel, editors. *Sound-Flow Interactions*. Springer Berlin Heidelberg, 2002.

[18] M. S. Howe. *Theory of Vortex Sound*. Cambridge University Press, Cambridge, 2002.

[19] Munjal. *Acoustics of Ducts and Muffler*. John Wiley & Sons, 2014.

[20] Stewart Glegg and William Davenport. *Aeroacoustics of low Mach number flows*. Academic Press, 2017.

[21] Vincent Laude. *Phononic Crystals*. DE GRUYTER, jan 2015.

[22] A. Khelif and A. Adibi. *Phononic Crystals*. Springer-Verlag GmbH, 2015.

[23] Vicente Romero Garcia and Anne-Christine Hladky-Hennion. *Fundamentals and Applications of Acoustic Metamaterials*. ISTE Ltd, 2019.

[24] Jay Hardin. *Computational Aeroacoustics*. Springer New York, New York, NY, 1993.

[25] Sanjiva K. Lele and Joseph W. Nichols. A second golden age of aeroacoustics? *Philosophical Transactions of the Royal Society A: Mathematical, Physical and Engineering Sciences*, 372(2022):20130321, aug 2014.

[26] Stefan Schoder and Manfred Kaltenbacher. Hybrid aeroacoustic computations: State of art and new achievements. *Journal of Theoretical and Computational Acoustics*, 27(04):1950020, dec 2019.

[27] Claus Albrecht Wagner, Thomas Huettl, and Pierre Sagaut. *Large-Eddy Simulation for Acoustics*. Cambridge University Press, 2016.

[28] Toyokatsu Miyashita. Sonic crystals and sonic wave-guides. *Measurement Science and Technology*, 16(5):R47–R63, apr 2005.

[29] Ming-Hui Lu, Liang Feng, and Yan-Feng Chen. Phononic crystals and acoustic metamaterials. *Materials Today*, 12(12):34–42, dec 2009.

[30] Yan Pennec, Jérôme O. Vasseur, Bahram Djafari-Rouhani, Leonard Dobrzyński, and Pierre A. Deymier. Two-dimensional phononic crystals: Examples and applications. *Surface Science Reports*, 65(8):229–291, aug 2010.

[31] Mahmoud I. Hussein, Michael J. Leamy, and Massimo Ruzzene. Dynamics of phononic materials and structures: Historical origins, recent progress, and future outlook. *Applied Mechanics Reviews*, 66(4), may 2014.

[32] Luca Fredianelli, Alessandro Del Pizzo, and Gaetano Licitra. Recent developments in sonic crystals as barriers for road traffic noise mitigation. *Environments*, 6(2):14, jan 2019.

[33] Noé Jiménez, Ahmed Mehrem, Rubén Picó, Lluís M. García-Raffi, and Víctor J. Sánchez-Morcillo. Nonlinear propagation and control of acoustic waves in phononic superlattices. *Comptes Rendus Physique*, 17(5):543–554, may 2016.

[34] J. M. Herrero, S. García-Nieto, X. Blasco, V. Romero-García, J. V. Sánchez-Pérez, and L. M. Garcia-Raffi. Optimization of sonic crystal attenuation properties by ev-MOGA multiobjective evolutionary algorithm. *Structural and Multidisciplinary Optimization*, 39(2):203–215, oct 2008.

[35] Daniel P. Elford, Luke Chalmers, Feodor V. Kusmartsev, and Gerry M. Swallowe. Matryoshka locally resonant sonic crystal. *The Journal of the Acoustical Society of America*, 130(5):2746–2755, nov 2011.

[36] Giorgio Palma, Huina Mao, Lorenzo Burghignoli, Peter Göransson, and Umberto Iemma. Acoustic metamaterials in aeronautics. *Applied Sciences*, 8(6):971, jun 2018.

[37] L.M. Garcia-Raffi, L.J. Salmerón-Contreras, I. Herrero-Durá, R. Picó, J. Redondo, V.J. Sánchez-Morcillo, K. Staliunas, N.J.E. Adkins, A. Cebrecos, N. Jiménez, and V. Romero-García. Broadband reduction of the specular reflections by using sonic crystals: A proof of concept

for noise mitigation in aerospace applications. *Aerospace Science and Technology*, 73:300–308, feb 2018.

[38] Umberto Iemma, Michael Carley, and Riccardo Pellegrini. Tailoring acoustic metamaterials to aeroacoustic applications. In *INTERNOISE 2014 - 43rd International Congress on Noise Control Engineering*, 2014.

[39] Xiwen Dai and Yves Aurégan. Acoustic of a perforated liner with grazing flow: Floquet-bloch periodical approach versus impedance continuous approach. *The Journal of the Acoustical Society of America*, 140(3):2047–2055, sep 2016.

[40] Xiwen Dai and Yves Aurégan. A cavity-by-cavity description of the aeroacoustic instability over a liner with a grazing flow. *Journal of Fluid Mechanics*, 852:126–145, aug 2018.

[41] Joachim Golliard, Yves Aurégan, and Thomas Humbert. Experimental study of plane wave propagation in a corrugated pipe: Linear regime of acoustic-flow interaction. *Journal of Sound and Vibration*, 472:115158, apr 2020.

[42] Yves Aurégan and Vincent Pagneux. Slow sound in lined flow ducts. *The Journal of the Acoustical Society of America*, 138(2):605–613, aug 2015.

[43] Yves Aurégan, Pierre Fromholz, Florent Michel, Vincent Pagneux, and Renaud Parentani. Slow sound in a duct, effective transonic flows, and analog black holes. *Physical Review D*, 92(8), oct 2015.

[44] Antonin Coutant, Yves Aurégan, and Vincent Pagneux. Slow sound laser in lined flow ducts. *The Journal of the Acoustical Society of America*, 146(4):2632–2644, oct 2019.

[45] Marvin E. Goldstein. *Aeroacoustics*. McGraw-Hill International Book Company, 1976.

[46] Sjoerd W. Rienstra and Avraham Hirschberg. An introduction to acoustics. [online 28-Nov-2019] https://www.win.tue.nl/ sjoerdr/papers/boek.pdf, 2019.

[47] Jan Delfs. Basics of aeroacoustics. `https://dlr.de/as/Portaldata/5/Resources/dokumente/abteilungen/abt_ta/Notes_Basics_of_Aeroacoustics_Delfs.pdf`, 2016. [Accessed 11-Jun-2020].

[48] G. K. Batchelor. *An Introduction to Fluid Dynamics*. Cambridge University Press, Cambridge, 2000.

[49] D. T. Blackstock. *Fundamentals of Physical Acoustics*. Wiley & Sons, New York, 2000.

[50] B. Lautrup. *Physics of Continuous Matter*. Taylor & Francis Inc, 2011.

[51] Paul Maneville. *Instabilities, Chaos and Turbulence*. Imperial College Press, London, 2010.

[52] G. Nakiboglu, S. Belfroid, J. Willems, and A. Hirschberg. Whistling behavior of periodic systems: Corrugated pipes and multiple side branch system. *International Journal of Mechanical Sciences*, 52, 2010.

[53] M. F. Hamilton, David T. Blackstock, and et al. *Nonlinear Acoustics*. Acoustical Society of America, Melville, NY, 2008.

[54] *Acoustics Module User's Guide, version 5.5*. COMSOL, 2019.

[55] R. Ewert and W. Schröder. On the simulation of trailing edge noise with a hybrid LES/APE method. *Journal of Sound and Vibration*, 270(3):509–524, feb 2004.

[56] Jung H. Seo and Young J. Moon. Linearized perturbed compressible equations for low mach number aeroacoustics. *Journal of Computational Physics*, 218(2):702–719, nov 2006.

[57] Samuel Newby Curle. The influence of solid boundaries upon aerodynamic sound. *Proceedings of the Royal Society of London. Series A. Mathematical and Physical Sciences*, 231(1187):505–514, sep 1955.

[58] Ernst-August Müller and Frank Obermeier. Vortex sound. *Fluid Dynamics Research*, 3(1-4):43–51, sep 1988.

[59] Alan Powell. Theory of vortex sound. *The Journal of the Acoustical Society of America*, 36(1):177–195, jan 1964.

[60] Wilhelm Möhring. On vortex sound at low mach number. *Journal of Fluid Mechanics*, 85(4):685–691, apr 1978.

[61] Sjoerd W. Rienstra. A classification of duct modes based on surface waves. *Wave Motion*, 37(2):119–135, feb 2003.

[62] Philip E. Doak. Fluctuating total enthalpy as the basic generalized acoustic field. *Theoretical and Computational Fluid Dynamics*, 10(1-4):115–133, jan 1998.

[63] Marvin E. Goldstein. A generalized acoustic analogy. *Journal of Fluid Mechanics*, 488:315–333, jul 2003.

[64] Michael S. Howe. The dissipation of sound at an edge. *Journal of Sound and Vibration*, 70(3):407–411, jun 1980.

[65] Stephen B. Pope. *Turbulent Flows*. Cambridge University Pr., 2000.

[66] David C. Wilcox. *Turbulence Modeling for CFD*. D C W Industries; 3rd edition, 2006.

[67] Christopher Rumsey. Nasa turbulence modeling resource. `http://turbmodels.larc.nasa.gov/`, 2020. Accessed: 2020-06-17.

[68] Paul G. Tucker. *Computation of Unsteady Internal Flows*. Springer US, 2001.

[69] Valentin Joseph Boussinesq. *Essai sur la théorie des eaux courantes*. Mémoires présentés par divers savants à l'Académie des sciences de l'Institut national de France. Imprimerie Nationale, 1877.

[70] Florian R. Menter. Two-equation eddy-viscosity turbulence models for engineering applications. *AIAA Journal*, 32(8):1598–1605, aug 1994.

[71] *CFD Module User's Guide, version 5.5*. COMSOL, 2019.

[72] John Seiner, Bernard Jansen, and Nathan Murray. Aero-performance efficient noise suppression of a supersonic model twin jet nacelle. In *15th AIAA/CEAS Aeroacoustics Conference (30th AIAA Aeroacoustics Conference)*. American Institute of Aeronautics and Astronautics, may 2009.

[73] Christopher K. W. Tam. *Computational Aeroacoustics*. Cambridge University Press, 2012.

[74] Axel Kierkegaard, Susann Boij, and Gunilla Efraimsson. A frequency domain linearized navier–stokes equations approach to acoustic propagation in flow ducts with sharp edges. *The Journal of the Acoustical Society of America*, 127(2):710–719, feb 2010.

[75] Massimo Emiliano D'Elia, Thomas Humbert, Yves Auregan, and Joachim Golliard. Optical measurements of the linear sound-flow interaction above a corrugated plate. In *25th AIAA/CEAS Aeroacoustics Conference*. American Institute of Aeronautics and Astronautics, may 2019.

[76] Lin Du, Andreas Holmberg, Mikael Karlsson, and Mats Åbom. Sound amplification at a rectangular t-junction with merging mean flows. *Journal of Sound and Vibration*, 367:69–83, apr 2016.

[77] Hendrik C. Kuhlmann and Francesco Romanò. The lid-driven cavity. In *Computational Methods in Applied Sciences*, pages 233–309. Springer International Publishing, jul 2018.

[78] Brian Cabral and Leith Leedom. Imaging vector fields using line integral convolution. In *Proceedings of the 20th annual conference on Computer graphics and interactive techniques. SIGGRAPH '93*, 1993.

[79] Chenyang Weng, Susann Boij, and Ardeshir Hanifi. The attenuation of sound by turbulence in internal flows. *The Journal of the Acoustical Society of America*, 133(6):3764–3776, jun 2013.

[80] A. Kierkegaard, S. Boij, and G. Efraimsson. Simulations of the scattering of sound waves at a sudden area expansion. *Journal of Sound and Vibration*, 331(5):1068–1083, feb 2012.

[81] *Acoustics Module User's Guide, version 5.3*. COMSOL, 2017.

[82] A.M. Petrie and I.D. Huntley. The acoustic output produced by a steady airflow through a corrugated duct. *Journal of Sound and Vibration*, 70(1):1–9, may 1980.

[83] Y Nakamura and N Fukamachi. Sound generation in corrugated tubes. *Fluid Dynamics Research*, 7(5-6):255–261, aug 1991.

[84] Ulf R. Kristiansen and Geir A. Wiik. Experiments on sound generation in corrugated pipes with flow. *The Journal of the Acoustical Society of America*, 121(3):1337–1344, mar 2007.

[85] Vincent Debut, José Antunes, and Miguel Moreira. Experimental study of the flow-excited acoustical lock-in in a corrugated pipe. In *ICSV14*, page 9, Cairns, 2007.

[86] Güneş Nakiboğlu, Oleksii Rudenko, and Avraham Hirschberg. Aeroacoustics of the swinging corrugated tube: Voice of the dragon. *The Journal of the Acoustical Society of America*, 131(1):749–765, jan 2012.

[87] O. Rudenko, G. Nakiboglu, and A. Hirschberg. On whistling of pipes with a corrugated pipe segment. In *10th International Conference on Flow-Induced Vibration (& Flow-Induced Noise) (FIV2012)*, 2012.

[88] M. Amielh, F. Anselmet, Y. Jiang, U. Kristiansen, P.-O. Mattei, D. Mazzoni, and C. Pinhède. Aeroacoustic source analysis in a corrugated flow pipe using low-frequency mitigation. *Journal of Turbulence*, 15(10):650–676, jul 2014.

[89] Hee-Chang LIM and Faran RAZI. Experimental study of flow-induced whistling in pipe systems including a corrugated section. *Energies*, 11(8):1954, jul 2018.

[90] Oleksii Rudenko, Güneş Nakiboğlu, Ad Holten, and Avraham Hirschberg. On whistling of pipes with a corrugated segment: Experiment and theory. *Journal of Sound and Vibration*, 332(26):7226–7242, dec 2013.

[91] Joachim Golliard, Néstor González-Díez, Stefan Belfroid, Günes Nakiboglu, and Avraham Hirschberg. U-RANS model for the prediction of the acoustic sound power generated in a whistling corrugated pipe. In *Volume 4: Fluid-Structure Interaction*, page 6. ASME, jul 2013.

[92] Mihaela Popescu and Stein Tore Johansen. Acoustic wave propagation in low mach flow pipe. In *46th AIAA Aerospace Sciences Meeting and Exhibit*, pages 1–15, 2008.

[93] M. Popescu, S. T. Johansen, and W. Shyy. Flow-induced acoustics in corrugated pipes. *Commun. Comput. Phys.*, 10, 2011.

[94] M. L. Facchinetti, E. de Langre, and F. Biolley. Vortex shedding modeling using diffusive van der pol oscillators. *C. R. Mecanique*, 330:451–456, 2002.

[95] M.L. Facchinetti, E. de Langre, and F. Biolley. Coupling of structure and wake oscillators in vortex-induced vibrations. *Journal of Fluids and Structures*, 19(2):123–140, feb 2004.

[96] Matteo Luca Facchinetti, Emmanuel de Langre, and Francis Biolley. Vortex-induced travelling waves along a cable. *European Journal of Mechanics - B/Fluids*, 23(1):199–208, jan 2004.

[97] L. Mathelin and E. de Langre. Vortex-induced vibrations and waves under shear flow with a wake oscillator model. *European Journal of Mechanics - B/Fluids*, 24(4):478–490, jul 2005.

[98] E. de Langre. Frequency lock-in is caused by coupled-mode flutter. *Journal of Fluids and Structures*, 22(6-7):783–791, aug 2006.

[99] Aleš Tondl and Radoslav Nabergoj. Non-periodic and chaotic vibrations in a flow induced system. *Chaos, Solitons & Fractals*, 4(12):2193–2202, dec 1994.

[100] D.W. Storti and R.H. Rand. Dynamics of two strongly coupled van der pol oscillators. *International Journal of Non-Linear Mechanics*, 17(3):143–152, jan 1982.

[101] A. Tondl. Passive and active means for self-excited vibration suppressing: Two-mass model. *Engineering Mechanics*, 15(2):133–138, May 2008.

[102] T. Bakri, R. Nabergoj, and A. Tondl. Multi-frequency oscillations in self-excited systems. *Nonlinear Dynamics*, 48(1-2):115–127, sep 2006.

[103] Ferdinand Verhulst. Quenching of self-excited vibrations. *Journal of Engineering Mathematics*, 53(3-4):349–358, dec 2005.

[104] F. Verhulst and Abadi. Autoparametric resonance of relaxation oscillations. *ZAMM*, 85(2):122–131, feb 2005.

[105] V. Debut, J. Antunes, and M. Moreira. A phenomenological model for sound generation in corrugated pipes. In *Proceedings of ISMA*, page 7, 2007.

[106] V. Debut, J. Antunes, and M. Moreira. Flow-acoustic interaction in corrugated pipes: Time-domain simulation of experimental phenomena. In *Flow Induced Vibration*, page 6, Prague, 2008.

[107] J.C. Bruggeman, A. Hirschberg, M.E.H. van Dongen, A.P.J. Wijnands, and J. Gorter. Self-sustained aero-acoustic pulsations in gas transport systems: Experimental study of the influence of closed side branches. *Journal of Sound and Vibration*, 150(3):371–393, nov 1991.

[108] J. W. Elliot. *Lecture notes on the mathematics of acoustics*, chapter Corrugated pipe flow. London: Imperial College Press, 2005.

[109] M. C. A. M. Peters, A. Hirschberg, A. J. Reijnen, and A. P. J. Wijnands. Damping and reflection coefficient measurements for an open pipe at low mach and low helmholtz numbers. *Journal of Fluid Mechanics*, 256:499–534, nov 1993.

[110] Uno Ingard and Vijay K. Singhal. Effect of flow on the acoustic resonances of an open-ended duct. *The Journal of the Acoustical Society of America*, 58(4):788–793, oct 1975.

[111] Steven H. Strogatz. *Nonlinear Dynamics and Chaos*. CRC Press, 2018.

[112] W J Cunningham. *Introduction to Nonlinear Analysis*. Mcgraw Hill, 1958.

[113] Henry D. I. Abarbanel, Mikhail I. Rabinovich, and Mikhail M. Sushchik. *Introduction to Nonlinear Dynamics for Physicists*, chapter Scenarios of the Onset of Chaos. Chaos through Quasi-Periodicity, pages 132–137. WORLD SCIENTIFIC PUB CO INC, 1993.

[114] Eric Jones, Travis Oliphant, Pearu Peterson, et al. SciPy: Open source scientific tools for Python, 2001–. [Online; accessed <today>].

[115] Mitsuo Gen and Runwei Cheng. *Genetic Algorithms and Engineering Optimization*. John Wiley & Sons, Inc., dec 1999.

[116] James Baker. Reducing bias and inefficiency in the selection algorithm. In *Proceedings of the Second International Conference on Genetic Algorithms on Genetic algorithms and their application*, 1987.

[117] Ulf R. Kristiansen, Pierre-Olivier Mattei, Cedric Pinhede, and Muriel Amielh. Experimental study of the influence of low frequency flow modulation on the whistling behavior of a corrugated pipe. *The Journal of the Acoustical Society of America*, 130(4):1851–1855, oct 2011.

[118] Viktor Hruška, Michal Bednařík, and Milan Červenka. Weakly nonlinear oscillations of gas column driven by self-sustained sources. *MATEC Web of Conferences*, 283:06001, 2019.

[119] Michal Bednarik and Milan Cervenka. Equations for description of nonlinear standing waves in constant-cross-sectioned resonators. *The Journal of the Acoustical Society of America*, 135(3):EL134–EL139, mar 2014.

[120] Yurii A. Ilinskii, Bart Lipkens, Timothy S. Lucas, Thomas W. Van Doren, and Evgenia A. Zabolotskaya. Nonlinear standing waves in an acoustical resonator. *The Journal of the Acoustical Society of America*, 104(5):2664–2674, nov 1998.

[121] William H. Press, Saul A. Teukolsky, William T. Vetterling, and Brian P. Flannery. *Numerical Recipes*. Cambridge University Pr., 2007.

[122] A. C. Hindmarsh. ODEPACK, a systematized collection of ODE solvers. *IMACS Transactions on Scientific Computation*, 1:55–64, 1983.

[123] Florian J. Krömer. *Sound emission of low-pressure axial fans under distorted inflow conditions*, volume Reihe B: Medizin. FAU University Press, 2018.

[124] Felix Czwielong, Viktor Hruska, Michal Bednarik, and Stefan Becker. On the acoustic effects of sonic crystals in heatexchanger arrangements. *Applied Acoustics [in review]*, 2021.

[125] Florian Zenger, Gert Herold, and Stefan Becker. Acoustic characterization of forward- and backward-skewed axial fans under increased inflow turbulence. In *22nd AIAA/CEAS Aeroacoustics Conference*. American Institute of Aeronautics and Astronautics, may 2016.

[126] Zixian Liang and Jensen Li. Extreme acoustic metamaterial by coiling up space. *Physical Review Letters*, 108(11), mar 2012.

[127] M. S. Howe. The generation of sound by aerodynamic sources in an inhomogeneous steady flow. *Journal of Fluid Mechanics*, 67(3):597–610, feb 1975.

[128] Viktor Hruska, Michal Bednarik, and Milan Cervenka. Methods of estimation of frequency spectrum and power of the sound generated by an unsteady flow through a sonic crystal. *Proceedings of the ICA 2019 and EAA Euroregio : 23rd International Congress on Acoustics*, integrating 4th EAA Euroregio 2019 : 9-13 September 2019:9 Sep 2019–13 Sep 2019; Aachen (2019)., 2019.

[129] William M. Hartmann. *Signals, Sound, and Sensation*. American Inst. of Physics, 2004.

[130] Jung-Hee Seo and Young J. Moon. Perturbed compressible equations for aeroacoustic noise prediction at low mach numbers. *AIAA Journal*, 43(8):1716–1724, aug 2005.

[131] John Guckenheimer, Kathleen Hoffman, and Warren Weckesser. The forced van der pol equation i: The slow flow and its bifurcations. *SIAM Journal on Applied Dynamical Systems*, 2(1):1–35, jan 2003.

Appendices

Appendix A – Notational conventions

Since there is only a low risk of confusion, no special notation is introduced to distinguish between vector and tensor variables.

Dyadic product $\boldsymbol{ab}$ and nabla operator $\boldsymbol{\nabla}$

Within this work the dyadic product of two vectors is not denoted by any special mark and it is put simply as $\boldsymbol{ab}$, where

$$\boldsymbol{ab} = \begin{pmatrix} a_1b_1 & a_1b_2 & a_1b_3 \\ a_2b_1 & a_2b_2 & a_2b_3 \\ a_3b_1 & a_3b_2 & a_3b_3 \end{pmatrix} . \tag{5.1}$$

In the same manner, the nabla operator on the vector field $\boldsymbol{\nabla a}$ results in the second-rank tensor field:

$$\boldsymbol{\nabla a} = \begin{pmatrix} \dfrac{\partial a_1}{\partial x_1} & \dfrac{\partial a_1}{\partial x_2} & \dfrac{\partial a_1}{\partial x_3} \\ \dfrac{\partial a_2}{\partial x_1} & \dfrac{\partial a_2}{\partial x_2} & \dfrac{\partial a_2}{\partial x_3} \\ \dfrac{\partial a_3}{\partial x_1} & \dfrac{\partial a_3}{\partial x_2} & \dfrac{\partial a_3}{\partial x_3} \end{pmatrix} . \tag{5.2}$$

Conversely, the divergence of a second-rank tensor field $\boldsymbol{c} = c_{ij}$ is a vector field given as:

$$\boldsymbol{\nabla} \cdot \boldsymbol{c} = \begin{pmatrix} \dfrac{\partial c_{11}}{\partial x_1} + \dfrac{\partial c_{12}}{\partial x_2} + \dfrac{\partial c_{13}}{\partial x_3} \\ \dfrac{\partial c_{21}}{\partial x_1} + \dfrac{\partial c_{22}}{\partial x_2} + \dfrac{\partial c_{23}}{\partial x_3} \\ \dfrac{\partial c_{31}}{\partial x_1} + \dfrac{\partial c_{32}}{\partial x_2} + \dfrac{\partial c_{33}}{\partial x_3} \end{pmatrix} . \tag{5.3}$$

Double-dot product $\boldsymbol{a} : \boldsymbol{b}$

The double-dot product of two tensors $\boldsymbol{a}$, $\boldsymbol{b}$ is defined as follows

$$\boldsymbol{a} : \boldsymbol{b} = \mathrm{Tr}\,(\boldsymbol{a} \cdot \boldsymbol{b}) = \sum_{ij} a_{ij} b_{ji} \,, \tag{5.4}$$

where Tr denotes a trace of a matrix.

Material derivative $\mathrm{D}/\mathrm{D}t$

The material (substantial, Lagrangian etc.) derivative of a scalar quantity $a(\boldsymbol{x}, t)$ defined within the fluid flow of velocity $\boldsymbol{u}$ is given as

$$\frac{\mathrm{D}a}{\mathrm{D}t} = \frac{\partial a}{\partial t} + \boldsymbol{u} \cdot \boldsymbol{\nabla} a = \frac{\partial a}{\partial t} + \sum_i u_i \frac{\partial a}{\partial x_i} \,, \tag{5.5}$$

where the last expression holds for components in Cartesian coordinates.

For a vector quantity $\boldsymbol{b}(\boldsymbol{x}, t)$ the definition is analogous, but some attention shall be given to the second term:

$$\frac{\mathrm{D}\boldsymbol{b}}{\mathrm{D}t} = \frac{\partial \boldsymbol{b}}{\partial t} + \boldsymbol{u} \cdot \boldsymbol{\nabla} \boldsymbol{b} = \frac{\partial \boldsymbol{b}}{\partial t} + \begin{pmatrix} u_1 \dfrac{\partial b_1}{\partial x_1} + u_2 \dfrac{\partial b_1}{\partial x_2} + u_3 \dfrac{\partial b_1}{\partial x_3} \\ u_1 \dfrac{\partial b_2}{\partial x_1} + u_2 \dfrac{\partial b_2}{\partial x_2} + u_3 \dfrac{\partial b_2}{\partial x_3} \\ u_1 \dfrac{\partial b_3}{\partial x_1} + u_2 \dfrac{\partial b_3}{\partial x_2} + u_3 \dfrac{\partial b_3}{\partial x_3} \end{pmatrix} \,, \tag{5.6}$$

and again, the last expression employs components in Cartesian coordinates.

Appendix B – Generalized functions

Concepts utilizing generalized functions, well-known also from the classic acoustics of stagnant media, have found many useful applications in the field of aeroacoustics. The following paragraphs aim for listing their definitions and most handy properties, not for rigorously deriving them. A more detailed treatment for the purpose of aeroacoustics could be found e.g. in [16, 18, 47, 46].

Dirac delta function δ

The Dirac delta function $\delta(x)$ is defined by fulfilling the following three properties:

$$\delta(x \neq 0) = 0 \,, \tag{5.7}$$

$$\delta(0) = \infty \,, \tag{5.8}$$

$$\int_{-\infty}^{\infty} \delta(x) = 1 \,. \tag{5.9}$$

Seemingly unnatural behavior is expounded by realising that these conditions can be reconstructed by considering the Gaussian curve of finite width, that is made narrower while retaining the surface under the curve (see Fig. 5.1). Formally:

$$\delta(x) = \lim_{\sigma \to 0} \frac{1}{|\sigma|\sqrt{\pi}} e^{-\frac{x^2}{\sigma^2}} \,. \tag{5.10}$$

An important property of the Dirac delta function involves integrating a product of the Dirac function with some classical "well-behaved" function $g(x)$, which results in the well-known sampling property:

$$\int_{-\infty}^{\infty} g(x)\delta(x - x_0) = g(x_0) \,. \tag{5.11}$$

Generalization to higher dimensions is straightforward. For $\boldsymbol{x} = (x_1, x_2, x_3)$:

$$\delta(\boldsymbol{x}) = \delta(x_1)\delta(x_2)\delta(x_3) \,. \tag{5.12}$$

Heaviside step function H

The Heaviside step function H is defined simply as

$$\mathrm{H}(x < 0) = 0 \,, \tag{5.13}$$

$$\mathrm{H}(x \geq 0) = 1 \,. \tag{5.14}$$

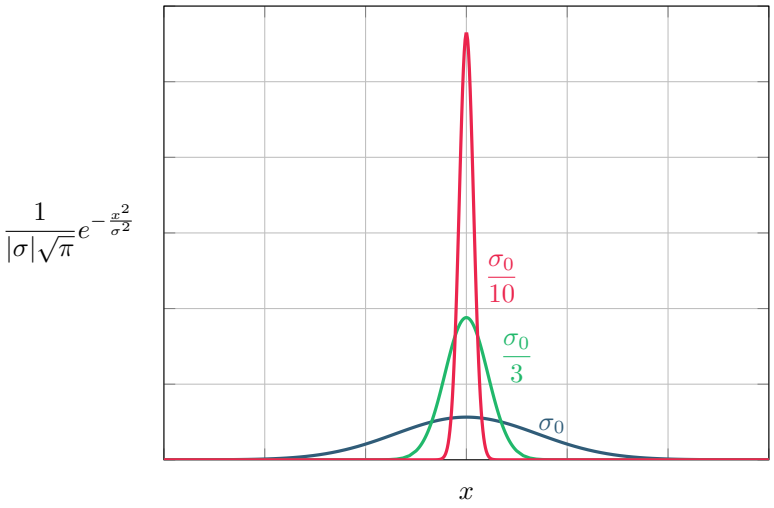

Figure 5.1: Illustration of the limit in Eq. (5.10).

Its relation to the Dirac delta function is not complicated. The Heaviside step function could be found by integrating the Dirac delta function:

$$\mathrm{H}(x) = \int_{-\infty}^{x} \delta(y)\ \mathrm{d}y \tag{5.15}$$

and vice versa

$$\delta(x) = \frac{\mathrm{dH}}{\mathrm{d}x}\ . \tag{5.16}$$

Free-space Green's function

The Green's function solution to the wave propagation problems is a very well-known topic, so the main purpose of the following lines is merely to set the terminology, provide some supplementary comments and prepare the ground for Appendix C dealing with the multipole expansion.

As the Lighthill's (2.56) and Curle's (2.59) equations consist of the d'Alembertian left-hand-side and source terms on the right-hand-side, it is possible to define the free-field Green's function G as the solution to the problem:

$$\nabla^2 G - \frac{1}{c_0^2}\frac{\partial^2 G}{\partial t^2} = \delta(\boldsymbol{x}-\boldsymbol{\xi})\delta(t-\tau)\ . \tag{5.17}$$

Hence, the free-field Green's function G is a solution to the inhomogenous wave equation driven by a point source at $\boldsymbol{\xi}$ that was active only at a singular time instant τ (see e.g., [18]):

$$G\left(\boldsymbol{x}, t|\boldsymbol{\xi}, \tau\right) = \frac{\delta\left(\tau - t + \dfrac{|\boldsymbol{x}-\boldsymbol{\xi}|}{c_0}\right)}{4\pi|\boldsymbol{x}-\boldsymbol{\xi}|}\ . \tag{5.18}$$

Making use of the last expression and the properties of Dirac delta function a solution to the inhomogenous wave equation with force density on the right-hand-side (Eq. (2.39)) may be written:

$$p'(\boldsymbol{x},t) = \boldsymbol{\nabla} \cdot \iiint_{\Omega(\boldsymbol{\xi})} \frac{\boldsymbol{f}\left(t - |\boldsymbol{x}-\boldsymbol{\xi}|/c_0\right)}{4\pi|\boldsymbol{x}-\boldsymbol{\xi}|} \,\mathrm{d}\boldsymbol{\xi} \,, \tag{5.19}$$

where Ω is a source domain of finite extent. It useful to consider the far-field behavior of the solution. Provided that $|\boldsymbol{\xi}| \ll |\boldsymbol{x}|$, the above relation might be simplified (see e.g., [18]):

$$p'(\boldsymbol{x},t) \approx \frac{1}{4\pi c_0}\frac{\boldsymbol{x}}{|\boldsymbol{x}|^2} \cdot \frac{\partial}{\partial t} \iiint_{\Omega(\boldsymbol{\xi})} \boldsymbol{f}\left(t - \frac{|\boldsymbol{x}|}{c_0} + \frac{\boldsymbol{x}\cdot\boldsymbol{\xi}}{c_0|\boldsymbol{x}|}\right) \,\mathrm{d}\boldsymbol{\xi} \,. \tag{5.20}$$

Sometimes this manipulation is known as the Fraunhofer approximation.

Now the transition between the Curle's analogy in differential form (Eq. (2.59)) and its integral forms (Eqs. (2.60), (2.61)) can be completed. The last missing piece is converting the volume integral from Eq. (5.19) to the surface ones in Eqs. (2.60), (2.61). The use is made an identity for the Heaviside function as introduced above (see p. 21) [18]:

$$\iiint_V \boldsymbol{\Phi}\boldsymbol{\nabla}\mathrm{H} \,\mathrm{d}V = \oiint_S \boldsymbol{\Phi}\cdot\boldsymbol{n} \,\mathrm{d}S \,, \tag{5.21}$$

where $\boldsymbol{\Phi}$ is an arbitrary function defined in V and on S and $\boldsymbol{n}$ is the (outer) normal vector to the surface S.

Generally, the Green's function for the convective wave equation (e.g. Eq. (2.46)) might be necessary in problems that include non-zero mean flow. For arbitrary Mach numbers the complexity of treatment significantly grows. However, for subsonic case all terms due to mean flow are of $\mathcal{O}\left(\mathrm{Ma}^2\right)$ (see e.g., [47]), so their influence on the specific scenarios presented within this work is negligibly low. Moreover, as pointed out above (Sec. 2.5.1), the Lighthill's analogy virtually transposes the problem to an analogous non-moving medium, so the convected Green's function is not required.

Appendix C – Multipole expansion of aeroacoustical sources

Let $Q(\boldsymbol{x},t)$ denote an arbitrary source term of the wave equation (in the d'Alembertian form):

$$\frac{1}{c_0}\frac{\partial^2 p'}{\partial t^2} - \boldsymbol{\nabla}^2 p' = Q \tag{5.22}$$

In fact, $Q(\boldsymbol{x},t)$ might be (and practically very often is) a spatially varying field. An useful insight into its nature and defining traits is obtained by analyzing it by the so-called multipole expansion. The cornerstone of the method is the spatial Taylor expansion of the Green's function. Note that only the free-field Green's function is used in the course of this work. Let the finite source domain $\Omega(\boldsymbol{\xi})$ be centered around some point $\boldsymbol{\xi}_0$. Then the Taylor expansion of the Green's function reads

$$G = G_0 + (\boldsymbol{\nabla}_{\boldsymbol{\xi}} G)_0 \cdot (\boldsymbol{\xi} - \boldsymbol{\xi}_0) + (\boldsymbol{\nabla}_{\boldsymbol{\xi}} \boldsymbol{\nabla}_{\boldsymbol{\xi}} G)_0 : (\boldsymbol{\xi} - \boldsymbol{\xi}_0)(\boldsymbol{\xi} - \boldsymbol{\xi}_0) + \dots \,, \tag{5.23}$$

where the subscript $()_0$ denote the evaluation at $\boldsymbol{\xi}_0$ and the subscript $\boldsymbol{\nabla}_{\boldsymbol{\xi}}$ is a reminder that the operation is taken with respect to $\boldsymbol{\xi}$.

Inserting the free-field Green's function (5.18) into Eq. (5.23) the following solution to the inhomogenous wave equation Eq. (5.22) might be obtained after some manipulations (see e.g., [47]):

$$p'(\boldsymbol{x},t) = \sum_{i,j,k=0}^{\infty} (-1)^{i+j+k} \frac{\partial^{i+j+k}}{\partial x_1^i \partial x_2^j \partial x_3^k} \left[\frac{m_{ijk}(\tau_0)}{4\pi |\boldsymbol{x} - \boldsymbol{\xi}_0|} \right] , \tag{5.24}$$

with

$$m_{ijk}(\tau_0) = \iiint_{\Omega} \frac{1}{i!j!k!} \left(\xi_1 - \xi_{10}\right)^i \left(\xi_2 - \xi_{20}\right)^j \left(\xi_3 - \xi_{30}\right)^k Q(\boldsymbol{\xi}, \tau_0) \, \mathrm{d}\Omega \,, \tag{5.25}$$

where $\boldsymbol{\xi} = (\xi_1, \xi_2, \xi_3)$ and $\tau_0 = t - |\boldsymbol{x} - \boldsymbol{\xi}_0|/c_0$ is the retarded time. Note that it is defined with respect to the fixed $\boldsymbol{\xi}_0$ and therefore it is independent of $\boldsymbol{\xi}$. The quantity m_{ijk} is called the multipole moment of order 2^{i+j+k}, where $i = j = k = 0$ stands for monopole term, $i + j + k = 1$ for dipole terms, $i + j + k = 2$ for quadrupole terms and so on.

Very useful expression is obtained employing the far-field (Fraunhofer) approximation:

$$p'(\boldsymbol{x},t) \approx \frac{1}{4\pi |\boldsymbol{x} - \boldsymbol{\xi}_0|} \sum_{i,j,k=0}^{\infty} \frac{1}{c_0^{i+j+k}} \cos^i \theta_1 \cos^j \theta_2 \cos^k \theta_3 \frac{\partial^{i+j+k}}{\partial t^{i+j+k}} m_{ijk}(\tau_0) \,, \tag{5.26}$$

where $\cos\theta_{1,2,3}$ are the direction cosines with respect to axes $x_{1,2,3}$ ($\cos\theta_1 = \partial|\boldsymbol{x} - \boldsymbol{\xi}_0|/\partial x_1$). Note that Eq. (5.20) is just a special case of this general form with known multipole order and source kind.

It follows that the capability of the source to efficiently radiate into the far-field significantly decrease and radiation pattern grows in complexity with the multipole order. Such estimation is convenient for assessing the relative importance of source terms.

The multipole orders of the source terms arising from the aeroacoustic analogies (p. 18) are now determined. For brevity, only two cases are discussed in detail. The rest follows from the analogous treatment of respective differential operators. The two most important cases are:

$$Q_L = \boldsymbol{\nabla}\cdot\boldsymbol{\nabla}\cdot(\rho_0\boldsymbol{u}\boldsymbol{u}) \ , \tag{5.27}$$
$$Q_H = \rho_0\boldsymbol{\nabla}\cdot(\boldsymbol{\omega}\times\boldsymbol{u}) \ , \tag{5.28}$$

where Q_L, Q_H denote the source terms according to the Lighthill's and Howe's analogy respectively (for low Mach number flow).

When the source domain Ω is finite, then the monopole terms of both are zero. To show that, the monopole moments are calculated:

$$m_{000}(Q_L) = \iiint_\Omega \boldsymbol{\nabla}\cdot\boldsymbol{\nabla}\cdot(\rho_0\boldsymbol{u}\boldsymbol{u}) \ \mathrm{d}\Omega = \oiint_{\partial\Omega} \boldsymbol{\nabla}\cdot(\rho_0\boldsymbol{u}\boldsymbol{u})\cdot\boldsymbol{n} \ \mathrm{d}S \ , \tag{5.29}$$
$$m_{000}(Q_H) = \iiint_\Omega \rho_0\boldsymbol{\nabla}\cdot(\boldsymbol{\omega}\times\boldsymbol{u}) \ \mathrm{d}\Omega = \oiint_{\partial\Omega} \rho_0\,(\boldsymbol{\omega}\times\boldsymbol{u})\cdot\boldsymbol{n} \ \mathrm{d}S \ . \tag{5.30}$$

But since the source domain is finite (there are no contribution from the external field), both surface integrals yield zero. Therefore both source terms radiate less efficiently than a monopole (say, a rigid radially vibrating sphere).

Before calculating the dipolar moments, consider following manipulations:

$$\xi_1\boldsymbol{\nabla}\cdot\boldsymbol{f} = \boldsymbol{\nabla}\cdot(\xi_1\boldsymbol{f}) - \boldsymbol{f}\cdot\boldsymbol{\nabla}\xi_1 = \boldsymbol{\nabla}\cdot(\xi_1\boldsymbol{f}) - f_1 \ , \tag{5.31}$$
$$\xi_1\boldsymbol{\nabla}\cdot\boldsymbol{\nabla}\cdot(\boldsymbol{u}\boldsymbol{u}) = \boldsymbol{\nabla}\cdot[\xi_1\boldsymbol{\nabla}\cdot(\boldsymbol{u}\boldsymbol{u})] - (\boldsymbol{\nabla}\xi_1)\cdot[\boldsymbol{\nabla}\cdot(\boldsymbol{u}\boldsymbol{u})] = \boldsymbol{\nabla}\cdot[\xi_1\boldsymbol{\nabla}\cdot(\boldsymbol{u}\boldsymbol{u}) - \boldsymbol{e}_1\cdot\boldsymbol{u}\boldsymbol{u}] \ . \tag{5.32}$$

From the same considerations about the source domain finiteness it follows that:

$$m_{100}(Q_H) = \iiint_\Omega \rho_0\xi_1\boldsymbol{\nabla}\cdot(\boldsymbol{\omega}\times\boldsymbol{u}) \ \mathrm{d}\Omega = -\iiint_\Omega \rho_0\,(\boldsymbol{\omega}\times\boldsymbol{u})\cdot\boldsymbol{e}_1 \ \mathrm{d}\Omega \ , \tag{5.33}$$
$$m_{100}(Q_L) = \iiint_\Omega \rho_0\xi_1\boldsymbol{\nabla}\cdot\boldsymbol{\nabla}\cdot(\boldsymbol{u}\boldsymbol{u}) \ \mathrm{d}\Omega = \oiint_{\partial\Omega} [\xi_1\boldsymbol{\nabla}\cdot(\boldsymbol{u}\boldsymbol{u}) - \boldsymbol{e}_1\cdot(\boldsymbol{u}\boldsymbol{u})]\cdot\boldsymbol{n} \ \mathrm{d}S = 0 \tag{5.34}$$

and similarly for m_{010} and m_{001}. So the Howe's source term has the nonzero dipole moment, while the Lighthill's one has the first nontrivial multipole moment at the quadrupolar order. This is one of the decisive points in favor of "vortices are the voice of the flow".

Note that $m_{100}(Q_H)$ yields in fact an averaged value of the force component over the source domain. Therefore, the quadrupole and higher terms in Q_H are necessary to capture the details of the force distribution within the source domain. An analogous argumentation would be in place considering the quadrupolar terms of Q_L. Strictly speaking, the source term Q_H should be labeled "no less than dipolar" and similarly the term Q_L "no less than quadrupolar". Such accuracy is usually omitted for the sake of simplicity, because the decisive trait is the leading order in the multipole expansion. Simply put, when it comes to the far-field radiation "dipole beats the quadrupole".

Appendix D – Basic analysis of the van der Pol equation

A detailed analysis of the homogenous van der Pol equation is not given above for the sake of brevity. Instead, some of its basic properties are summarized here. Namely the linear stability analysis and solution in the weakly non-linear approximation.

The van der Pol equation in terms of an arbitrary variable u might be expressed

$$\frac{\mathrm{d}^2 u}{\mathrm{d}t^2} + \varepsilon\omega\left(u^2 - 1\right)\frac{\mathrm{d}u}{\mathrm{d}t} + \omega^2 u = 0\,, \tag{5.35}$$

where $\varepsilon \geq 0$ is the non-dimensional non-linearity parameter. If the variable t is time (in seconds), then the variable ω is the angular frequency (in radians per second). Eq. (5.35) describes a harmonic oscillator with non-linear damping supplemented by the second term. It may be equivalently expressed as two fisrt-order ordinary differential equations

$$\frac{\mathrm{d}u}{\mathrm{d}t} = v\,, \tag{5.36}$$

$$\frac{\mathrm{d}v}{\mathrm{d}t} = -\varepsilon\omega\left(u^2 - 1\right)v - \omega^2 u\,. \tag{5.37}$$

First, the system (5.36)–(5.37) is investigated by means of linear stability analysis (see e.g., [51, 111]). The only fixed point (sometimes equilibrium point or stationary point, i.e. the point at which the right-hand-sides of (5.36)–(5.37) are zero) is $u = v = 0$. Around this point a linearization $u = 0 + u' + \mathcal{O}\left(u'^2\right)$ and similarly for v is employed. It follows that

$$\frac{\mathrm{d}u'}{\mathrm{d}t} = v'\,, \tag{5.38}$$

$$\frac{\mathrm{d}v'}{\mathrm{d}t} = \varepsilon\omega v' - \omega^2 u'\,. \tag{5.39}$$

Solution is sought in the form $u' = u'_0 e^{\alpha t}$, $v' = v'_0 e^{\alpha t}$. Substituting this to Eqs. (5.38)–(5.39) the condition for α is obtained after some manipulations as the second order polynomial equation:

$$\alpha^2 - \varepsilon\omega\alpha + \omega^2 = 0\,. \tag{5.40}$$

Two possible roots are:

$$\alpha_{1,2} = \frac{\varepsilon\omega \pm \mathrm{i}\omega\sqrt{4 - \varepsilon^2}}{2}\,. \tag{5.41}$$

Therefore, the origin is linearly unstable due to positive real part of $\alpha_{1,2}$. For small ε, the other term is imaginary, which means that the trajectory in the (u', v') phase plane will spiral around the origin. Hence, the origin is called an unstable (repelling) focus (see [51, 111] for more details). It follows that the van der Pol equation (5.35) yields oscillating solution of growing amplitude that starts from infinitesimal fluctuations.

Intuitively, when u is not small any more in Eq. (5.35), the sign of the second term changes and consequently the negative damping turns to be positive. Such behavior leads to existence of the limit cycle around the origin, which may be formally proven by the Liénard or Poincaré-Bendixson theorem (see e.g. [51, 111]).

In the case of weak nonlinearity ($\varepsilon \ll 1$), an approximate analytical solution to Eq. (5.35) might be found by the method of averaging or the method of multiple scales (see e.g., [51]). The latter, which belongs among the wide family of perturbation techniques, is outlined here.

For the sake of simplicity, let $\omega = 1$ and the whole system nondimensional. This could be done without loss of generality by scaling the time variable. The expansion of t and u is introduced in the form:

$$u = u_0 + u_1 + u_2 + ... = u_0 + \varepsilon u_0 + \varepsilon^2 u_0 + ... \,, \tag{5.42}$$

$$t = t_0 + t_1 + t_2 + ... = t_0 + \varepsilon t_0 + \varepsilon^2 t_0 + ... \,. \tag{5.43}$$

Therefore, the time-scale $t_1 = \varepsilon t_0$ measures events that are slow compared to the (fast) main mechanism. Similarly, the quantity $u_1 = \varepsilon u_0$ provides a small first-order correction to the robust u_0. By substitution of the multiple scales expansion into Eq. 5.35 and collecting the terms of the same order one obtains two equations for the lowest orders:

$$\frac{\partial^2 u_0}{\partial t_0^2} + u_0 = 0 \,, \tag{5.44}$$

$$\frac{\partial^2 u_1}{\partial t_0^2} + u_1 = (1 - u_0^2)\frac{\partial u_0}{\partial t_0} - 2\frac{\partial^2 u_0}{\partial t_0 \partial t_1} \,. \tag{5.45}$$

It is straightforward to solve the first equation, but it is vital to keep in mind that the integration constants might depend on the higher terms of the expansion:

$$u_0 = A(t_1, t_2, ...) \cos\left[t + \phi(t_1, t_2, ...)\right] \,. \tag{5.46}$$

In order to find appropriate conditions for A and φ, note that the equation (5.45) governing the first-order corrections, shall not contain terms on the right-hand-side that would be in resonance with the left-hand-side. Such case would give rise to the so-called secular terms infinitely growing in time (see

e.g., [51, 111]). Inserting the solution (5.46) into the left hand side of Eq. (5.45) one finds the conditions for removing the resonances:

$$2A\frac{\partial\phi}{\partial t_1} = 0 \,, \tag{5.47}$$

$$2\frac{\partial A}{\partial t_1} = A\left(1 - \frac{A^2}{4}\right) \,, \tag{5.48}$$

which yields a solution valid to the first order of the expansion in the form:

$$u = \frac{2\cos(t+\phi)}{\sqrt{4c_1 e^{-\varepsilon t}+1}} \,, \quad \phi,\ c_1 = \text{const.} \,. \tag{5.49}$$

For $t \to \infty$ the denominator is 1 and the amplitude of oscillations is equal to 2 independently of the initial conditions. This is the consequence of the stable limit cycle as commented above. Note that the amplitude of 2 is reached for any initial conditions allowing for $c_1 > 0$, which is consistent with the existence of the stable limit cycle.

Profound analysis of the forced van der Pol equation is beyond the scope of this work (see e.g., [131] for more details).

Appendix E – List of symbols and abbreviations

LES	Large Eddy Simulations
LNSE	Linearized Navier-Stokes equations
RANS	Reynolds-averaged Navier-Stokes equations
URANS	Unsteady Reynolds-averaged Navier-Stokes equations

$\mathbb{C}$	set of complex numbers
$\mathbb{N}$	set of natural numbers
$\mathbb{R}$	set of real numbers

Ma	Mach number
Pr	Prandtl number
Re	Reynolds number
Sr	Strouhal number

a	lattice constant
$\boldsymbol{a}$	primitive vector of the direct lattice
$\boldsymbol{b}$	primitive vector of the reciprocal lattice
B	specific total enthalpy, model coefficient
c_0	adiabatic speed of sound
c_p	specific heat capacity at constant pressure
c_V	specific heat capacity at constant volume
e	specific internal energy
$\boldsymbol{F}$	force
f	frequency, force density
$\boldsymbol{f}$	force density field
G	Green's function
H	Heaviside function
i	specific enthalpy
k	wavenumber, turbulent kinetic energy
$\boldsymbol{k}$	wave vector
P	characteristic pressure, equivalent pressure source
p	pressure
q	dimensionless pressure
r	radius
R	reflection coefficient
S	(control) surface
s	specific entropy
T	thermodynamic termeprature, time interval
T	transmission coefficient
t	time
U	characteristic flow velocity
$\boldsymbol{u}$	velocity

γ	ratio of specific heat capacities
δ	Dirac function
δ_μ	thermoviscous penetration depth
ε	small nondimensional parameter, turbulence dissipation rate
ζ	sound diffusivity
κ	thermal conductivity
μ	shear viscosity
ν	kinematic viscosity, dimensionless frequency
ξ	coupling coefficient
$\boldsymbol{\xi}$	auxilliary radius vector
P	characteristic density
ρ	density
τ	dimensionless time, retarded time
$\boldsymbol{\tau}$	shear stress tensor
φ	(scalar) velocity potential
$\boldsymbol{\Psi}$	vector potential
ω	angular frequency, specific turbulence dissipation
$\boldsymbol{\omega}$	vorticity